

## ABSTRACT

Title of Dissertation: TOWARDS OBJECT-BASED EVALUATION  
OF INDIVIDUAL FIRES AT GLOBAL  
SCALES

Michael Laurence Humber, Doctor of  
Philosophy, 2019

Dissertation directed by: Professor Christopher Justice, Department of  
Geographical Sciences

Fire is a complex biophysical variable that has shaped the land surface for over 400 million years and continues to play important roles in landscape management, atmospheric emissions, and ecology. Our understanding of global fire patterns has improved dramatically in recent decades, coincident with the rise of systematic acquisition and development of global thematic products based on satellite remote sensing. Currently, there are several operational algorithms which map burned area, relying on coarse spatial resolution sensors with high temporal frequencies to identify fire-affected surfaces. While wildfires have been analyzed over large areas at the pixel level, object-based methods can provide more detailed attributes about individual fires such as fire size, severity, and spread rate. This dissertation evaluates burned area products using object-based methods to quantify errors in burn shapes and to extract individual fires from existing datasets.

First, a wall-to-wall intercomparison of four publicly available burned area products highlights differences in the spatial and temporal patterns of burning identified by each product. The results of the intercomparison show that the MODIS Collection 6 MCD64A1 Burned Area product mapped the most burned area out of the four products, and all products except the Copernicus Burnt Area product showed agreement with regard to temporal burning patterns. In order to determine the fitness of the MCD64A1 product for mapping fire shapes, a framework for evaluating the shape accuracy of individual fires was developed using existing object-based metrics and a novel metric, the “edge error”. The object-based accuracy assessment demonstrated that MCD64A1 preserves the fire shape well compared to medium resolution data. Based on this result, an algorithm for extracting individual fires from MCD64A1 data was developed which improves upon existing algorithms through its use of an uncertainty-based approach rather than empirically driven approaches. The individual fires extracted by this algorithm were validated against medium resolution data in Canada and Alaska using object-based metrics, and the results indicate the algorithm provides an improvement over similar datasets. Overall, this dissertation demonstrates the capability of coarse resolution burned area products to accurately identify individual fire shapes and sizes. Recommendations for future work include improving the quality assessment of burned area products and continuing research into identifying spatiotemporal patterns in fire size distributions over large areas.

TOWARDS OBJECT-BASED EVALUATION OF INDIVIDUAL FIRES AT  
GLOBAL SCALES

by

Michael Laurence Humber

Dissertation submitted to the Faculty of the Graduate School of the  
University of Maryland, College Park, in partial fulfillment  
of the requirements for the degree of  
Doctor of Philosophy  
2019

Advisory Committee:  
Professor Christopher Justice, Chair  
Professor Tatiana Loboda  
Professor Louis Giglio  
Professor Luigi Boschetti  
Professor Zhanqing Li

© Copyright by  
Michael Laurence Humber  
2019

## Acknowledgments

Throughout my years in the Department of Geographical Sciences, I have had the pleasure of working with a number of excellent professors and researchers. It would be impossible to name all of them, but to each I am grateful. Special thanks are owed to my advisory committee, Professors Justice, Loboda, Giglio, and Boschetti, who provided invaluable guidance and expertise throughout the last five years – there is no more qualified set of individuals in this field. Dr. Justice, in particular, has helped me balance this dissertation with my professional work throughout the years. I also would like to thank Dr. Zhanqing Li, who has graciously served as the Dean’s representative for the committee.

I would be remiss not to acknowledge the opportunities I’ve been fortunate to have, and the people who have funded me throughout the years. Dr. Boschetti first hired me as an undergraduate intern in 2010 and brought me into the world of remote sensing. Dr. Matt Hansen and Andrea Baraldi funded me under the CARPE and SIAM programs, respectively, as a master’s student. Dr. Giglio has kept me on under the MODIS/VIIRS Burned Area projects and has taught me a great deal about fire mapping and image processing. I want to thank everyone involved with the NASA Harvest program, including Dr. Alyssa Whitcraft and Dr. Pierre Guillevic who have included me in their projects, and especially Dr. Inbal Becker-Reshef whose support and flexibility throughout the years allowed me to pursue this degree while working in a different field.

On a more personal note, thank you to my family, friends, and colleagues, many of whom have been around since before the start of this work. Last but certainly not

least, thank you to Maria, whose love, kindness, support, and (at times) empathy helped me throughout this research – going through this process together made everything better.

## Table of Contents

Acknowledgments.....	ii
List of Tables .....	vi
List of Figures.....	vii
Chapter 1 – Introduction .....	1
Background.....	1
Purpose and Research Objectives .....	8
Organization of the study.....	11
Chapter 2 – Spatial and Temporal Intercomparison of Global Burned Area Products .....	14
Introduction.....	14
Data.....	18
Global Burned Area Products .....	19
MODIS MCD14ML Active Fire Product.....	22
Methods.....	23
Comparison Grid.....	23
Spatial Analysis Grid .....	24
Temporal Comparison Grid .....	25
Data Preprocessing.....	25
Data Analysis .....	26
Burned Area Totals.....	26
Scatterplots.....	27
Temporal Heat Maps.....	27
Results.....	28
Overview.....	29
Fire CCI and MCD64A1 Comparison .....	35
Copernicus Burnt Area and MCD64A1 Comparison .....	41
MCD45A1 and MCD64A1 Comparison .....	45
Discussion and Conclusions .....	48
Acknowledgments.....	52
Supplemental material .....	53
Chapter 3 – Assessing the Shape Accuracy of Coarse-resolution Burned Area Classifications .....	54
Introduction.....	54
Data.....	59
MCD64A1 Burned Area Product.....	59
Monitoring Trends in Burn Severity (MTBS) .....	60
Study Area .....	62
Methods.....	63
Extraction and Harmonization .....	64
Metric Calculation .....	65
Results.....	75
Minimum Achievable Edge Error.....	75
Edge Error and Overlapping Area Metrics .....	77
Discussion and Conclusion .....	80

Appendix.....	83
Acknowledgments.....	86
Chapter 4 – A MODIS MCD64A1-based Algorithm for Identifying Individual Fires in Boreal and Arctic North America.....	87
Introduction.....	87
Data and Methods .....	91
Individual Fire Extraction.....	91
Accuracy Metrics .....	95
Accuracy Assessment .....	99
Discussion and Conclusions .....	105
Chapter 5 – Discussion and Conclusions.....	108
Summary of Findings.....	108
Impact and Importance to the Broader Community .....	113
Directions for Future Work.....	118
References.....	122

## List of Tables

Table 3.1. Fires selected for this study, ordered by size (area reported by MTBS). Dominant Land Cover determined by the degree of overlap with the National Land Cover Database 2011 (NLCD).....	62
Table 3.2. Object-based accuracy metrics for eight fires in the study region. The MAEE is presented parenthesis with the EE metric. ....	77
Table 4.1. Edge Error metrics (in meters) for individual fires extracted from MCD64A1 vs. ABoVE reference fires. Fire Atlas - MUSE indicates the difference in median distance from mapped-to-reference boundaries between algorithms.....	100
Table 4.2. Oversegmentation (OS) and Undersegmentation (US) errors for individual fires extracted from MCD64A1 vs. ABoVE reference fires. Fire Atlas - MUSE indicates the difference in the error metric between algorithms.....	101

## List of Figures

Figure 2.1. GFED fire regions with Thiessen Scene Area (TSA) polygons superimposed. ....	24
Figure 2.2. Yearly burned area totals (km <sup>2</sup> ) per fire region and globally. Bar plot size is normalized to the maximum of the fire region across all products and all years....	30
Figure 2.3. Total burned area identified per year by each product. ....	31
Figure 2.4. Percent of burned area detected per fire region, normalized to the maximum amount of burned area identified by any product in the respective fire region (2005 - 2011). ....	31
Figure 2.5. Comparison of the timing of active fire detections with burned area detections (Australia - Europe). ....	33
Figure 2.6. Comparison of the timing of active fire detections with burned area detections (Middle East - Temperate North America).....	34
Figure 2.7. Maximum differenced burned area totals per TSA for 2006 between MCD64A1 and Fire CCI. Each cell indicates the greatest difference between concurrent months in the year, with darker blue indicating higher Fire CCI totals and darker red indicating higher MCD64A1 totals. ....	36
Figure 2.8. Scatterplot for Boreal Asia (BOAS) in May 2006 illustrating burned area detected per TSA polygon for Fire CCI and MCD64A1. The four circled points represent the largest difference in burned area detected between Fire CCI and MCD64A1 and coincide with the burning events described in Chuvieco et al. (2016). ....	37
Figure 2.9. Comparison of Eastern Europe burning episode, May 2006. Top: Best available Landsat imagery, from left to right - Path 152 Row 21 (Landsat 5, May 12, 2006); Path 151 Row 21 (Landsat 7, June 6, 2006); Path 150 Row 21 (Landsat 7, May 30, 2006) with SWIR1-NIR-SWIR2 composite. Middle: Fire CCI burned area for May 2006. Bottom: MCD64A1 burned area for May 2006. ....	38
Figure 2.10. Scatterplots for Northern Hemisphere Africa (NHAF) in January 2006 illustrating burned area detected per TSA polygon for Fire CCI (left) / MCD45A1 (right) and MCD64A1. Note that while the slope is similar, the RMSE is much greater for the CCI plot. ....	39
Figure 2.11. Example of artifacts introduced by the region growing procedure in the Fire CCI product. Western portion of NHAFR, January 2006. ....	40
Figure 2.12. Maximum differenced burned area totals per TSA for 2006, MCD64A1 and Copernicus Burnt Area. Each cell indicates the greatest difference between	

concurrent months in the year, with darker blue indicating higher Copernicus Burnt Area totals and darker red indicating higher MCD64A1 totals. ....	41
Figure 2.13. Burned area identifications for Copernicus (top) and MCD64A1 (bottom) in September 2006 for BOAS and CEAS, aggregated to 6 km grid cell (maximum value aggregation). ....	43
Figure 2.14. Scatterplot of burned area per TSA in AUST, June (left) and November (right) 2006. Copernicus (y-axis) detects less burning per TSA but, in June, more TSA's with burning. ....	44
Figure 2.15. Burned area identifications for Copernicus (top) and MCD64A1 (bottom) in June (left) and November (right) 2006 for AUST, aggregation to 6 km grid cell (maximum value). ....	44
Figure 2.16. Maximum differenced burned area totals per TSA for 2006, MCD64A1 and MCD45A1. Each cell indicates the greatest difference between concurrent months in the year, with darker blue indicating higher MCD45A1 totals and darker red indicating higher MCD64A1 totals. ....	45
Figure 2.17. Example scatterplots of global TSA Burned Area totals for MCD64A1 vs. MCD45A1 (left) and Fire CCI (right). While the TLS regression slopes are similar, the RMSE of the global distribution is greater for Fire CCI. ....	46
Figure 2.18. AUST Jan 2006. (Left) Scatterplot of MCD45A1 Burned Area per TSA vs MCD14ML Active Fire count per TSA; note the burned area totals associated with no active fire detections. (Right) Map of MCD45A1 burn identifications and MCD14ML active fire detections. ....	47
Figure 2.19. October 2006 EQAS fires in southern Kalimantan, Indonesia. MCD45A1 (top) and MCD64A1 (bottom) detections overlaid on Landsat 5 scenes path/row 118/062 (Oct 29, 2006; right) and 119/062 (Nov 5, 2006; left) with SWIR1-NIR-SWIR2 composite. ....	48
Figure 3.1. Eight fires selected for this study, depicted in RGB = SWIR2, NIR, Red composite with MTBS boundaries (yellow). ....	63
Figure 3.2. Association of four evaluated edge locations, Burn(evali), to two target edge locations, Burn(tgtj). Note that evaluated edge locations 1 and 4 are associated with the nearest target burn edge location while evaluated edge location 3 is associated with the geometric normal of the line segment Burn(tgt1), Burn(tgt2) and in the case of evaluated edge location 2, the geometric normal and nearest neighbor distance are identical. ....	67
Figure 3.3. Edge error vectors for two hypothetical burns, in the direction of coarse to high-resolution. The “Target Burned Cells” represent the reference dataset at higher resolution, in this instance MTBS. The “Evaluated Burn Cells” represent the coarser	

resolution dataset, i.e. MCD64A1. The EEi vectors (arrows) show the direction and magnitude of the cell-specific edge error.....	69
Figure 3.4. Examples of cross-resolution edge location scenarios. (a) illustrates burn boundaries at both resolutions are ideally co-located, while (b) illustrated a scenario in which contains commission and omission errors. The distance between edge locations in both cases is the result of only resolution differences.....	72
Figure 3.5. Esmerelda Fire: Original MTBS classification and projection/resampling to MODIS Sinusoidal 500-m grid indicating the percent of each cell identified as burned by MTBS.....	74
Figure 3.6. Esmerelda Fire: Edge cell locations for MTBS data at MODIS 500-m resolution using 1%, 50%, and 100% thresholds.....	74
Figure 3.7. Minimum achievable edge error thresholds for MODIS resolution edge locations (463.3127 m cells) and MTBS native resolution edge locations. Red triangles indicate series minima; gray dashed lines indicate MODIS cell size. ....	76
Figure 3.8. Mean edge error for MCD64A1 to MTBS. The dashed gray line indicates MODIS cell size.....	78
Figure 3.9. Rim Fire edge locations identified by MCD64A1 and MTBS. Significant discrepancies in the northernmost part of the image contribute to high EE values....	79
Figure 3.10. MCD64A1 and Modified MTBS edge locations including interior unburned islands. Top: Esmerelda Fire (Nevada, 2005) has an EE of 252.59. Bottom: East Amarillo Complex (Texas, 2006) has an EE of 398.52.....	86
Figure 4.1. Biomes within the Alaska and Canada study area.....	91
Figure 4.2. MODIS MCD64A1 burned area detections in Canada and Alaska. Year refers to fire year, from March to the following February.....	93
Figure 4.3. Graph of Edge Error through time for individual fires extracted from MCD64A1 vs. ABoVE reference fires. The gray dashed line indicates 1x MODIS cell dimension, the black dashed line indicates 2x MODIS cell dimension.....	101
Figure 4.4. Graph of Oversegmentation (OS) and Undersegmentation (US) errors through time for individual fires extracted from MCD64A1 vs. ABoVE reference fires. ....	102
Figure 4.5. The 2007 Anuktavuk Fire. (a) Landsat-7 Path 073 Rows 011-012 composite (June 2008; R=Mid IR, G=NIR, B=Red). (b) MUSE overlapping fire segments. (c) Fire Atlas overlapping fire segments. In (b) and (c), each color corresponds to an individual extracted fire segment. Note that MCD64A1 underestimates the area of the burn, which propagates into the extraction algorithms. ....	105

Figure 4.6. The 95th percentile fire size for 1-degree cells, based on the 2002 through 2018 fire years according to the MUSE algorithm. .... 106

Figure 4.7. Size of individual fires throughout any of the 2002 to 2018 fire seasons according to the MUSE algorithm. .... 106

# Chapter 1 – Introduction

## Background

Fire is an important land surface process affecting systems at multiple scales. At present, wildfires burn an estimated two to four percent of the Earth's land surface every year (Randerson *et al.*, 2012; Giglio *et al.*, 2018; Humber *et al.*, 2019). Charcoal records show that fire has played a role in shaping the Earth for hundreds of millions of years (Scott and Glasspool, 2006; Pausas and Keeley, 2009). Though sometimes viewed through the lens of fire as a landscape disturbance (Turner *et al.*, 1998), wildfires can be an important part of an ecosystem in equilibrium (Van Langevelde *et al.*, 2003) and can act as a control on the extent of vegetation types globally (Bond and Keeley, 2005; Bond, Woodward and Midgley, 2005).

In wildland areas, such as boreal forests, lightning can result in large wildfires. In more inhabited parts of the world, humans play a significant role in initiating fires and shaping global fire patterns, often with different goals depending on the region in question. For thousands of years, humans have used fire as a tool for clearing land, managing pests, and pasture management (Bowman *et al.*, 2011). On the other hand, human activity in recent decades has led to an overall decrease in the number of fires in and around populated areas due to targeted suppression (for example, to protect property) or through indirect suppression through actions such as constructing roads or cutting fuel breaks which slow the propagation of fire across the surface (Mouillot and Field, 2005; Marlon *et al.*, 2008; Andela *et al.*, 2017).

The influences of climate and human variables have not been constant through time, owing to shifts in the human population size and location. The Industrial Revolution, at the turn of the 19th century, is a logical breakpoint during which rapid changes in technological capacity which allowed the human population to increase dramatically. It was found that while fire activity over the last millennium can be modeled effectively using vegetation and climatological variables, human variables were necessary to replicate known fire patterns (Pechony and Shindell, 2010). The result, according to the same authors, will be an “unprecedentedly fire-prone environment” in the 21st Century.

While human actions such as sparking ignitions, creating fuel breaks through land fragmentation, active fire suppression, and land cover conversion can negate some effects of climate on wildfire activity (Syphard *et al.*, 2017), anthropogenic climate change is nonetheless expected to affect the frequency, extent, and severity of wildfires (Westerling *et al.*, 2006; Flannigan *et al.*, 2009; Abatzoglou and Kolden, 2011). Furthermore, gasses and particulates released by fire play important roles in climate change by altering planetary albedo and increasing the presence of greenhouse gases, and potentially creating a feedback loop depending on the location (Hansen and Nazarenko, 2004; Pyne, 2007; Pechony and Shindell, 2010; Chen *et al.*, 2018).

The complexity of these interactions underscores the importance of understanding fire as a dynamic variable through time. This has been recognized in the context of climate change by several governing bodies, including at the international level, e.g. the Intergovernmental Panel on Climate Change (IPCC,

2012). For a long time, there had been recognition that we need better data on the frequency, extent, and characteristics of fire, so as to be able to track changing fire regimes (Justice and Dowty, 1994) and fire is included among the Essential Climate Variables (GCOS, 2019) defined by the World Meteorological Organization (WMO) Global Observing System for Climate (GCOS). In response to those needs, the international science community has come together to create and coordinate fire products from satellite data with global coverage, initially through the International Geosphere Biosphere Programme Data and Information System (IGBP-DIS; Townshend, 1991) and more recently through the Global Observations of Forest and Land Cover Dynamics (GOFD/GOLD) Fire network (Justice *et al.*, 2003) and the GEO Global Wildfire Information System (GEO, 2019). At the national level, programs such as the Monitoring Trends in Burn Severity project in the United States (Eidenshink *et al.*, 2007) and the Canadian Wildland Fire Information System<sup>1</sup> provide records of individual fires with attributes such as the start date, end date, area burned, and burn severity.

Records of fire activity can inform descriptions of a region's fire regime, which often includes information about the size and spread of fires, fire intensity, burn severity, fire frequency, and seasonality (Bond and Keeley, 2005). There is no standardized definition of fire regime, though several classification schemes have been proposed. Characteristics of individual fires can affect the survival of existing species, even those which have developed fire-tolerant adaptations (Fuller, 1991; Whelan, 1995). For example, Fuller (1991) details that the snowbrush ceanothus,

---

<sup>1</sup> <https://cwfis.cfs.nrcan.gc.ca/home>

which is a fire-dependent species found in chaparral ecosystems, requires a fire temperature of 113 degrees Fahrenheit for seeds to germinate, but, above 300 degrees Fahrenheit the seeds will not survive – fire intensity is, therefore, a key variable in determining the rate at which the snowbrush ceanothus can recolonize the burned area. Considering fire size, Whelan (1995) and Turner *et al.* (1998) note that post-fire vegetation succession comes from two sources – the seed banks remaining from species which were present during the fire, or re-sprouting and colonization from the nearby unburned species. The distance of a given location within the burn to the edge of the burn determines the advantage the nearby colonizing species would have, thus fires with a high perimeter-to-area ratio could favor colonizing species and vice versa.

Proximity to fire, at a broader scale, also plays an important role. Fires near inhabited areas put lives and property at risk (Bowman *et al.*, 2011), and smoke released by fires is a public health hazard (for a thorough review, see Reid *et al.*, 2016). The ramifications of fires can be far-reaching as well. For example, fires occurring in boreal forests and tundra can loft back carbon and soot into the atmosphere, which can transport it to higher latitudes where it settles on permafrost, thusly accelerating melting and further release of greenhouse gases such as methane (Hall *et al.*, 2017).

Knowing that anthropogenic climate forcing affects fire-related climate variables (Abatzoglou and Williams, 2016), establishing baseline datasets of fire characteristics is important to understanding how fire patterns are changing at all spatial scales. Paleo-fire records have been established in some specific locales for periods spanning centuries to millennia using sampling methodologies such as

analysis of charcoal records and lake sediment sampling (e.g. Scott and Glasspool, 2006; Sugihara *et al.*, 2006; Gavin *et al.*, 2007). These records are not generated through standardized analysis techniques and are spatially sparse due to the considerable effort required to construct timelines of fire for each location (Patterson, Edwards and Maguire, 1987; Higuera *et al.*, 2011).

In recent decades, remote sensing through satellite observations has been a valuable source of data for studying land processes in general and has been used as a data source for generating fire records. Although the limited length of the satellite data archive is a hindrance to establishing long-term fire records, remote sensing provides opportunities to systematically observe fires globally. Global fire products generated from satellite observations fall into one of two categories: *burned area products* – representing the post-fire affected area as determined by the removal of vegetation, exposure of soil and presence of charcoal and ash (Roy, 1999; Roy, Boschetti and Smith, 2013) – or *active fire products* – representing location and in some cases the radiative power of fires burning on the Earth surface at the time of the sensor overpass (Justice, Giglio, *et al.*, 2002; Justice *et al.*, 2002; Roy *et al.*, 2008).

Burned area algorithms evaluate burning as an image classification problem, typically identifying burning as the result of a rapid change from a vegetated land cover to one of bare soil, ash, and soot (Roy, 1999; Roy, Boschetti and Smith, 2013). Some of the resulting products have proven to be useful data sources for emissions calculations and for studies at regional to continental scales (e.g. van der Werf *et al.*, 2006; van der Werf *et al.*, 2017).

As a practical matter, wildfires interact with the landscape in a non-uniform manner which makes pixel-based classifications (of burned/unburned cells) inadequate for many situations. Products such as the MTBS fire perimeters (Eidenshink *et al.*, 2007) and the Arctic-Boreal Vulnerability Experiment's Wildfire Date of Burning dataset (Loboda and Hall, 2017) map the extent of burned area objects using individual fires as the basic unit rather than pixels. In the case of MTBS, the data helps land managers make better-informed decisions, while the ABoVE dataset is used to limit the spatial extent of fire progression analysis. Ultimately, the final burn scar shape and size are a reflection of the underlying conditions of the fire such as fuel type and uniformity, topography, and wind (Whelan, 1995). For example, fires occurring on dry surfaces with low biomass, as in savannas, will spread faster and oftentimes be larger. Similarly, fires on a slope will propagate upwards at a faster rate due to the fire ladder effect and likewise move slower downslope as the pre-drying effects of the fire front are lessened.

To date, fire attributes have been difficult to quantify for individual fires at the global scale. The recently published Fire Atlas (Andela *et al.*, 2018) and FRY Database (Laurent *et al.*, 2018) provide data including fire sizes, shape summaries, spread rates, and timing by extracting individual fire boundaries from existing global, coarse spatial resolution burned area products. These are typically derived based on empirical relationships defining the rate at which fires propagate across the landscape and can be global or regionally adapted.

Because fire attributes are derived from existing burned area products, the errors in the latter are propagated to the former. The accuracy of global burned area

products varies greatly from product to product (Roy and Boschetti, 2009; Chuvieco *et al.*, 2018; Humber *et al.*, 2019), making the choice of burned area product non-trivial both generally and for the purposes of fire information extraction. Beyond the choice of burned area product, there is a need to evaluate the accuracy of products mapping individual fires at the object level. Establishing the accuracy of burned area products has taken many forms such as error matrix calculation based on independent reference data (Roy and Boschetti, 2009; Padilla *et al.*, 2014; Padilla *et al.*, 2015), comparison with other burned area products (Giglio *et al.*, 2010), and comparison with active fire products (Roy *et al.*, 2008; Boschetti *et al.*, 2010). While methods such as these assess the accuracy of burned/unburned labels, the accuracy of individual pixels is not the only relevant aspect of burning for end users. In fact, traditional pixel-based accuracy measures, such as overall accuracy, can appear misleading for burned area validation exercises due to the low prevalence of burning on the Earth's surface (Fielding and Bell, 1997).

An alternative to pixel-based approaches is object-based accuracy assessment. While object-based accuracy assessments have been applied to remote sensing-derived maps before (e.g. Clinton, 2010; Persello and Bruzzone, 2010; Baraldi *et al.*, 2013; Baraldi *et al.*, 2014), there has been relatively little work on their application to burned area detection. Even though assumptions drawn from fire shape already influence the selection of parameters in current vegetation models (Chuvieco *et al.*, 2016), assessments of the accuracy of burn scar shapes are rare and the existing work has focused on metrics derived from comparing the extent of overlapping areas rather

than directly comparing burn scar shapes (Remmel and Perera, 2002; Nogueira *et al.*, 2017).

This dissertation furthers research into determining fire attributes from satellite-derived products by systematically analyzing individual wildfires over large areas. This requires investigation of the quality of the available burned area products, development of a framework for assessing the accuracy of individual burned areas through quantification of the shape error, and creation of a new individual fire extraction algorithm to identify trends in fire size and location.

### *Purpose and Research Objectives*

The overarching goal of this work is to develop an object-based understanding of large-area fire patterns which emphasizes the nuance in fire characteristics based on satellite observations, with attention given to how well coarse-resolution burned area maps preserve the spatial integrity of burn scars compared to higher resolution representations. These goals aim to answer the question: can coarse resolution burned area products be used to map individual fires and their specific characteristics such as size and shape, and how accurately do coarse resolution burned area products represent those characteristics?

To address these issues, this dissertation consists of three main components: understanding differences in the currently available burned area products; developing a method for evaluating burned area products using an object-based approach; and implementing object-based analysis methods to answer questions about patterns of burning based on analyzing individual fires. Further details of the three objectives of the study are presented below:

*Objective 1: Characterize the spatial and temporal discrepancies between a suite of the available global burned area products.*

While a proper sampling design can be developed to support a spatially and temporally consistent pixel-based validation, the fact remains that only a small portion of the Earth's surface burning can be represented in a photointerpreted reference dataset due to practical limitations including the number of samples required, cloud cover, and dependence on manual labor. As an alternative approach, intercomparison is a technique in which multiple products are compared wall-to-wall to determine the relative performance of the products, in the absence of a reference dataset (Herold *et al.*, 2008; Pflugmacher *et al.*, 2011). Direct comparison of datasets provides insights into the differences and similarities necessary for determining the usefulness of any given product in a specific region.

*Objective 2: Develop a framework for evaluating the limitations of satellite-derived burned area products regarding burn shape and size, accounting for differences in spatial resolution.*

The limitations of computing capacity and availability of medium spatial resolution (c. 10 – 30 m) satellite data coverage have, until recently, restricted the creation of global products to coarse spatial resolution data (c. 250 m – 1 km). Traditional pixel-based validation measures such as overall accuracy, omission and

commission errors, and relative bias provide estimates of the probability of encountering a classification error for a given cell. While useful for assessing accuracy over large areas, these metrics are less informative at the individual fire scale and therefore are less desirable in an object-oriented framework. Object-oriented metrics in the literature have generally focused on comparing overlapping areas of mapped and reference data, much like pixel-based methods, but do so at the object level (i.e. individual fires) rather than for individual cells or pixels (Bruzzone and Persello, 2010; Clinton *et al.*, 2010; Baraldi, Humber and Boschetti, 2013; Yan and Roy, 2014). This approach is advantageous because the accuracy of a specific fire is generally of more interest to a user than the accuracy of only one cell. But, the widely used object-based accuracy metrics – oversegmentation and undersegmentation – do not account for errors in the boundaries of mapped burn scars. It is, therefore, important to develop a metric for quantifying the error not only in the classification itself but in the shape and size of specific fires in order to provide a more descriptive set of per-fire accuracy metrics.

*Objective 3: Develop a method for extracting individual burn scars from existing burned area maps in order to analyze changes in the size distribution of burning through space and time.*

By examining individual fires over a large area, it is possible to analyze attributes of the fire regime which go beyond total area burned, such as the fire size distribution. Existing datasets that record individual fires are extracted from burned

area products and rely on flood-fill algorithms implementing thresholds representing the fire spread rate (Archibald and Roy, 2009; Andela *et al.*, 2018; Laurent *et al.*, 2018; Oom *et al.*, 2016). These data can be used to map spatial and temporal and patterns of fire sizes but suffer from two limitations. First, the existing products are validated using pixel- or area-based metrics rather than object-based accuracy metrics such as those described in “Objective 2”. Additionally, these products use empirically derived thresholds to determine the fire spread rate rather than data-driven or physically-based approaches.

As higher spatial and temporal resolution sensors become more commonly used for burned area detection, object-based approaches will be required to assess the value of the new generation of burned area maps as tools not only for emissions calculations but also for improving conservation and landscape management. The metrics and methods proposed in these three objectives will be valuable in assessing and interpreting future generations of high resolution fire data.

### Organization of the Study

The research in this dissertation is presented in four chapters. Chapter 2: “Spatial and Temporal Intercomparison of Global Burned Area Products” provides an inventory and assessment of the relative performance of four global burned area products for a study period spanning 2005 – 2011. In this work, a rigorous framework for evaluating the spatial and temporal properties of the burned area products was implemented to characterize the amount and timing of burning detected by each product. The results of this study highlighted the lack of consensus among burned area products, especially at regional scales. Of the evaluated products, the MODIS

Collection 6 MCD64A1 product was selected for analysis in the subsequent work because it is more temporally consistent with active fire detections and creates fewer processing artifacts than the other products examined.

In Chapter 3: “Assessing the shape accuracy of coarse-resolution burned area identifications,” an object-based metric (“Edge Error”) was proposed for quantifying errors in the location of burn scar boundaries identified in coarse spatial resolution burned area maps compared to high spatial resolution reference data. Additionally, a measure of the low-resolution bias (Boschetti *et al.*, 2004) is accounted for via calculation of the minimum achievable edge error. The metric was applied to a sample of eight case study fires in the western United States and automatically to 165 fires from the 2016 burning season identified in the Monitoring Trends in Burn Severity dataset (Eidenshink *et al.*, 2007).

Chapter 4: “A MODIS MCD64A1-based Algorithm for Identifying Individual Fires in Boreal and Arctic North America” introduces a non-empirical MODIS Uncertainty-based Single-fire Extraction algorithm (MUSE), developed for extracting individual fires from the MCD64A1 product in order to evaluate the fire size distribution in Canada and Alaska from 2002 – 2018 at yearly intervals. The fires extracted using the MUSE algorithm were compared to an existing fire events database, the Fire Atlas (Andela *et al.*, 2018), using three object-oriented accuracy metrics, including the edge error.

Lastly, Chapter 5: “Discussion and Conclusions,” summarizes the findings of the previous chapters and provides context for the findings within the body of work of the broader wildfire remote sensing community. Additionally, Chapter 5 highlights

ongoing work and future research based on the work presented in Chapters 2 through 4.

## Chapter 2 – Spatial and Temporal Intercomparison of Global

### Burned Area Products

This work was originally published in Michael L. Humber, Luigi Boschetti, Louis Giglio & Christopher O. Justice (2019) Spatial and temporal intercomparison of four global burned area products, *International Journal of Digital Earth*, 12:4, 460-484, DOI: 10.1080/17538947.2018.1433727. It is reproduced here with minor formatting modifications.

#### Introduction

The availability of well-calibrated, global remote sensing data since the late 1990s has enabled the production of a variety of global, multiannual burned area products that are now freely available. These products, which are generally derived from sensors offering what is, by current standards, coarse spatial resolution (250 m - 1 km), daily or near-daily temporal resolution, include the SPOT-Vegetation and PROBA-V Copernicus Burnt Area products (Tansey *et al.*, 2008), the MODIS burned area products MCD45A1 (Roy *et al.*, 2005) and MCD64A1 (Giglio *et al.*, 2009), the MERIS Fire CCI products (Alonso-Canas and Chuvieco, 2015), the L3JRC (Tansey *et al.*, 2008), GLOBCARBON (Plummer *et al.*, 2006) product, and others (e.g. (Mouillot *et al.*, 2014).

Since the release of the first global burned area data sets, significant discrepancies in areal estimates and spatial patterns have been observed (Boschetti *et al.*, 2004). Despite the continued development and recent proliferation of such products, significant differences persist between them. While the global burned area totals for each product show comparatively good agreement, significant discrepancies with respect to the location and timing of fire activity are apparent at smaller spatial and/or temporal scales. For example, (Alonso-Canas and Chuvieco, 2015) found that

the GFED4, MCD45A1, and Fire CCI products identified total global burned area within 10% of one another for the years 2006 through 2008, though the analysis did not take finer spatial or temporal scales into consideration. (Giglio *et al.*, 2010) showed that although five contemporaneous burned area data sets (GFED2, GFED3, MCD45A1, L3JRC, and GLOBCARBON) reported similar global annual burned area totals, the monthly area burned within fourteen sub-continental regions exhibited substantial differences in magnitude and temporal patterns (Giglio *et al.*, 2010). These findings suggest that burned area products still have significantly different performance in space and time, and support the case for a systematic investigation of such differences.

The standard procedure for the validation of burned area products consists of the comparison with independent, co-located reference data generated from two or more consecutive Landsat class (10-30 m spatial resolution) images. The independent reference data should have minimal error, and should be generated either by visual interpretation (Roy, Frost, *et al.*, 2005; Giglio *et al.*, 2009; Roy and Boschetti, 2009) or by application of a semiautomatic algorithm followed by visual checking and manual refinement (Boschetti *et al.*, 2006; Padilla, Stehman and Chuvieco, 2014; Padilla *et al.*, 2015). Such efforts are expensive, time-consuming, and constrained by the availability of cloud-free images; for this reason, validation studies have relied on a very limited quantity of reference data, typically up to one hundred Landsat image pairs for the global validation of a yearly product. A study of six burned area products for the year 2008, using 30 m reference data generated from 102 Landsat image pairs, found that commission errors of all products were greater than or equal to 42% and

omission errors were greater than or equal to 68% (Padilla, Stehman and Chuvieco, 2014). Similar results were found for the MCD45A1, L3JRC, and GLOBCARBON products in southern Africa using 11 Landsat image pairs (Roy and Boschetti, 2009).

Such validation exercises can provide insight on the performance of burned area mapping algorithms over a range of different conditions, but these exercises rely on probability sampling methods to select a spatially and temporally random set of images in order to preserve the statistical validity of the accuracy estimators (Stehman and Czaplewski, 1998; Boschetti, Stehman and Roy, 2016). The limited set of reference data, which is typically very small relative to the population being estimated, is unlikely to capture all differences between products. In the absence of an extensive global, multi-temporal validation dataset involving a much larger number of reference data scenes, the intercomparison of products is a necessary step in order to characterize the relative performance of each product. Satellite product intercomparison is less costly than validation in terms of time and resources (Garrigues *et al.*, 2008; D'Odorico *et al.*, 2014) and provides systematic information about spatial and temporal patterns of agreement and disagreement. Such information can also provide insights as to the reasons for the differences between products (Boschetti *et al.*, 2004; Chang and Song, 2009) and has been applied to burned area product intercomparisons in the past, e.g. (Sánchez, Heil and Chuvieco, 2014). As with map validation exercises, product intercomparison should be repeated as new sensors and algorithms become available in order to provide an up-to-date record of the relative performance of the data sets to end-users.

In this work, we propose a rigorous framework for the spatial and temporal comparison of global fire products, and we apply this framework to four available operational products: Copernicus Burnt Area, Fire CCI, MODIS MCD45A1, and MODIS MCD64A1. The intercomparison explicitly considers both the temporal and the spatial dimension of the products, by using a spatial and temporal analysis grid. The non-overlapping grid of Thiessen Scene Areas (Gallego, 2005; Kennedy, Yang and Cohen, 2010), generated from the Landsat World Reference System (WRS-2) scene centroids, is partitioned into monthly time intervals, to provide tri-dimensional analysis elements called voxels (a portmanteau word of ‘volume’ and ‘pixels’). The amount of burning within each voxel provides an indicator of the total area burned while comparison with MODIS active fire observations provides an independent indicator of the correctness of the timing of burned patches. The entire 2005-2011 time period during which all the products are available is considered.

Through this analysis, we aim to provide users of global burned area data useful information about the relative performance of the available products by identifying regions where the timing and magnitude of burning detected by the products vary. Additionally, the results of this intercomparison may be useful to algorithm developers for refining and improving the existing products by examining areas where a given product indicates different burning patterns. Finally, the types of discrepancies highlighted by this research can inform stratification strategies used in future validation efforts to ensure that the appropriate surface phenomena are captured by the reference data sets.

## Data

The majority of satellite-derived global fire data sets fall into two broad categories: *burned area products* and *active fire products* (Justice *et al.*, 2002a). Among other applications, these products are used for fire management activities (e.g. Eidenshink *et al.*, 2007; Davies *et al.*, 2009), national monitoring systems (e.g. Boschetti *et al.*, 2008; Leblon, Bourgeau-Chavez and San-Miguel-Ayanz, 2012), calculating fire emissions inventories (e.g. Barbosa, Stroppiana and Cardoso, 1999; Zhang *et al.*, 2003; van der Werf *et al.*, 2010; Giglio, Randerson and van der Werf, 2013; Rossi *et al.*, 2016), fire ecology and fire regime assessment (e.g. Archibald *et al.*, 2010, 2013) and ecosystem modeling exercises (e.g. Yue *et al.*, 2014, 2015). Further discussion of the applications of burned area products can be found in (Mouillot *et al.*, 2014).

Burned area products identify areas that have been affected by fire, detecting the change from a vegetated surface to a surface of char, ash, and bare soil (Roy, 1999). Burned area mapping is essentially a non-permanent land cover change detection problem, and a variety of algorithms have been applied, leading to different results spatially and temporally. Burned area detection changes dramatically with scale due to the presence of mixed pixels (Boschetti, Flasse and Brivio, 2004). As a result, methods applied at coarse spatial resolution will not necessarily perform effectively at finer spatial resolutions (Hall *et al.*, 2016). Due to the variety of approaches implemented in burned area algorithms, there is a large amount of spatial variability amongst burned area products (Figures 2.1, 2.2; Table 2.1).

Active fire products provide the location of all fires actively burning at the satellite overpass time. The short persistence of the signal of active fires means that active fire products are very sensitive to the daily dynamics of biomass burning and that in situations where the fire front moves quickly, there will be an under-sampling of fire dynamics. Based on the physical characteristics of the sensor, the characteristics of the fire and the algorithm used for the detection, active fires orders of magnitude smaller than the pixel size can be detected: as an example, for the MODIS active fire product, fires in temperate deciduous forest covering around 100 m<sup>2</sup> within the 1 km<sup>2</sup> pixel have a 90% probability of detection (Giglio *et al.*, 2003). Active fire data sets offer a direct indication of fire activity which are generated with low levels of commission error (Schroeder *et al.*, 2008); for this reason, data sets such as the MODIS active fire product have been used to assess the temporal accuracy of burned area products (Boschetti *et al.*, 2010; Giglio *et al.*, 2010). In this study, the MODIS Global Monthly Fire Location Product, MCD14ML<sup>2</sup>, is used to provide an independent indication of the presence or absence of fire at given times of year and spatial locations.

#### Global Burned Area Products

Brief descriptions of the products selected for analysis are provided in the subsequent sections, with a tabular summary in Table 2.1.

#### *Copernicus Burnt Area Product*

---

<sup>2</sup> <http://modis-fire.umd.edu/af.html>

The Copernicus Burnt Area products are generated under the European Commission's Copernicus Global Land Service. The Burnt Area products are generated from two sensors and are available as three distinct products. Burned area products generated from the SPOT-Vegetation and Proba-V sensors are available from the Copernicus Global Land Service at 1 km resolution beginning with April 1999A recently released 300 m product derived from Proba-V imagery, is available for the April 2014 to present. The Copernicus Burnt Area products identify burns by detecting sudden changes in a vegetation index. Individual 1 km pixels are grouped into 1° cells and flagged as burned if the value of the vegetation index is more than two standard deviations below the mean value throughout the historical time series for the grid cell (Tansey *et al.*, 2008). The product is distributed in 10° by 10° tiles through the Copernicus Global Land Service data access portal<sup>3</sup>.

#### *Fire CCI Burned Area Product*

Based on acquisitions from the Medium Resolution Imaging Spectrometer (MERIS), on-board the ESA Envisat platform, the Fire CCI product is produced as a 300 m pixel product and a 0.5° gridded product. Both are distributed in the geographic projection, with the pixel product available in six geographic windows<sup>4</sup>. At the time of writing, only the years 2005 to 2011 are publicly available. However, the goals of the Fire CCI project are to extend the archive from 2000 to 2017, with a spatial resolution of 250 m to 500 m for the pixel product and 0.25° for the gridded product. A two-phase algorithm, described in full in (Alonso-Canas and Chuvieco, 2015), is

---

<sup>3</sup> <http://land.copernicus.eu/global>

<sup>4</sup> [https://geogra.uah.es/fire\\_cci/](https://geogra.uah.es/fire_cci/)

used to identify burned areas. First, MODIS active fire locations are used to identify seed pixels corresponding to high confidence burned areas. A region growing algorithm is then applied using the seed pixels selected in the first phase. These phases are applied to MERIS VEGETATION input data, which are distributed in 10° by 10° tiles.

#### *MODIS MCD45A1 Burned Area Product*

The MODIS Collection 5.1 Monthly Burned Area product, MCD45A1, is part of the suite of land monitoring products systematically generated from MODIS data (Justice, Giglio, *et al.*, 2002; Justice, Townshend, *et al.*, 2002). The product uses 500 m input data from the MODIS sensors onboard both the Aqua and Terra satellite platforms and is available starting from April 2000, with the exception of June 2001 which was not processed due to a sensor outage (Roy, Jin, *et al.*, 2005). The algorithm uses a bidirectional reflectance distribution function (BRDF) model to identify burned areas. Following an inversion period of up to 16 days, the observed reflectance of MODIS band 2 (841–876 nm) and band 5 (1230–1250 nm) are compared to a predicted reflectance value based on the BRDF model inversion. A Z-score for both bands is computed as a function of the predicted and observed reflectance values, which is used to identify potential burned areas (Roy, Frost, *et al.*, 2005; Roy, Jin, *et al.*, 2005). The product is distributed by the USGS Land Process Distributed Active Archive Center (LP DAAC)<sup>5</sup>.

#### *MODIS MCD64A1 Burned Area Product*

---

<sup>5</sup> [https://lpdaac.usgs.gov/dataset\\_discovery/modis/modis\\_products\\_table/mcd45a1](https://lpdaac.usgs.gov/dataset_discovery/modis/modis_products_table/mcd45a1)

The MCD64A1 burned area mapping algorithm combines daily MODIS surface reflectance imagery with 1 km MODIS active fire data to map burning on a daily basis at 500 m spatial resolution. The algorithm applies dynamic thresholds to composite MODIS Terra and Aqua imagery generated from a burn-sensitive spectral band index derived from MODIS 1240 nm and 2130 nm Terra and Aqua bands, and a measure of temporal variability. Cumulative MODIS 1 km active fire detections are used to guide the selection of burned and unburned training samples and to guide the specification of prior burned and unburned probabilities (Giglio *et al.*, 2009). The MCD64A1 product is also distributed by the USGS LP DAAC<sup>6</sup>.

For this study, we used the Collection 5.1 MCD45A1 and Collection 6 MCD64A1 burned area products. The Collection 6 MCD64A1 product detects significantly more burned area than the previous Collection 5.1 MCD45A1 and Collection 5.1 MCD64A1 products, with global area burned increasing by approximately 18.5% to 24.5% for the former, and by approximately 25% to 28.5% for the latter. While the Collection 6 product has superseded the Collection 5.1 product, both are included to examine the spatial and temporal manifestations of the difference in algorithm performance which may have significant impacts on existing user applications.

#### MODIS MCD14ML Active Fire Product

We used the MODIS Collection 5 MCD14ML global monthly fire location product, which provides the geographic location, date, and additional information for

---

<sup>6</sup> [https://lpdaac.usgs.gov/dataset\\_discovery/modis/modis\\_products\\_table/mcd64a1\\_v006](https://lpdaac.usgs.gov/dataset_discovery/modis/modis_products_table/mcd64a1_v006)

each 1 km fire pixel detected by the Terra and Aqua MODIS sensors on a monthly basis. Fires that are actively burning at the time of the satellite overpass (and under relatively cloud-free conditions) are detected using the contextual algorithm described by (Giglio *et al.*, 2003). The MODIS Active Fire Product has been validated against coincident high-resolution ASTER data (Morisette *et al.*, 2005; Csiszar, Morisette and Giglio, 2006; Giglio *et al.*, 2008; Schroeder *et al.*, 2008; Giglio, Schroeder and Justice, 2016) as well as several other studies (e.g. de Klerk, 2008; Hawbaker *et al.*, 2008).

Table 2.1. Overview of burned area products selected for intercomparison (\* grid size at Equator)

Producer	Product	Sensor	Grid Size	Projection	Layer
European Commission	Copernicus Burnt Area	SPOT-VGT	1000 m*	Geographic	“FDOB_DEKAD”
European Space Agency	Fire CCI	MERIS	300 m*	Geographic	1 (“Date of first Detection”)
NASA MODIS Land Science Team	MCD45A1	MODIS	463.3 m	Sinusoidal	“Burndate”
NASA MODIS Land Science Team	MCD64A1	MODIS	463.3 m	Sinusoidal	“Burn Date”

## Methods

### Comparison Grid

Previous works which consider burned area products at yearly and subcontinental to global scales suffer from two limitations with regard to scale of analysis: generally, the spatial unit for analysis is too large to identify differences in the location of burn identifications (e.g. Boschetti *et al.*, 2004), and the temporal unit for analysis is too long to capture inconsistencies in the timing of burn identifications

(e.g. Giglio *et al.*, 2010). To address these issues, we implement a comparison grid of finer resolution both temporally and spatially through the use of the voxels described in the proceeding sections.

### Spatial Analysis Grid

Burning is reported by Thiessen Scene Area (TSA) polygon. The TSA is a tessellation of the Landsat World Reference System-2 (WRS-2) acquisition scheme which assigns each location on the Earth's surface to one WRS path/row combination (Gallego, 2005; Kennedy, Yang and Cohen, 2010). Overlapping path and row areas are therefore eliminated. TSA's have been used previously as the spatial sampling unit for burned area product validation (Padilla, Stehman and Chuvieco, 2014; Boschetti, Stehman and Roy, 2016).

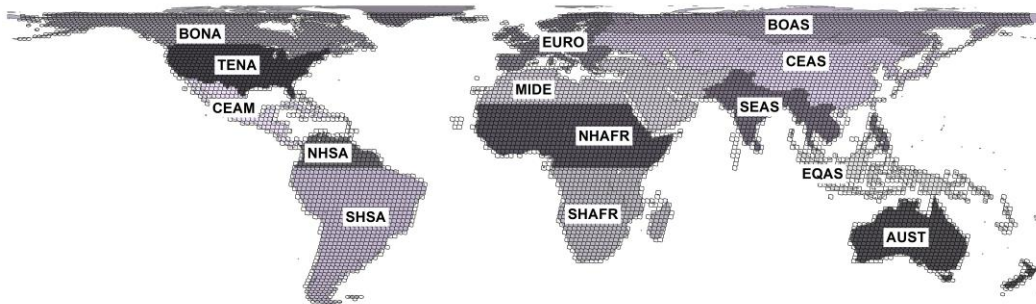


Figure 2.1. GFED fire regions with Thiessen Scene Area (TSA) polygons superimposed.

Results are also aggregated to fourteen large regions, herein referred to as fire regions, defined in the Global Fire Emissions Database (GFED) (Giglio *et al.*, 2006; van der Werf *et al.*, 2006). These regions are characterized by similarities in their climate and fire regime attributes and are suitable for emissions studies (van der Werf *et al.*, 2010) and fire activity reporting (Boschetti and Roy, 2008; Giglio *et al.*, 2010;

Giglio, Randerson and van der Werf, 2013). The larger scale of the fire regions relative to the TSA polygons enables analysis of trends that manifest at the larger regional scale (Figure 2.1).

### Temporal Comparison Grid

Several previous burned area product intercomparisons report burning as a yearly total, which has the undesirable effect of obscuring the temporal inconsistencies in the products. However, the compositing periods of the selected burned area products are dekadal (Copernicus Burnt Area) or monthly (Fire CCI, MODIS MCD45A1, MODIS MCD64A1), allowing for a higher temporal resolution in this study. By dividing the world into a set of TSA tiles geographically and temporally in fixed intervals, a voxel concept is used to assign each burned pixel to a TSA polygon in space and time (Boschetti, Stehman and Roy, 2016). Two temporal grids are used in this study: a finer monthly grid and a quarterly grid used to highlight seasonal patterns.

### Data Preprocessing

For each burned area product, all burned grid cells are assigned to a corresponding TSA voxel based on their spatial location and product's day of burning. For the Fire CCI and Copernicus Burnt Area products, which are distributed in the geographic projection, determining the burned area for each TSA polygon in a geographic projection requires special consideration for the effect of latitude. To compensate for the variation in cell size, the contribution of each cell was adjusted using a cosine weighting factor and assuming an Earth radius of 6371 km.

The MCD45A1 and MCD64A1 products are generated in the equal-area sinusoidal projection, thus the total burned area is simply the number of burned grid cells multiplied by the cell area (21.46 ha). These values were recorded for each TSA tile in the overlapping product coverage for each month throughout the 2005 to 2011 study period.

We elected to process the amount of area burned per TSA polygon in the native pixel size, adjusting for the effects of latitude as necessary i.e. for the products distributed in the geographic projection. We acknowledge that small errors may be introduced along the edges of the polygons, however, this decision reduces the error propagated by resampling and projecting the data from its original format.

For analysis purposes, each TSA polygon is also associated with a fire region if its centroid is contained by the region. Each dataset is therefore summarized on a per-voxel basis and associated with a fire region as appropriate for the seven-year study period.

### Data Analysis

#### Burned Area Totals

The simplest indicator of burned area algorithm performance is the burned area total per month and per year. Although summaries of burning are generally not sufficient for assessing performance, such summaries are useful for identifying trends from year-to-year. The annual burned area totals were calculated globally and for each fire region over the seven-year study period on a monthly and yearly basis.

### Scatterplots

The relative amount of burning for each product is summarized at a finer temporal resolution (monthly and quarterly) by scatterplots of the TSA tiles overlapping the fire region. Scatterplots are generated to compare two products at a time in four different cases: global yearly burning totals, global monthly burning totals, region-specific yearly burning totals, and region-specific monthly burning totals.

A total least squares (TLS) regression is calculated for each scatterplot as well as the root mean square error (RMSE). TLS regression models are appropriate for product intercomparison because the model assumes no dependency of the variables, thus the result of the regression does not depend on the arbitrary choice of axis assignment. The slope of the regression line is an indication of the relative burned area identification bias of two products. The RMSE of the distribution is used as an indicator of the dispersion of the burned area proportions, or the tendency of the classifiers to identify the same amount of burned area across voxels.

Both the TLS regression slope (and offset) and RMSE are necessary to determine if there is a bias between products and the degree to which burn detections are co-located. Based on the interrogation of the scatter plots, individual Landsat scenes can be selected for further investigation, particularly for scenes where one product identifies a large amount of burning and the other identifies very little.

### Temporal Heat Maps

Active fire detections are known to have very low commission errors (Schroeder *et al.*, 2008; Giglio, Schroeder and Justice, 2016), hence they are an

independent indicator of the presence of fire activity in a given region at a given time, and can be used as a qualitative evaluation of the time of burning, independent of the intercomparison between burned area products (e.g. Boschetti *et al.*, 2010). MODIS active fire counts were aggregated according to the same voxel scheme described above; for each month and fire region, a heat map is calculated indicating the burned area identified by each product compared to the number of active fire detections. Heat maps can be used to identify whether burn detections are temporally coincident with active fire detections throughout the entire time series.

### Results

The results of our intercomparison are presented in the following subsections. Due to the scale of this study in terms of the number of products analyzed and the length of the time series, it is not possible to reproduce all of the results here. Rather, in addition to summary results for the entire study period, we consider 2006 as an example year for a more detailed comparison of the products, which provides examples of significant fire activity in Eastern Europe and Southeast Asia as well as typical fire activity in high-burning regions such as Africa and Australia. The systematic processing of the products should yield consistent results from year to year. Comparisons between products are made with respect to the MCD64A1 product because it is the most recently updated product generated operationally. The results for all years are made available in the supplementary materials.

## Overview

The total annual burned area detected globally and for each fire region by the four global burned area products is reported in Figure 2.4. In every year, the Copernicus Burnt Area product detected the least total amount of burned area while the Collection 6 MCD64A1 product detected the most. Summary statistics for each product are reported in Figure 2.2.

Overall, MCD64A1 detects the most total burned area throughout the study period, exceeding the totals detected by Copernicus, Fire CCI, and MCD45A1 by approximately 90%, 25%, and 21%, respectively. Conversely, the Copernicus Burnt Area Product detects the least amount of burned area throughout the study period, trailing the estimated burned area from Fire CCI, MCD45A1, and MCD64A1 by approximately 52%, 56%, and 90%, respectively. The total burned area detected by Fire CCI and MCD45A1 is similar (within 2% global burned area), however, this does not capture the significant differences in the spatial location of the burn identifications. Yearly global burned area totals shown in Figure 2.3 indicate that the Fire CCI, MCD45A1, and MCD64A1 products do not demonstrate a robust trend in burned area throughout the seven-year study period. On the other hand, the Copernicus Burnt Area product detects noticeably less burned area through time.

Product	AUST	BOAS	BONA	CEAM	CEAS	EQAS	EURO	MIDE	NHAFR	NHSA	SEAS	SHAFR	SHSA	TENA	Total
2005															
Fire_eoi	197,697	41,638	10,162	36,853	143,851	11,287	11,378	3,989	1,373,498	10,215	163,843	1,443,717	174,276	25,033	3,647,417
Copernicus	253,491	284,857	139,158	48,236	375,910	1,545	46,616	87,343	634,456	9,934	61,886	716,319	191,924	202,113	3,053,759
MCD45A1	183,281	34,095	18,597	20,448	202,689	786	8,287	13,367	1,549,924	6,015	104,898	1,298,115	181,340	28,526	3,651,379
MCD64A1	257,491	62,309	29,708	43,241	269,634	9,525	9,803	10,919	1,623,712	55,311	135,034	1,643,509	348,986	27,769	4,526,952
2006															
Fire_eoi	305,026	77,334	13,873	16,106	152,985	10,268	9,869	8,330	1,285,967	12,886	113,384	1,202,970	110,001	29,470	3,348,467
Copernicus	200,635	215,238	161,263	44,603	300,379	2,144	35,768	65,038	486,389	8,240	41,226	597,096	146,414	194,898	2,499,331
MCD45A1	457,150	76,290	14,008	13,716	228,993	1,728	13,819	16,076	1,262,566	3,474	79,043	1,294,551	113,435	38,440	3,613,290
MCD64A1	552,857	84,070	18,943	23,281	277,579	31,512	8,995	13,206	1,333,122	47,072	114,756	1,492,447	233,008	36,860	4,267,709
2007															
Fire_eoi	396,824	41,563	7,706	12,479	112,796	6,133	13,938	5,889	1,612,555	18,303	170,377	1,337,405	258,288	33,302	3,967,559
Copernicus	257,158	147,981	109,273	42,175	228,732	1,278	39,366	51,503	499,063	11,313	39,277	607,874	188,438	168,217	2,391,647
MCD45A1	386,241	52,548	9,719	10,362	202,572	998	14,942	14,541	1,388,687	22,308	87,923	1,197,919	308,943	32,412	3,730,117
MCD64A1	488,582	58,901	15,527	25,788	215,597	4,810	12,596	13,637	1,454,481	70,997	172,773	1,535,345	487,228	38,170	4,594,432
2008															
Fire_eoi	231,836	132,251	11,990	20,950	159,947	7,232	14,690	4,728	1,436,391	36,592	116,382	1,353,881	192,352	31,050	3,750,272
Copernicus	177,386	149,467	90,454	40,457	200,843	998	27,904	49,356	487,847	7,120	33,434	532,476	131,361	130,224	2,059,329
MCD45A1	275,846	140,131	8,620	12,609	245,160	753	11,021	5,932	1,260,978	5,447	72,181	1,262,697	151,614	21,528	3,474,516
MCD64A1	297,191	169,826	14,890	23,716	260,116	3,762	12,664	8,770	1,373,280	56,833	113,191	1,587,314	256,845	27,740	4,197,138
2009															
Fire_eoi	337,036	61,707	12,175	7,267	124,705	15,293	10,043	9,014	1,338,088	1,346	145,481	1,162,909	79,756	25,301	3,330,122
Copernicus	161,737	177,420	112,202	34,700	210,049	1,397	28,193	47,709	400,867	6,663	44,024	530,309	134,919	151,594	2,011,754
MCD45A1	328,104	77,720	7,111	13,578	149,387	899	7,305	23,091	1,213,645	4,925	122,342	1,165,002	58,366	24,981	3,196,454
MCD64A1	384,205	72,444	13,434	26,424	170,087	18,773	6,338	19,056	1,198,957	51,801	164,051	1,472,066	156,548	23,655	3,774,930
2010															
Fire_eoi	123,266	57,560	22,138	687	113,186	1,509	7,979	13,459	995,140	2,645	181,482	1,202,176	93,800	19,943	2,834,970
Copernicus	170,021	107,966	134,887	29,028	206,153	591	21,502	52,032	393,088	6,027	40,201	479,887	127,926	101,667	1,370,977
MCD45A1	112,898	47,649	23,905	7,129	215,339	248	6,138	27,967	1,045,553	13,729	112,830	1,375,163	331,891	19,203	3,339,042
MCD64A1	173,692	71,516	26,735	18,035	219,991	3,679	7,463	19,122	1,163,975	47,633	170,823	1,693,682	500,197	22,252	4,138,795
2011															
Fire_eoi	502,498	63,725	14,731	49,316	52,260	5,335	14,953	9,802	1,189,420	1,405	102,930	1,114,941	39,492	43,273	3,204,852
Copernicus	261,133	188,224	92,835	22,019	132,915	958	25,765	34,381	409,854	3,743	26,429	522,424	106,467	112,406	1,909,552
MCD45A1	671,208	74,380	10,541	23,687	117,175	561	9,704	15,713	1,194,287	6,986	94,556	1,339,858	125,893	38,456	3,723,006
MCD64A1	859,861	105,001	16,429	42,180	113,904	9,090	9,947	15,447	1,276,190	34,827	121,141	1,680,001	226,351	42,568	4,552,937

Figure 2.2. Yearly burned area totals (km<sup>2</sup>) per fire region and globally. Bar plot size is normalized to the maximum of the fire region across all products and all years.

Concerning individual fire regions, the Copernicus Burnt Area product shows evident and significant discrepancies from the other products. Specifically, it identified significantly less burned area in the regions which contribute most to the global burned area total i.e. Southern- and Northern-Hemisphere Africa (SHAF, NHAF), while detecting significantly more burned area than the other products in zones such as Boreal Asia (BOAS), Boreal North America (BONA), Temperate North America (TENA), Europe (EURO) and the Middle East (MIDE) which, according to the other three burned area products as well as previous studies, do not contribute significantly to global burned area totals.

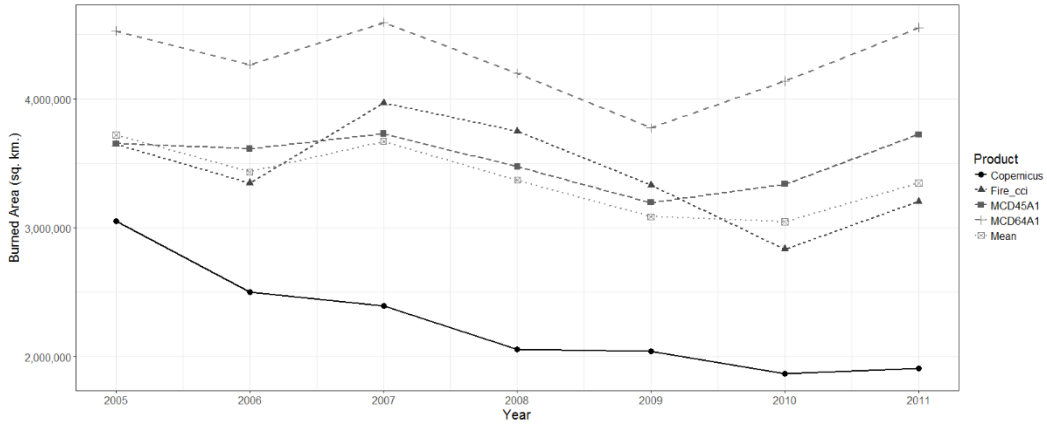


Figure 2.3. Total burned area identified per year by each product.

The magnitude of these differences is illustrated in Figure 2.4, which illustrates, per fire region, the proportion of total burning detected by each product normalized to the region’s maximum. Noteworthy outliers for the Fire CCI product include Equatorial Asia (EQAS) and Northern Hemisphere South America (NHSA). The Copernicus product identifies more burning than the other three products combined in four regions: TENA, BONA, EURO, and MIDE.

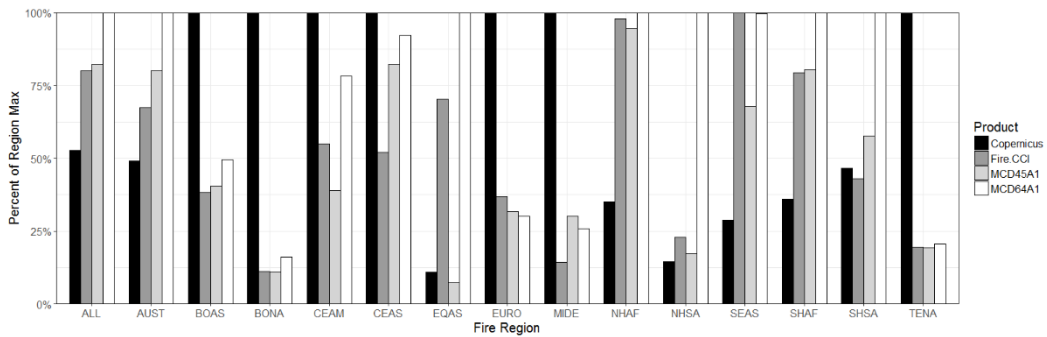


Figure 2.4. Percent of burned area detected per fire region, normalized to the maximum amount of burned area identified by any product in the respective fire region (2005 - 2011).

While the magnitude of the burning detected is an important indicator of a product’s performance, it is equally important to consider the temporal aspect of burning. The time of burning is captured in Figure 2.5 and Figure 2.6, which compares the burned area detected in a calendar month by the four products to the

MCD14ML Active Fire product, which is known to be a good indicator of the timing of the burning season. For most fire regions, the Fire CCI, MCD45A1, and MCD64A1 products show strong agreement with the temporal pattern of the MCD14ML detections. However, the Copernicus Burnt Area product shows temporal patterns, unlike the other three products. In particular, regions which show high seasonal variability such as Temperate North America (TENA), Central America (CEAM), and Europe (EURO) appear to be out of phase, which is to say the burning identified by the Copernicus Burnt Area algorithm corresponds to times when there are few or no coinciding active fire detections. In regions characterized by strong fire signals, such as the Southern Hemisphere Africa (SHAF) and Northern Hemisphere Africa (NHAF), there is strong agreement amongst all products with regard to timing, however, there are variations in the magnitude of burning. It is also noteworthy that for Equatorial Asia (EQAS), a region characterized by extensive cloud cover for much of the year, only those algorithms that use active fire detections as an input, Fire CCI and MCD64A1, identify any appreciable amount of burning.

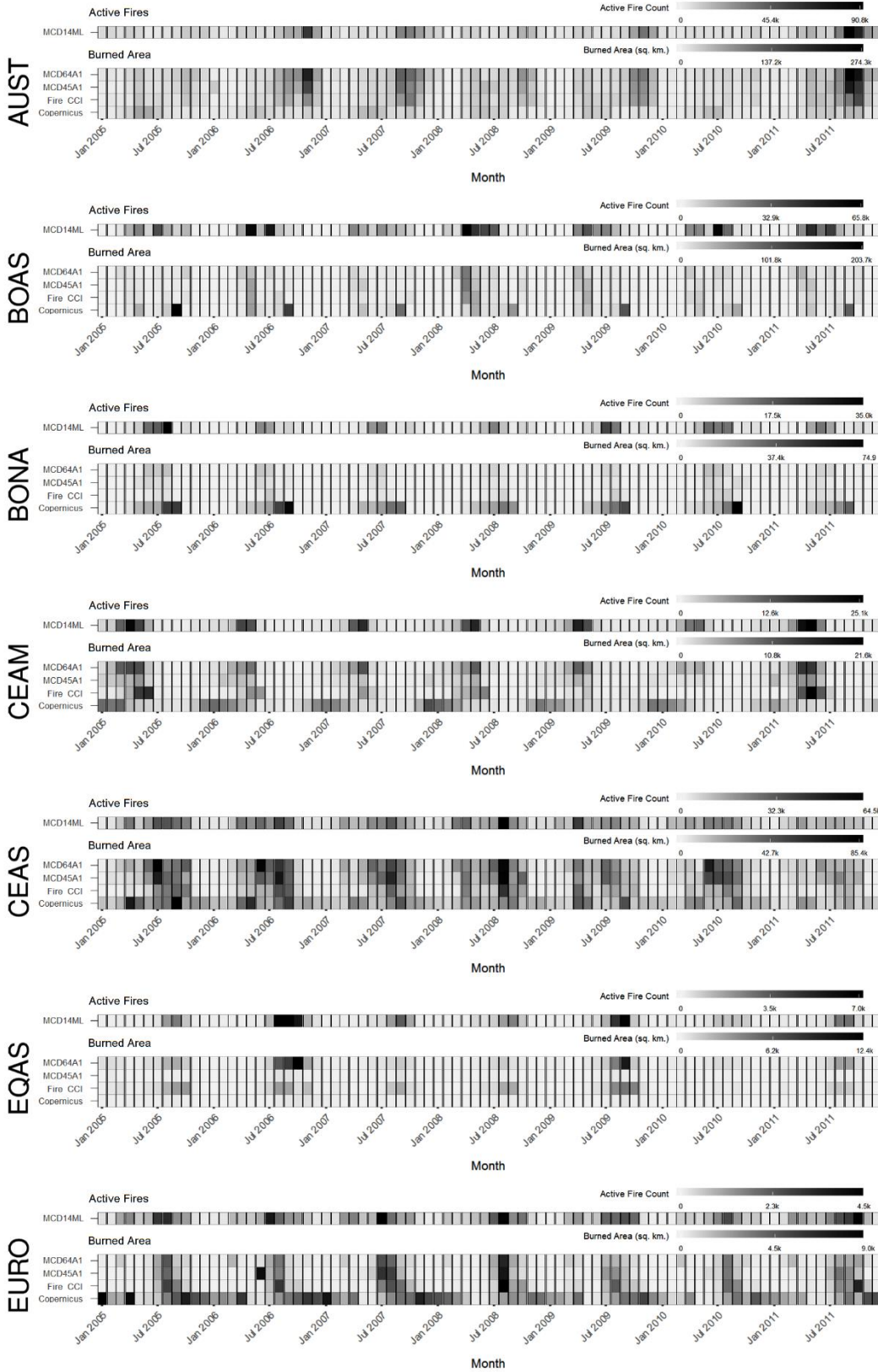


Figure 2.5. Comparison of the timing of active fire detections with burned area detections (Australia - Europe).

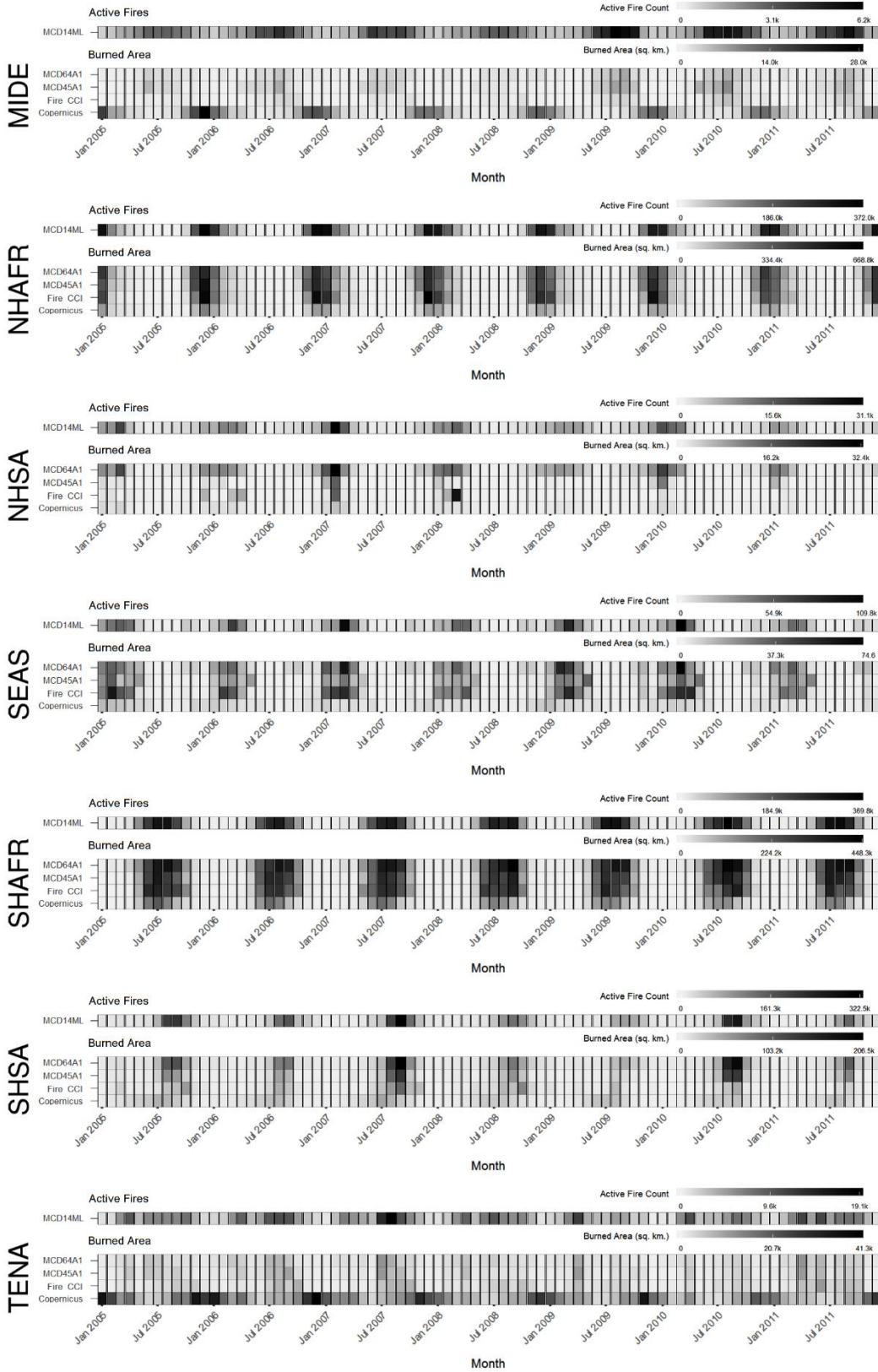


Figure 2.6. Comparison of the timing of active fire detections with burned area detections (Middle East - Temperate North America).

These results demonstrate that the burned area products have large variations spatially and temporally, even though similar burned area totals may be reported by the different products, as is particularly the case for Fire CCI and MCD45A1.

The following sub-sections will focus on some specific discrepancies between products, highlighting some of the differences in spatial and temporal burning patterns. These analyses are focused on 2006, which was chosen due to the presence of notable fire activity in Eastern Europe and Southeast Asia, in addition to typical fire activity in high-burning regions such as Africa and Australia.

#### Fire CCI and MCD64A1 Comparison

As shown in Figure 2.2, in 2006 the MCD64A1 product detects more burned area than the Fire CCI in every fire region except EURO. Globally, MCD64A1 identified 919,241 km<sup>2</sup> burned area more than Fire CCI, though most of this difference – about 77% – can be attributed to the four regions which burned the most: AUST, CEAS, NHAf, and SHAF. Across all fire regions, the temporal patterns of Fire CCI and MCD64A1 are generally in agreement with the MCD14ML Active Fire detections (Figure 2.5, Figure 2.6). Interestingly, in some cases, the Fire CCI detections appear to identify longer burning periods than the MCD64A1 detections by a month for regions which do not experience large amounts of burning such as EURO, EQAS, and CEAM, though this is generally not the case in 2006 (Figure 2.5, Figure 2.6).

Regarding the difference in burned area detected per TSA polygon, there are some spatial manifestations of the classifier tendencies. The results from 2006 are illustrated in Figure 2.7. TSA's where MCD64A1 identifies greater burned area than

Fire CCI are more prevalent, as is to be expected given the tendency of the former to identify more area as burned throughout the study period. However, there is spatial clustering of occurrences where the Fire CCI product identifies more burned area that tends to be consistent from year-to-year.

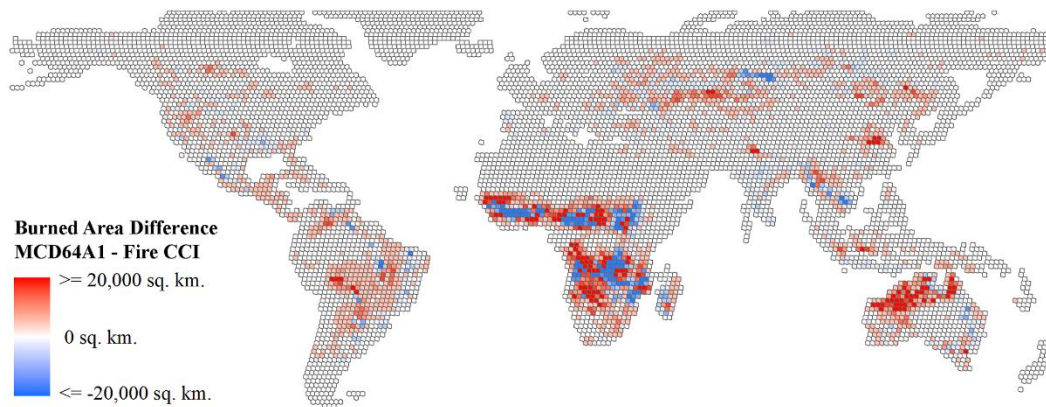


Figure 2.7. Maximum differenced burned area totals per TSA for 2006 between MCD64A1 and Fire CCI. Each cell indicates the greatest difference between concurrent months in the year, with darker blue indicating higher Fire CCI totals and darker red indicating higher MCD64A1 totals.

The four TSA points highlighted in Figure 2.8 represent the four instances where the Fire CCI product detects more than 2000 km<sup>2</sup> burned area than the corresponding MCD64A1 result. Each belongs to the Eastern Europe burning event within Novosibirsk Oblast, Russia described in (Chuvieco *et al.*, 2016), who claim that the Fire CCI product correctly detected this burning event while GFED4 (i.e. MCD64A1 Collection 5.1) missed the burns in their entirety. Using the spatial and temporal comparison grid described previously, we investigate this event to determine whether the Collection 6 MCD64A1 product is able to capture this event as well as verify the Fire CCI ability to correctly identify the burning episode.

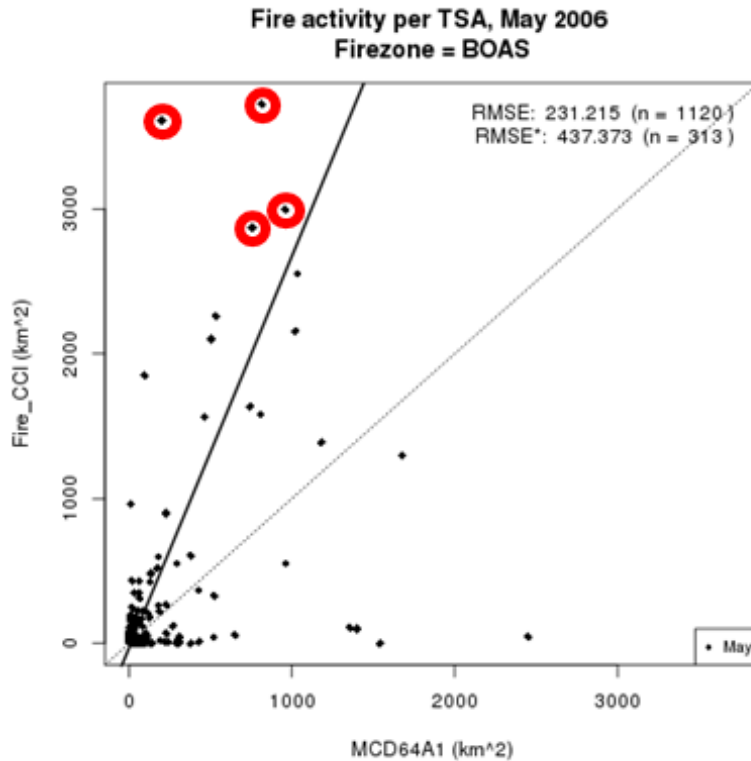


Figure 2.8. Scatterplot for Boreal Asia (BOAS) in May 2006 illustrating burned area detected per TSA polygon for Fire CCI and MCD64A1. The four circled points represent the largest difference in burned area detected between Fire CCI and MCD64A1 and coincide with the burning events described in Chuvieco et al. (2016).

The corresponding Landsat scenes and coarse-resolution burned area detections are shown in Figure 2.9. This evidence corroborates the claim that the Fire CCI product identifies the burning episode while MCD64A1 continues to mostly omit it in the Collection 6 version of the product.

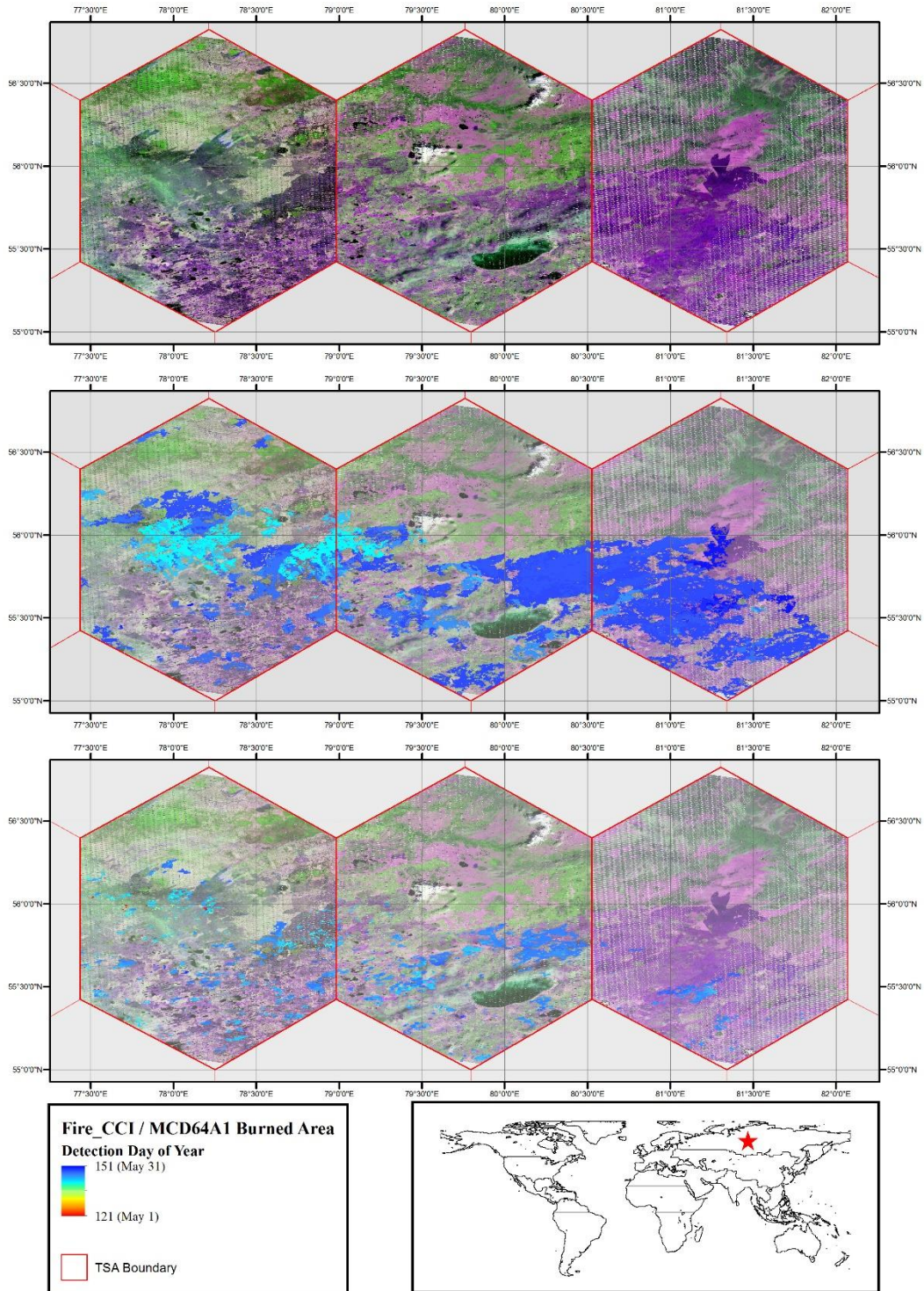


Figure 2.9. Comparison of Eastern Europe burning episode, May 2006. Top: Best available Landsat imagery, from left to right - Path 152 Row 21 (Landsat 5, May 12, 2006); Path 151 Row 21 (Landsat 7, June 6, 2006); Path 150 Row 21 (Landsat 7, May 30, 2006) with SWIR1-NIR-SWIR2 composite. Middle: Fire CCI burned area for May 2006. Bottom: MCD64A1 burned area for May 2006.

In addition to this, we investigate a particularly heterogeneous area in the Northern Hemisphere Africa which is characterized by large differences in the reported burned area. By comparing the values from the TSA scatterplot in Figure 2.10, it is clear that while there is relatively little bias (indicated by the slope of the TLS regression) between the estimates from the two products in January 2006 for NHAF, there are noteworthy cases where one product detects much more burned area than the other. At the fire region scale, these commissions and omissions balance one another, causing the TLS regression to show a near one-to-one correspondence, indicating low bias in the estimate for the fire region. However, the lack of bias in the regression model is not necessarily indicative of agreement between the two products. As shown in the same figure, the regression value is similar to that of the MCD45A1 and MCD64A1 comparison for the same voxel, however, the lower RMSE indicates that there is generally better spatial agreement between the products and the likelihood of overlap within voxels is greater.

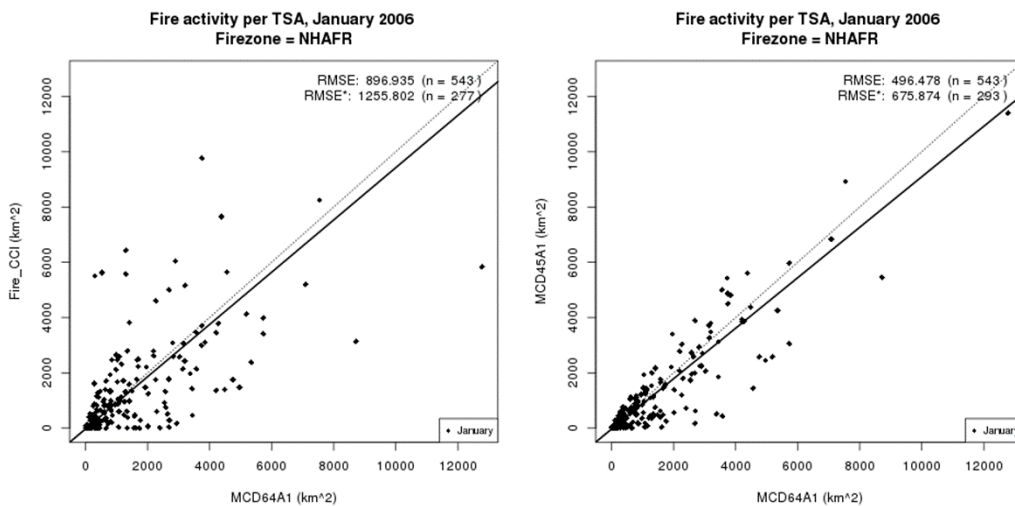


Figure 2.10. Scatterplots for Northern Hemisphere Africa (NHAF) in January 2006 illustrating burned area detected per TSA polygon for Fire CCI (left) / MCD45A1 (right) and MCD64A1. Note that while the slope is similar, the RMSE is much greater for the CCI plot.

From inspection at the native resolution, it is clear that the Fire CCI product suffers from the presence of large artifacts that coincide with the edges of processing tiles. The artifacts lead to large swaths of burning occurring during a single day of the year and dominate the majority of the overlapping TSA, as illustrated in Figure 2.11.

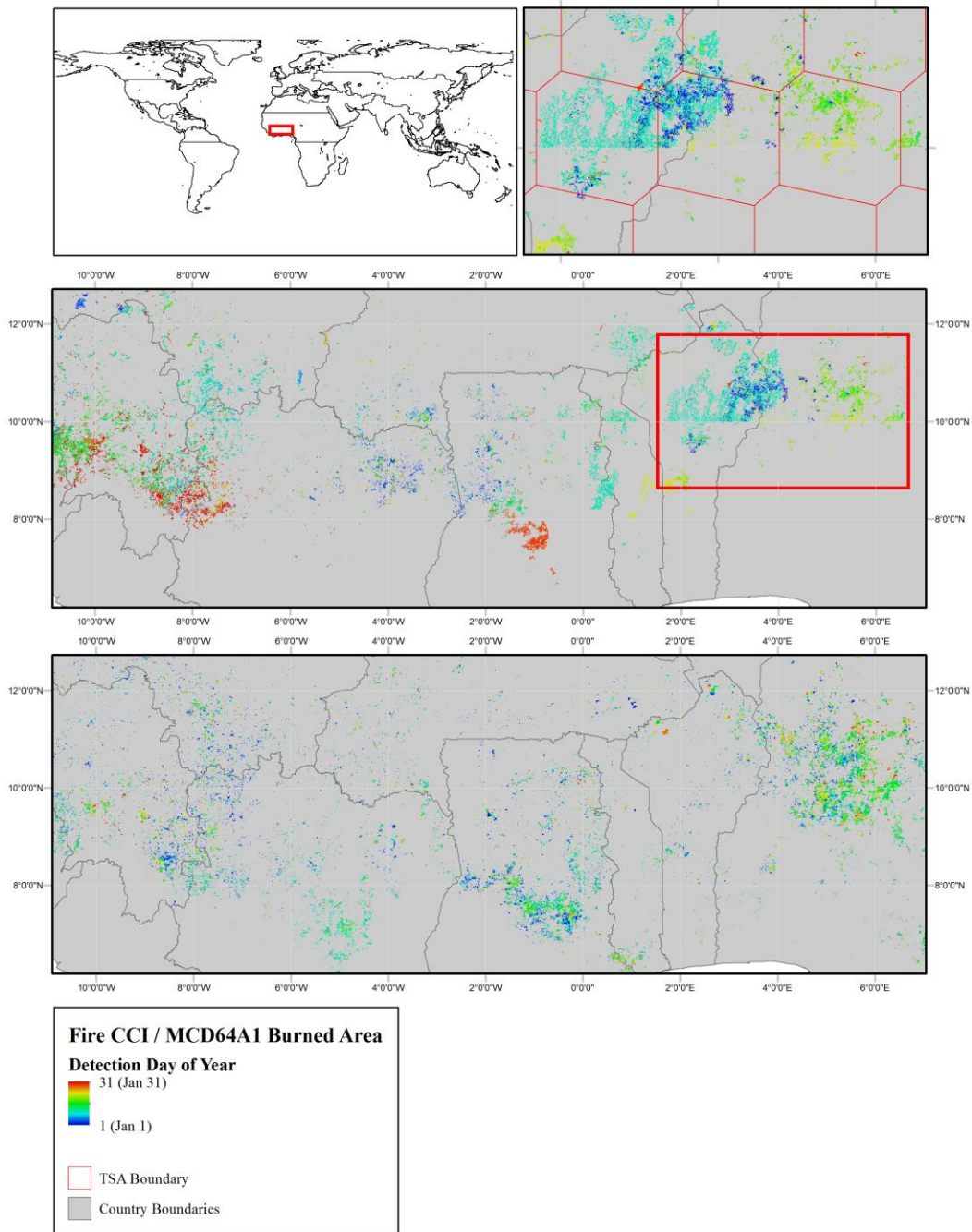


Figure 2.11. Example of artifacts introduced by the region growing procedure in the Fire CCI product. Western portion of NHAFR, January 2006.

## Copernicus Burnt Area and MCD64A1 Comparison

The Copernicus Burnt Area shows little relationship to the other burned area products both spatially and temporally. On a global and annual basis, the product detects the least amount of burned area by a significant amount (Figure 2.2) and as previously mentioned, generally detected less burned area in successive years throughout the study period. In 2006, the Copernicus areal estimates were similar to the other three products for CEAS, NHSA, and SHSA while in the remaining ten fire regions the Copernicus product detects either more than twice as much burning as the other products or less than half of the other products (Figure 2.2).

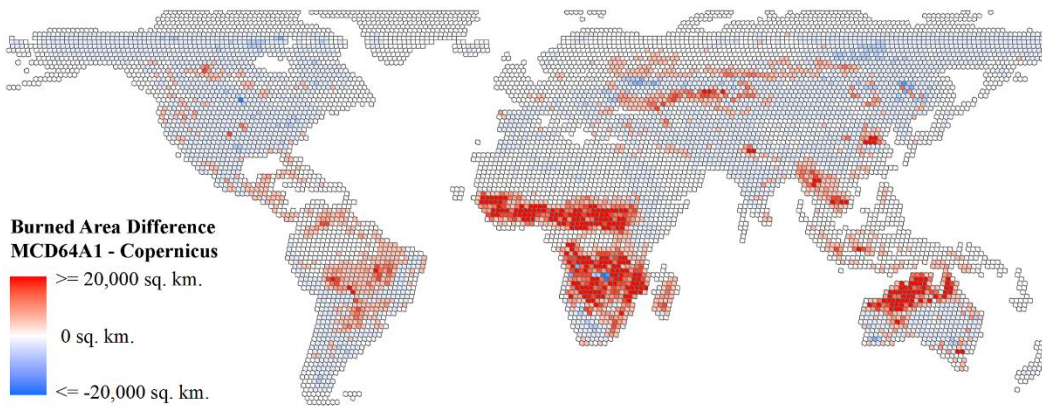


Figure 2.12. Maximum differenced burned area totals per TSA for 2006, MCD64A1 and Copernicus Burnt Area. Each cell indicates the greatest difference between concurrent months in the year, with darker blue indicating higher Copernicus Burnt Area totals and darker red indicating higher MCD64A1 totals.

The timing of these burns also tends not to coincide with MCD14ML detections throughout the year, with some extreme cases, such as CEAM, EURO, MIDE, and TENA indicating that burning is out of phase with the active fire detections, i.e. the burned area product indicates burning when there is no burning and *vice versa* (Figure 2.5, Figure 2.6).

As shown in Figure 2.12, the Copernicus product identifies small amounts of burning in most TSA's globally. Relative to MCD64A1, this results in lower levels of

burning identified in greater burning regions but higher levels of burning identified in lesser burning regions. In the high northern latitude regions, BONA and BOAS, the Copernicus product detects large amounts of burning in August and September for the former region and September for the latter. While both regions still exhibit a small degree of burning in August (Giglio, Randerson and van der Werf, 2013), September is well beyond the peak of fire activity in these areas. Given the design of the algorithm and the timing of the detections, it is possible that the identifications are false positives resulting from slight variations in the rapid decrease in NDVI due to leaf senescence and abscission. The spatial extent of the burn classifications in eastern Russia can be seen in Figure 2.13 (the areas identified in western CEAS by both products is a wheat-producing region where agricultural residue burning is a common practice during this time of the year).

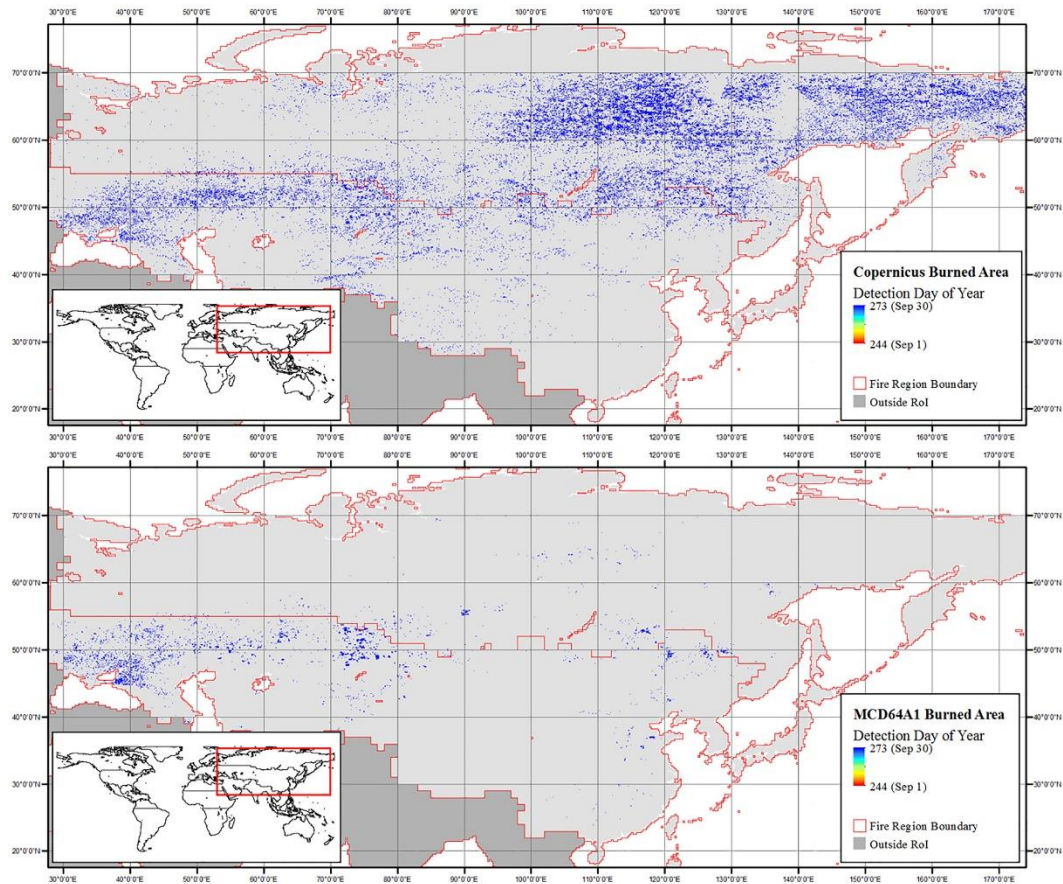


Figure 2.13. Burned area identifications for Copernicus (top) and MCD64A1 (bottom) in September 2006 for BOAS and CEAS, aggregated to 6 km grid cell (maximum value aggregation).

In Australia, which contributes significantly to global burned area totals, the out-of-phase burn identifications shown in Figure 2.5 are corroborated by Figure 2.14 and Figure 2.15. Noting that the majority of fire activity in AUST occurs between August and December, while very little fire activity occurs between January and July (Giglio, Randerson and van der Werf, 2013), the small amounts of fire detected in June can generally be attributed to commission errors while the extent of burning observed in November is much lower for the Copernicus Burnt Area product than the MCD64A1 product. With respect to the expected duration of the 2006 fire season, MCD64A1 identified approximately 68,448 km<sup>2</sup> area burned between January and

July and 508,781 km<sup>2</sup> area burned between August and December while Copernicus identified approximately 124,238 km<sup>2</sup> and 81,040 km<sup>2</sup>, respectively.

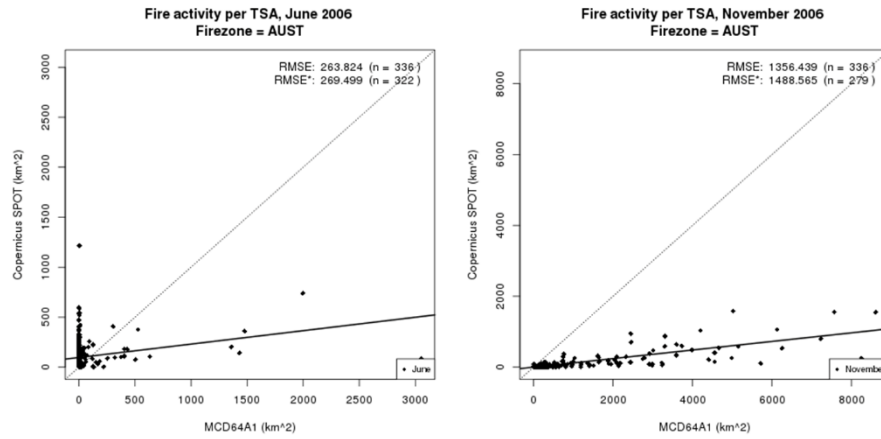


Figure 2.14. Scatterplot of burned area per TSA in AUST, June (left) and November (right) 2006. Copernicus (y-axis) detects less burning per TSA but, in June, more TSA's with burning.

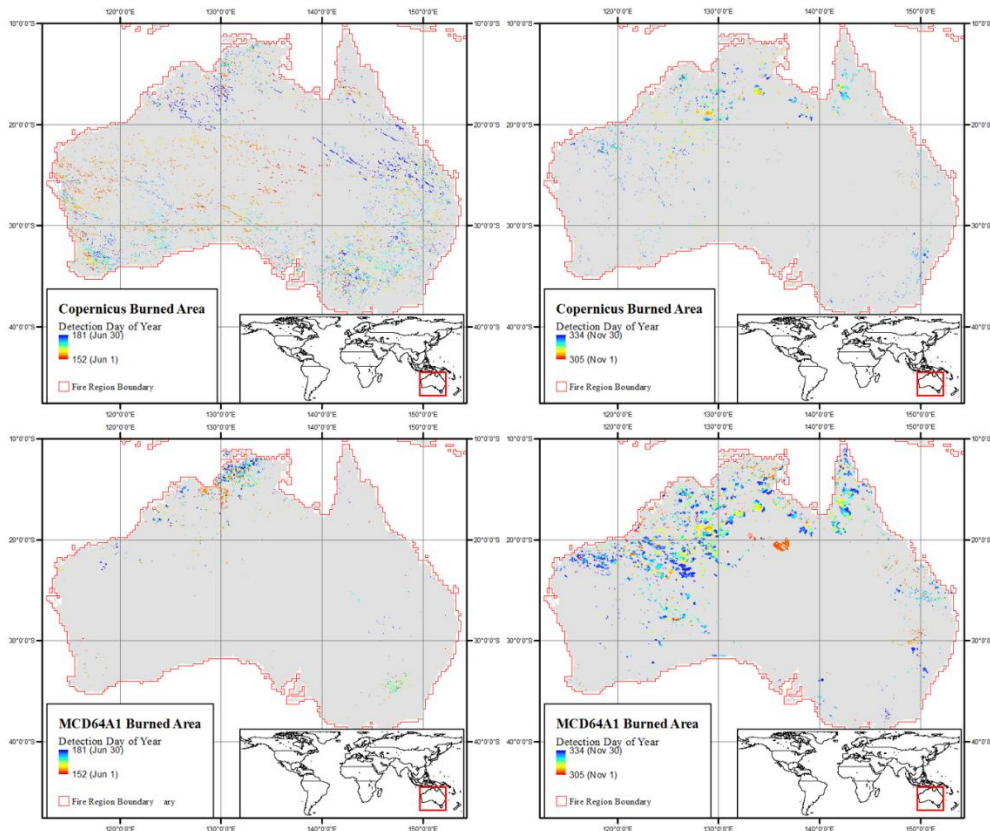
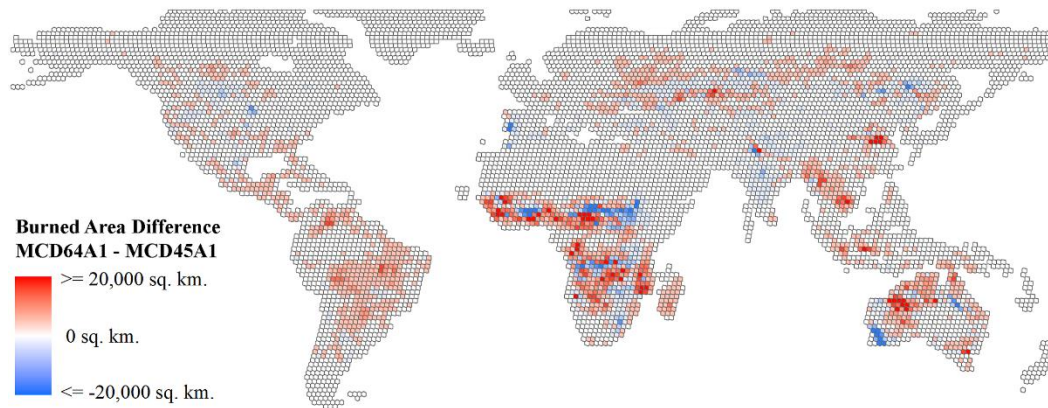


Figure 2.15. Burned area identifications for Copernicus (top) and MCD64A1 (bottom) in June (left) and November (right) 2006 for AUST, aggregation to 6 km grid cell (maximum value).

## MCD45A1 and MCD64A1 Comparison

Consistent with other years, for 2006 MCD45A1 detected more burning than Copernicus Burnt Area, a similar amount of burning compared to Fire CCI, and less burning than MCD64A1. Also like Fire CCI, the timing of the burn detections agrees with MCD14ML, though the pattern is slightly more consistent with the active fire detections.



*Figure 2.16. Maximum differenced burned area totals per TSA for 2006, MCD64A1 and MCD45A1. Each cell indicates the greatest difference between concurrent months in the year, with darker blue indicating higher MCD45A1 totals and darker red indicating higher MCD64A1 totals.*

In eleven of the fourteen fire regions, MCD45A1 identifies less area as burned than MCD64A1, the exceptions being EURO, MIDE, and TENA. The spatial distribution of differences between MCD45A1 and MCD64A1 is similar to that of Fire CCI and MCD64A1. In 2006, the differences in SHAF are similar in location, albeit smaller in magnitude, to the Fire CCI differences (Figure 2.16). This is evident in the scatterplots (Figure 2.17), which show that while there are differences in the burned area detected per TSA, the RMSE of these errors during the burning season tends to be smaller for MCD45A1 and MCD64A1 than for Fire CCI and MCD64A1.

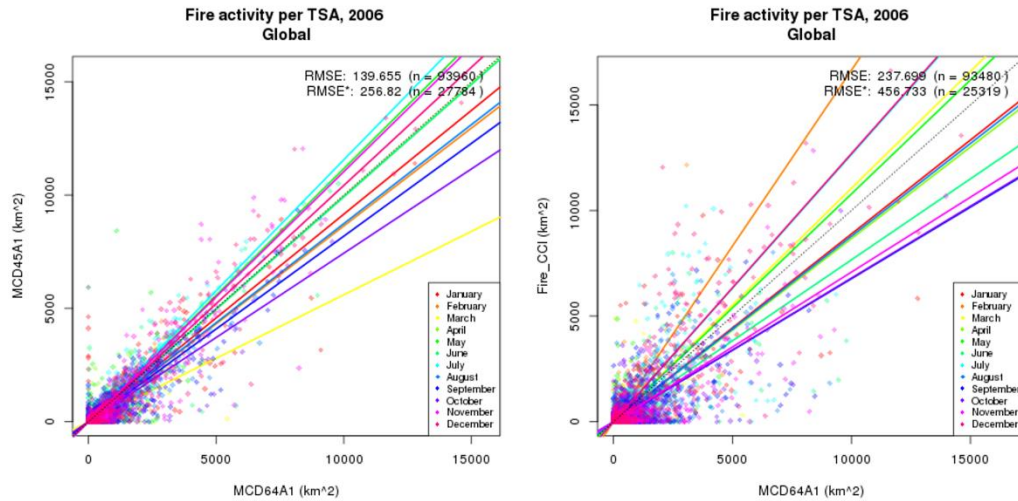


Figure 2.17. Example scatterplots of global TSA Burned Area totals for MCD64A1 vs. MCD45A1 (left) and Fire CCI (right). While the TLS regression slopes are similar, the RMSE of the global distribution is greater for Fire CCI.

There are instances where MCD45A1 differs greatly from MCD64A1. For the 2006 focus period, there is a notable presence of burned area detected in the southern portion of Western Australia which is detected by MCD45A1 and not MCD64A1. This detection in January coincides with the location of wheat in the province and is likely due to harvest, not burning. This is supported by Figure 2.18, which shows no coinciding active fire detections in the area labeled as burned. This is also evident in the scatterplot which shows large amounts of burning detected by MCD45A1 corresponding no active fire detections. This type of commission error was observed again in December 2007 in the same region.

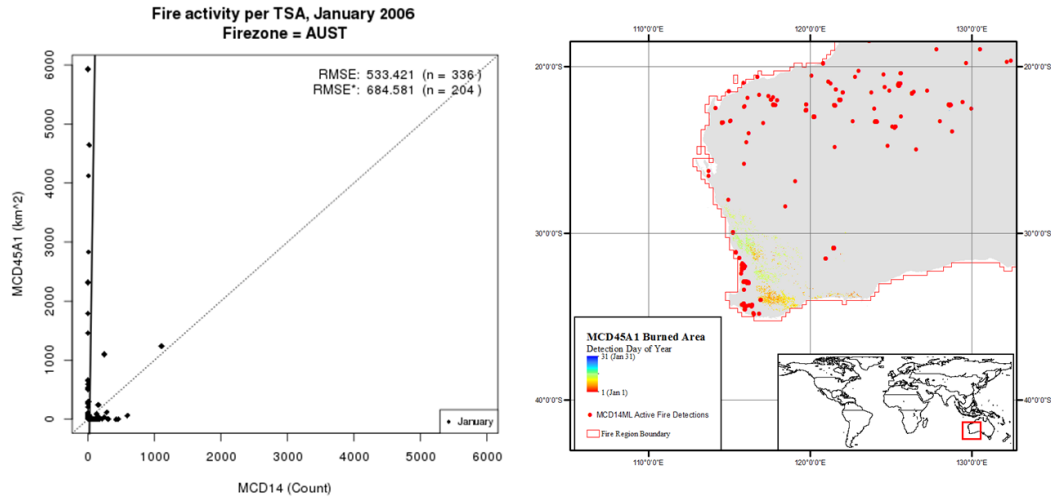


Figure 2.18. AUST Jan 2006. (Left) Scatterplot of MCD45A1 Burned Area per TSA vs MCD14ML Active Fire count per TSA; note the burned area totals associated with no active fire detections. (Right) Map of MCD45A1 burn identifications and MCD14ML active fire detections.

Fires observed in Kalimantan, Indonesia (EQAS) in October 2006 went undetected or grossly underestimated by MCD45A1, Fire CCI, and Copernicus Burnt Area, likely due to persistent cloud cover in the region resulting from the start of the rainy season. Using the voxel scheme, we observe that the majority of the burning occurred in only two TSA's during the burning episode. While MCD64A1 was able to some of the burned area, MCD45A1 identified only a few isolated pixels as burned (Figure 2.19). This result is in keeping with the results throughout the entire study period for the four burned area products tested in this intercomparison, MCD45A1 classifies the least amount of burning in EQAS every year while MCD64A1 classifies the most amount of burning in EQAS for the majority of years. This pattern is also observed in CEAM, which shares similar climate and cloud cover traits with EQAS, indicating that the MCD64A1 algorithm is more robust with respect to cloud cover than the MCD45A1 algorithm which requires more clear observations during the inversion period in order to identify an area as burned.

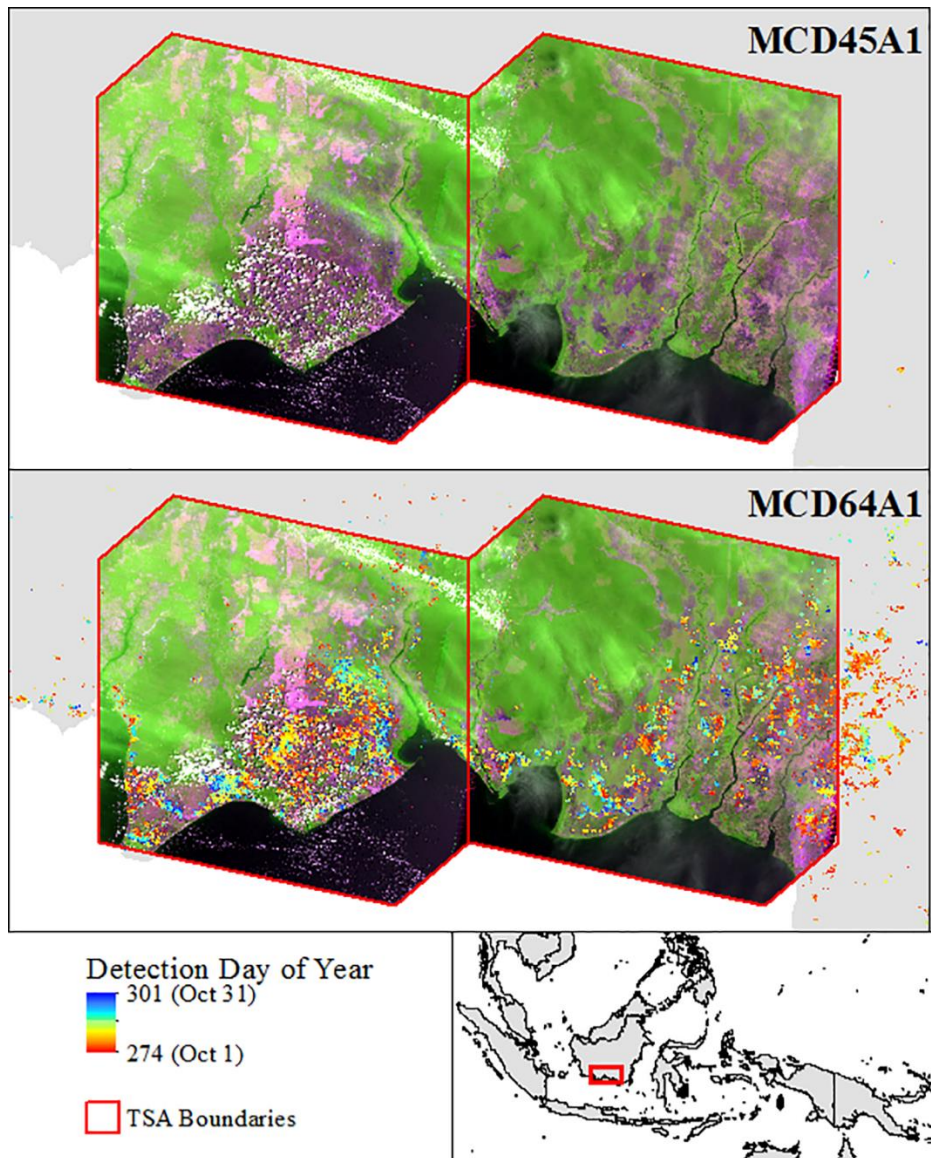


Figure 2.19. October 2006 EQAS fires in southern Kalimantan, Indonesia. MCD45A1 (top) and MCD64A1 (bottom) detections overlaid on Landsat 5 scenes path/row 118/062 (Oct 29, 2006; right) and 119/062 (Nov 5, 2006; left) with SWIR1-NIR-SWIR2 composite.

### Discussion and Conclusions

In this paper, through systematic intercomparison of four global burned area products, we have identified spatial and temporal similarities and differences in burned area detections between 2005 and 2011. The products - Copernicus Burnt Area, Fire CCI, MODIS Collection 5.1 MCD45A1, and MODIS Collection 6 MCD64A1 - are based on coarse spatial resolution (~300 m grid cell or larger) and high temporal resolution

(3 days or less revisit time) satellite data and are generated globally and systematically. The intercomparison procedure exploits a voxel concept to create an intercomparison grid, defined spatially by the Landsat Thiessen Scene Areas or TSA's (Gallego, 2005; Kennedy, Yang and Cohen, 2010), and temporally by calendar months. On a broader scale, fire regions are also used in order to better compare burning patterns under similar conditions (Giglio *et al.*, 2006; van der Werf *et al.*, 2006). While we focus on specific cases in 2006 for the analysis, all results are included in the supplemental material and the conclusions drawn can generally be applied to all years throughout the study period.

Global burning totals show that for each calendar year, MCD64A1 detected the most total burned area while Copernicus Burnt Area detected the least total burned area. The Fire CCI and MCD45A1 algorithms detected similar amounts of burned area each year throughout the study period, consistent with the results described by (Alonso-Canas and Chuvieco, 2015). The MODIS Collection 6 MCD64A1 dataset identifies over twenty-five percent more burning per year than its predecessor during the study period.

While Fire CCI, MCD45A1, and MCD64A1 showed similar patterns in yearly global total burned area detected per year, Copernicus Burnt Area detected progressively less burned area from 2005 to 2010, with only a slight increase in 2011 and smaller than the 2010-2011 increase identified by the other classifiers. At the time of writing, we are not aware of any systematic drift in the calibration of SPOT-Vegetation, pointing to a reduced sensitivity of the algorithm over time, possibly due to the algorithms use of a running vegetation index-based time series, which

introduces eccentricity into the time series as the dataset expands, requiring the algorithm to exceed a greater threshold in order to identify a pixel as burned.

The classifier tendencies diverge at the fire region level. In spite of identifying the least burned area globally, Copernicus Burnt Area identifies the most burned area in seven of the fourteen fire regions. However, these regions are typically responsible for relatively small contributions to the global burned area. For six of the remaining seven fire regions, MCD64A1 identified the most burned area over the seven-year study period. In persistently cloudy regions such as EQAS and NHSA, the long (16-day) inversion period required by MCD45A1 often results in burn omissions due to insufficient data resulting from cloud cover or aerosol content. In line with expectations, Fire CCI and MCD64A1 identify the most burned area in cloudy regions due to their reliance on active fire detections as training data samples.

Comparison with the MCD14ML Active Fire dataset indicates that while the burn timing of Fire CCI, MCD45A1, and MCD64A1 is similar to the pattern of active fire activity, the Copernicus Burnt Area is apt to detect burned areas outside of the normal burning cycle, with extreme examples in temperate climates such as EURO and TENA where the Copernicus detections are out of phase with the cycle of active fire detections. The consistency of these cycles at the fire region level combined with the algorithm's reliance on vegetation indices suggests that the Copernicus Burnt Area detections are related to the natural yearly growth and senescence cycles of the vegetation in the respective region. The timing of burning is important when considering fire cycles in modeling exercises because the spread of fire is known to be constrained by, amongst other factors, fuel (i.e. biomass) availability while the

emissions from burning are a factor of the biomass consumed. Errors in the timing of fire detection can have large effects on the biomass emissions estimates due to seasonal variations in precipitation and temperature which act as controls on fuel availability, combustion type (i.e. smoldering vs. flaming) and combustion completeness (Korontzi, Justice and Scholes, 2003; van Leeuwen and van der Werf, 2011).

Given that the use of the data sets often occurs at the local, national and regional scales (e.g. der Werf *et al.*, 2009; Leblon, Bourgeau-Chavez and San-Miguel-Ayanz, 2012; Loboda *et al.*, 2012; Rucker and Tiemann, 2012; Rossi *et al.*, 2016), it is important to generate products that exhibit reliable location, timing, and extent of burning. Intercomparison is, therefore, an important and practical tool for characterizing the relative performance of global burned area products in this regard as it allows for wall-to-wall coverage of the entire time series which is impractical, if not impossible to achieve, with current validation practices and protocols. As a result, it is able to capture burning events which are acute and anomalous which would otherwise be unlikely to appear in a random sample, such as the 2006 examples presented for Kalimantan, Indonesia (EQAS, October 2006) and Novosibirsk Oblast, Russia (BONA, May 2006).

Nonetheless, product intercomparison implicitly assumes that, as a whole, the products being compared provide a reasonable approximation of the conditions on the ground. For example, if all products omit burning in a region then there is no basis for investigating that region on a data-driven *a posteriori* basis. Intercomparison should, therefore, be recognized as an important tool in product evaluation that is

complementary to, rather than a replacement for, product validation. In this context, the recent study by (Boschetti, Stehman and Roy, 2016) provides some guidelines on procedures for validation of global burned area products.

Given the results of this intercomparison, which demonstrates that the four burned area products do not achieve a consensus on burn locations or timing, there is a clear need for standardization of satellite-derived burned area products and the reporting of their accuracies. Developing a comprehensive burned area validation data set to assess consistently the accuracy of multiple global products would be an important next step towards helping users assess which product is most appropriate for their application. In the meantime, users of any burned area product should take care to understand the nature of commission and omission errors of the product with regard to geographic location, timing of the burning season, and total amount of burning.

Future efforts based on this work and upcoming systematic validation exercises such as those described in (Boschetti, Stehman and Roy, 2016) and (Padilla *et al.*, 2017) focus on identifying sources of errors in publically available burned area products. While it is outside of the scope of the present work, understanding the source of these errors can be an important factor in users' selection of burned area products for input to other research efforts.

### Acknowledgments

This work was supported in part by NASA Grant # NNX14AI68G.

*Supplemental material*

The supplemental material provided contains a combination of all scatterplots described in this manuscript. The self-describing zip files contain charts for burned area aggregated globally and at the fire region level, where the unit for analysis is the Thiessen Scene Area (TSA) for the respective time period. Time periods consist of yearly, quarterly (Jan-Mar, Apr-Jun, July-Sep, Oct-Dec), and monthly windows. This archive is available from the original publisher, Taylor and Francis *International Journal of Digital Earth*, DOI: 10.1080/17538947.2018.1433727

## Chapter 3 – Assessing the Shape Accuracy of Coarse-resolution

### Burned Area Classifications

This work has been accepted for publication in *IEEE Transactions on Geoscience and Remote Sensing*: Michael L. Humber, Luigi Boschetti & Louis Giglio (*Accepted*) Assessing the shape accuracy of coarse-resolution burned area identifications, *IEEE Transactions on Geoscience and Remote Sensing*

#### Introduction

Wildfires are an important natural process which have widespread effects on human health, property, ecology, land cover, emissions, and more (Bowman *et al.*, 2009). While the fire activity over the last millennium can be modeled effectively using climatological variables until the Industrial Revolution, increased pressure from the growing human population around the 1900's altered global fire patterns via anthropogenic suppression and ignitions (Pechony and Shindell, 2010). This change is not limited to solely the number of fires and amount of burned area: recent studies have shown that fire size, and as a corollary, shape, are influenced by human activity as well (Hantson *et al.*, 2015; Hantson, Pueyo and Chuvieco, 2015).

From a remote sensing perspective, understanding and mapping the burned area has received more attention in the past than understanding the size and shape of individual fires. In fact, current methods used for identifying individual fires from coarse-resolution satellite data requires extracting those fires from existing burned area maps (Archibald and Roy, 2009; Archibald *et al.*, 2013; Hantson *et al.*, 2015; Hantson, Pueyo and Chuvieco, 2015; Oom *et al.*, 2016; Andela *et al.*, 2018). However, the shape and size of individual fires is an important topic with regard to ecology and fire succession, landscape management, and determining other fire

properties such as the spread rate. As a basic example, the length of the fire front impacts the ability of fauna to escape the flames (Whelan, 1995). The post-fire succession can be influenced by the shape of the burn as well as by the patchiness of the burned area mosaic which can favor certain plant or animal traits by changing the amount of fringe habitat and the openness of the canopy (Fuller, 1991; Whelan, 1995). Fire size is also related to management practices – heterogeneous landscapes create fuel breaks which can limit the spread of fire across the surface (Ager, Vaillant and Finney, 2010; Moreira *et al.*, 2011). Lastly, in image processing workflows such as those presented in (Frantz *et al.*, 2016; Nogueira *et al.*, 2017; Andela *et al.*, 2018), individual fires are identified for the purpose of extracting other metrics such as the fire spread rate, which are inherently linked to the shape and size of the fire.

Several programs exist with the goal of providing satellite products to be used for operationally monitoring – spatially and temporally – global wildfire activity. Such products can be broadly categorized as *active fire products* (representing locations actively burning on the Earth’s surface at the time of the sensor overpass) and *burned area products* (representing the post-fire affected area as determined by the removal of vegetation, exposure of soil and presence of charcoal and ashes). Two decades of mapping efforts have produced a number of global coarse spatial resolution (e.g. 250m to 1km pixel size) burned area products, including MCD45A1, MCD64A1, Copernicus Burnt Area, Fire CCI, and others (respectively, Roy *et al.*, 2005; Tansey *et al.*, 2008; Mouillot *et al.*, 2014; Alonso-Canas and Chuvieco, 2015; Giglio *et al.*, 2018). These products have used input from a variety of sensors including MODIS, SPOT-VEGETATION, PROBA-V, and MERIS. The extent and

timing of burning is an essential parameter in fire emissions calculations performed with the conventional bottom-up approach (Seiler and Crutzen, 1980), and the need for consistent estimates of greenhouse gas emissions was one of the main drivers of the development of global satellite fire monitoring products (Descloitres *et al.*, 2002).

Quality assessment of coarse-resolution burned area products is needed to provide data users with necessary information about the suitability of the products for specific applications, and has taken many forms such as intercomparison with other coarse-resolution burned area or active fire products (Boschetti *et al.*, 2004; Roy *et al.*, 2008; Boschetti *et al.*, 2010; Giglio *et al.*, 2010; Michael L. Humber *et al.*, 2019) or comparison with a sample of higher resolution, independently derived reference burned area maps (Boschetti *et al.*, 2019; Roy and Boschetti, 2009; Padilla, Stehman and Chuvieco, 2014; Padilla *et al.*, 2015). Product validation is an important activity outlined by the Committee on Earth Observation Satellites (CEOS) Land Product Validation (LPV) Subgroup and involves assessing product accuracy in one of four stages, each with increasing statistical rigor. The comparison with independent reference burned area maps (commonly termed *validation*) is conventionally conducted using accuracy metrics derived from a confusion matrix – i.e. the matrix reporting the co-occurrence of proportion of burned and unburned data in the product and in the independent reference data (for a review, see Boschetti, Stehman and Roy, 2016), or from the regression between proportions of area burned in coarser resolution grid cells (Gregoire *et al.*, 2006).

Arguably because of the great emphasis placed on the use of global burned area products for emissions estimation, validation has traditionally described the

accuracy and precision of *areal* estimates at different scales, rather than on the accuracy of other aspects of the burned area representation. The accuracy of the shapes mapped in a burned area product is currently not considered as part of product validation exercises, and neither is the accuracy of derived metrics such as fire size distribution, compactness, orientation or speed and orientation of the fire front. There is an outstanding need to expand the validation of burned area products to consider these characteristics. Several recent studies have aimed to quantify the distribution of fire sizes and other characteristics of individual fires, based on existing datasets that have not been validated beyond standard areal accuracy (Malamud, Millington and Perry, 2005; Hantson *et al.*, 2015; Hantson, Pueyo and Chuvieco, 2015; Andela *et al.*, 2018). Of those studies, only the results of (Hantson, Pueyo and Chuvieco, 2015) were partially validated, limited however to the comparison of the size distribution of MODIS-derived burn scars, to the size distribution of a sample of Landsat-derived burn scars, without directly comparing individual fires.

Evaluating properties such as the number of fires, fire size, and fire shape requires object-based approaches, rather than area-based approaches. While object-based accuracy assessments have been previously applied to remotely sensed thematic maps (e.g. Bruzzone and Persello, 2010; Clinton *et al.*, 2010; Baraldi, Humber and Boschetti, 2013; Yan and Roy, 2014), there has been relatively little research on the applications in burned area detection. Early work on object-based accuracy assessment of burned area classifications was conducted by (Rommel and Perera, 2002), who considered the degree of areal overlap between mapped and reference data between individual fire events using AVHRR-derived burned area

maps and a wide variety of high-resolution reference data (in addition to the confusion matrix). While this work was based on overlapping area and did not explicitly take into account the fire boundaries, it does highlight the errors from the perspective of the mapped burn, the individual fire event, and the reference data which provides an analog to the concepts of “producer’s” and “user’s” accuracy. Another recent exception is (Nogueira *et al.*, 2017), who proposed a patch-based burned area product accuracy assessment approach, but their method approximates it with an ellipsoidal model for the purposes of compatibility with the behavior of more advanced vegetation and fire models, such as ORCHIDEE (“Organising Carbon and Hydrology In Dynamic Ecosystems”) rather than assessing the actual mapped shape of the fire complex (Krinner *et al.*, 2005; Chuvieco *et al.*, 2016).

In this paper, we provide a novel edge error metric which is used to quantify the degree to which coarse-resolution burned area maps retain the shape of burn scars identified at medium resolution, in keeping with established protocols for burned area product validation. The metric is demonstrated through a comparison of the MODIS MCD64A1 Burned Area product, which has a nominal resolution of 500-m (Giglio *et al.*, 2018), to the Landsat-based Monitoring Trends in Burn Severity (MTBS) products, which have a resolution of 30 m (Eidenshink *et al.*, 2007). A calculation of the minimum achievable edge error metric, which accounts for differences in pixel size, is detailed in the Methods section along with other object-based metrics from literature. The results section presents the performance of the metrics and the paper concludes with a discussion of the implications of implementing coarse-resolution burned area products for representing individual fire shapes.

## Data

### MCD64A1 Burned Area Product

Coarse-resolution sensors such as MODIS provide global coverage with short revisit times (e.g. daily). This is advantageous for burned area mapping as the high temporal frequency improves the probability of obtaining cloud-free observations and can be exploited to more accurately determine the day of burning. On the other hand, such sensors are unable to capture fine details in the shape of objects on the ground due to their low spatial resolution and, in the case of burned area mapping, the minimum fire size which can be reliably mapped is larger than that obtainable by medium-resolution counterparts (Giglio, Randerson and van der Werf, 2013). In this paper, the latest Collection 6 MODIS MCD64A1 Burned Area product (Boschetti *et al.*, 2019; Giglio *et al.*, 2018) was selected because it is operational, global, and publicly available. The Collection 6 MCD64A1 product detects the most total burned area of any current operational product at coarse spatial resolution (Humber *et al.*, 2019), including significantly more burned area than the previous Collection 5.1 MCD45A1 product (Roy *et al.*, 2005, 2008), with yearly global burned area increasing by approximately 26% (Giglio *et al.*, 2018).

The MCD64A1 Burned Area mapping algorithm combines daily MODIS surface reflectance imagery with 1-km MODIS active fire data to map burning on a daily basis at the MODIS 500-m spatial resolution. The algorithm applies dynamic thresholds to composite MODIS Terra and Aqua imagery generated from a burn-sensitive spectral band index derived from MODIS 1240 nm and 2130 nm Terra and Aqua bands, and a measure of temporal variability. Cumulative MODIS 1-km active

fire detections are used to guide the selection of burned and unburned training samples and to guide the specification of prior burned and unburned probabilities (Giglio *et al.*, 2018).

The MCD64A1 Burned Area product includes several data layers – “Burn Date”, “Burn Date Uncertainty”, “QA” (Quality Assurance), and “First Day” / “Last Day” (during which burns can be reliably detected) (Giglio *et al.*, 2016). The product is distributed in the MODIS Sinusoidal Equal Area Projection (Wolfe, Roy and Vermote, 1998), with a nominal 500-m resolution (the actual resolution is 463.3127 m).

#### Monitoring Trends in Burn Severity (MTBS)

In previous literature, coarse-resolution ( $\geq 250$ -m) satellite-derived burned area maps have been assessed or validated using medium (typically  $\leq 30$  m) resolution data such as those provided by Landsat, e.g. (Boschetti *et al.*, 2019; Roy and Boschetti, 2009; Boschetti, Stehman and Roy, 2016; Padilla *et al.*, 2017; Giglio *et al.*, 2018). There are multiple programs in the United States which map burned area across the conterminous United States and Alaska using Landsat data. One of the more comprehensive efforts with regard to the total number of fires mapped is the Monitoring Trends in Burn Severity (MTBS) (Eidenshink *et al.*, 2007) project, which provides wall-to-wall Landsat-based burned area maps for the United States. The classification is largely derived from photointerpretation conducted by expert interpreters rather than automated methods.

MTBS commenced in 2005 in support of the Wildland Fire Leadership Council (mtbs.gov). Now supported by the USGS, U.S. Forest Service, and the U.S.

Department of the Interior, the program aims to map all fires since 1984 which exceed 1000 acres (405 ha) or 500 acres (202 ha) in the western and eastern United States, respectively. Three basic types of data are available from the MTBS program: burned area boundaries, fire occurrences, and burn severity mosaics. Both the burned area boundaries and burn severity mosaics provide information about the location and spatial extent of fires occurring in the United States and selected territories.

The burned area boundaries dataset consists of vectors which delineate the outermost extent of the burned area patches. The boundaries are derived via photointerpretation of Landsat TM, ETM+, and OLI scenes and do not identify internal unburned islands within the boundary of the burn (Eidenshink *et al.*, 2007). The burn boundaries are used to limit the extent of analysis for the burn severity data, which consists of classifications derived from the pixel values indicating the severity of burning based on the differenced normalized burn ratio (dNBR).

For studies in the United States, MTBS data have been used as a reference dataset for comparison to other products (Loboda *et al.*, 2011; Boschetti *et al.*, 2015). However, studies have demonstrated that MTBS often overestimates the total burned area due to the commission of the unburned islands to the burned area total (Sparks *et al.*, 2015). This feature is consistent with the intended use of MTBS, which focuses on land management rather than burned area estimates (Eidenshink *et al.*, 2007). It is noted that due to the ambiguity in the burn severity classification it is impossible to reconstruct internal unburned islands in the context of this study.

## Study Area

Eight fires in the western United States, occurring between 2005 and 2015, were selected as case studies (Fig. 3.1 and Table 3.1). The fires were selected in a semi-random fashion from the MTBS dataset, such that the fires represented a variety of sizes and locations. No more than one fire was selected for any given state.

According to the National Land Cover Database (NLCD2011) (Homer *et al.*, 2015), the dominant land cover for the Dry Creek Complex, Esmerelda Fire, Cave Creek Complex, and Murphy Complex was shrub/scrubland. The South Sarpy Fire and Lincoln Canyon Complex were also predominantly in shrub/scrublands, but also included grasslands/herbaceous areas. The East Amarillo Complex, the largest fire in the study, occurred predominantly in grasslands/herbaceous areas with secondary occurrence in shrub/scrublands. Finally, the Rim Fire occurred predominantly in evergreen forests with a secondary land cover of shrub/scrublands. In addition to these eight fires, 165 fires identified from the 2016 burning season were selected to demonstrate the methods over a large sample size.

*Table 3.1. Fires selected for this study, ordered by size (area reported by MTBS). Dominant Land Cover determined by the degree of overlap with the National Land Cover Database 2011 (NLCD).*

Fire Name	State	Year	Ignition Date	Size (ha)	Dominant Land Covers
South Sarpy Fire	Montana	2015	12-Jul-15	2,017	Shrub/Scrub and Grassland/Herbaceous
Lincoln Canyon Complex	New Mexico	2011	2-Aug-11	4,048	Shrub/Scrub and Grassland/Herbaceous
Dry Creek Complex	Washington	2009	20-Aug-09	20,170	Shrub/Scrub
Esmerelda Fire	Nevada	2005	15-Jul-05	40,920	Shrub/Scrub
Rim Fire	California	2013	17-Aug-13	104,040	Evergreen Forest and Shrub/Scrub
Cave Creek Complex	Arizona	2005	21-Jun-05	108,605	Shrub/Scrub
Murphy Complex	Idaho	2007	21-Jul-07	229,628	Shrub/Scrub
East Amarillo Complex	Texas	2006	12-Mar-06	240,139	Grassland/Herbaceous and Shrub/Scrub

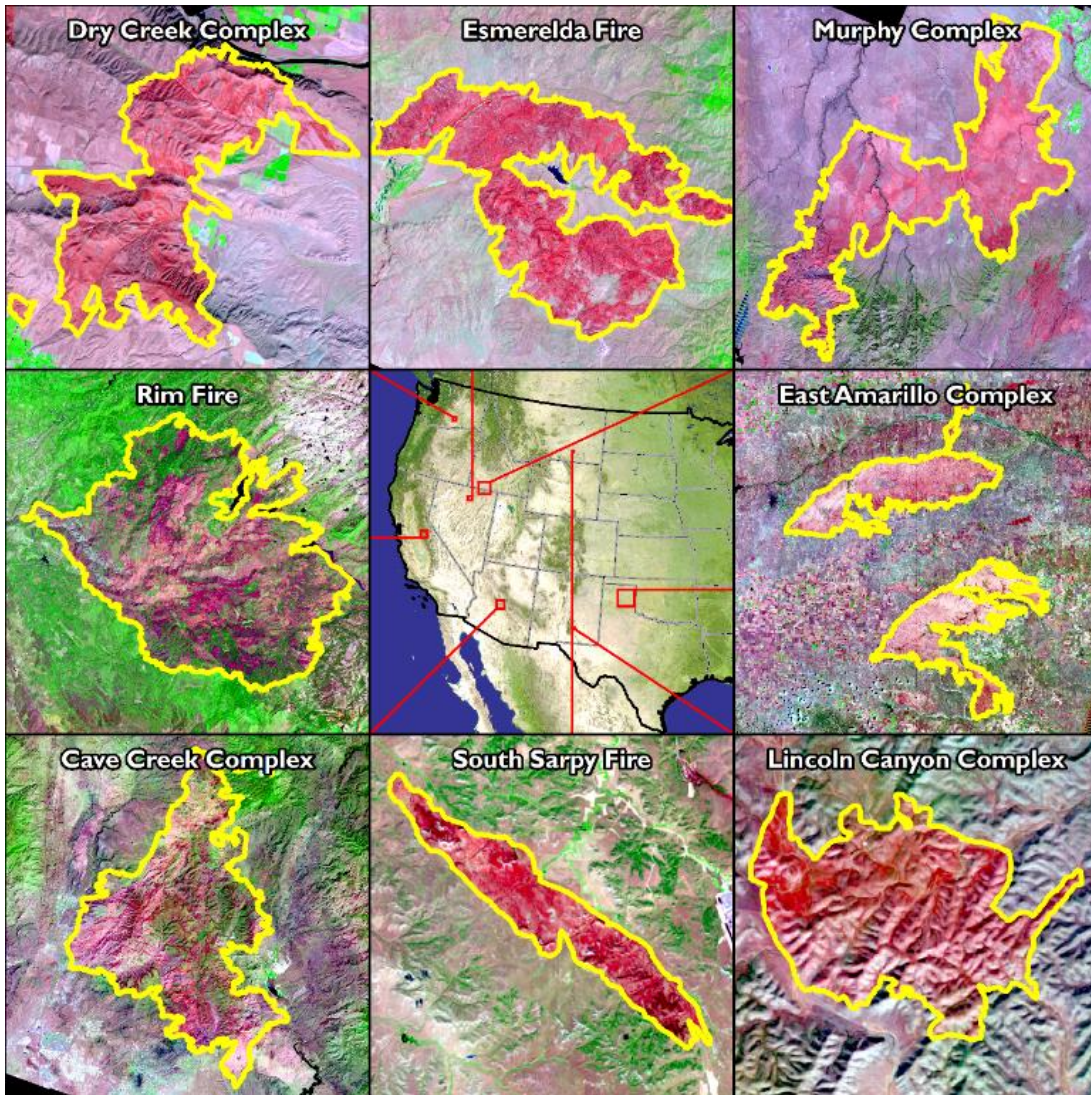


Figure 3.1. Eight fires selected for this study, depicted in RGB = SWIR2, NIR, Red composite with MTBS boundaries (yellow).

### Methods

Previous work has shown that the accuracy of pixel labels at the regional and continental scale does not necessarily indicate accuracy with respect to assigning shape boundaries (Baraldi, Humber and Boschetti, 2013). Object-based approaches to assessing burned area detection accuracy, wherein the entire shape of a fire are taken into consideration rather than simply the individual pixels, are necessary to quantify a classifier's performance at the individual fire scale and enable the accuracy of the fire

to be described with regard to shape as well as area. This approach, which should be considered complementary to – rather than a replacement for – the commonly implemented pixel-based approaches, consists of three key steps: extraction and harmonization, metric calculation, and identification of the minimum achievable edge error. These steps are described hereafter.

### Extraction and Harmonization

Individual fires were extracted from their respective datasets using a two-pass region (otherwise known as “connected components”) labeling algorithm, such as that described in (Shapiro and Stockmann, 2001). First, a binary mask was created from the MTBS and MCD64A1 datasets. The MCD64A1 product is distributed as a monthly composite; for this study, in instances where the burning event took place over the course of multiple calendar months, the monthly products were composited temporally such that the maximum day of burning between two consecutive months was retained. Unlike MTBS, the MCD64A1 product does not associate individual fires with a fire name. While several algorithms exist for the purpose of extracting individual fires from the MODIS Burned Area datasets (e.g. Archibald and Roy, 2009; Oom *et al.*, 2016), the operation was trivial and conducted manually for the relatively simple cases in this study. A binary mask was then created encompassing all cells flagged as burned.

From the binary masks, the locations of edge (that is, the boundary or perimeter) cells were extracted by identifying any cell adjacent to an unburned cell, based on queen’s case adjacency (otherwise known as 8-adjacency) rules. The location of the center of the cell was recorded, rather than the cell corners, and stored

in a vector format. The boundaries of the MTBS fires were projected from the native Albers Equal Area Projection to the MODIS Sinusoidal projection. For fires observed in 2016, MCD64A1-derived fires were then paired with MTBS fires under the following conditions: the overlapping area was greater than 10 percent of the MTBS and MODIS fire area; the area of the fire was greater than 500 ha; the fire was characterized as a “wildfire” by MTBS; and there was no obvious mischaracterization resulting from the rudimentary extraction method based on visual inspection.

### Metric Calculation

#### *Edge Error Computation*

Computer vision algorithms identify the similarity of two image objects through the lens of “shape representation” or “shape matching.” Generally, such algorithms may be used for database retrieval or image object retrieval (Günsel, Recognition and 1998, 1998; Andreou and Sgouros, 2005; Schindler and Suter, 2008; Nasreddine, Benzinou and Fablet, 2010). Shape matching algorithms are not typically spatially explicit and instead focus on identifying patterns regardless of size or orientation (Veltkamp, 2001; Adamek and O’Connor, 2004). These features may be useful for identifying broad patterns of shape, but, for object comparison in the spatially explicit geographic domain, these may not be desirable attributes as the rotation or orientation of a fire scar on the landscape is an intrinsic property of the fire itself. Any agreement in burned area shapes along different orientations is, in this regard, coincidental.

An advantage of shape matching in the scope of this study is the ability of the algorithms to assess the similarity of object boundaries without the use of a user-

defined parameter. The discrepancy in boundary locations, or so-called “contour dissimilarity”, is calculated by identifying the edges of an object (i.e. the burn edge extraction step) then calculating the distance between the edge locations of the evaluated object and a reference object. The error for each edge location is calculated by advancing through the edge points in order to identify the minimum distance between the objects (Adamek and O’Connor, 2004).

Measures of contour dissimilarity are desirable in this regard because, assuming the data are represented in a projected coordinate system, the unit of the contour dissimilarity in the geospatial domain is a physically meaningful representation of distance. In this work, the contour dissimilarity is calculated based on edge errors (*EE*), where the average edge error represents the expected distance between a given evaluated and target object. The proposed edge error metric quantifies the degree to which two burn identifications agree upon the location of a burn boundary. The method is used to determine the location of every edge pixel in an evaluated burn, *Burn(eval)*, relative to its nearest neighbors belonging to the target burn, *Burn(tgt)* (see Figure 3.2). It is assumed that if the boundaries are closer together on average, then the representation of the burn shape as a whole is more accurate.

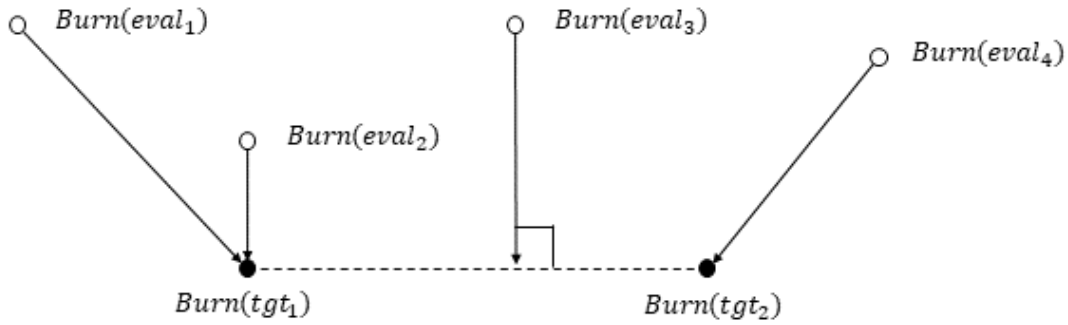


Figure 3.2. Association of four evaluated edge locations,  $Burn(eval_i)$ , to two target edge locations,  $Burn(tgt_j)$ . Note that evaluated edge locations 1 and 4 are associated with the nearest target burn edge location while evaluated edge location 3 is associated with the geometric normal of the line segment  $\overline{Burn(tgt_1), Burn(tgt_2)}$  and in the case of evaluated edge location 2, the geometric normal and nearest neighbor distance are identical.

In the ideal case, zero edge error represents instances where the burn boundaries of the evaluated product are perfectly aligned with the burn boundaries of the target product. In practice, this is very unlikely to be the case for an entire burn, especially at differing spatial resolutions, due to imperfect co-registration, sub-pixel differences in boundary identifications, and differences in methodologies for identifying burns in each data set. Note that while the first two issues are related to cell size and are not truly errors, the latter is a result of erroneous classifications. It follows that smaller edge errors (those approaching zero) therefore represent a higher level of agreement and a more accurate classification of the fire boundary while increasing edge errors indicate poorer characterization of the fire boundary.

The (coarse-resolution) MCD64A1 burn boundary is designated as the burn to be evaluated,  $Burn(eval)$ , which is compared to the higher resolution MTBS burn boundary designated as the target burn,  $Burn(tgt)$ . The  $EE$  is the mean error between an evaluated edge location  $Burn(eval)$  to the minimum of geometric normal of the line segment ( $\perp$ ) connecting the two nearest neighbors (NN) in a target burn,

Burn(*tgt*)<sub>NN1</sub> and Burn(*tgt*)<sub>NN2</sub>, or the closest of the two NN such that for a Burn(*eval*) with *n* edge locations (Figure 3.2):

$$EE = \sum_i^n \frac{EE_i}{n} \quad (1)$$

Where

$$EE_i = \min(EE_{NN}, EE_{Norm}) \quad (2)$$

and

$$EE_{NN} = d(\text{Burn}(eval_i), \text{Burn}(tgt)_{NN1}) \quad (3)$$

and

$$EE_{Norm} = d(\text{Burn}(eval_i) \perp [\text{Burn}(tgt)_{NN1}, \text{Burn}(tgt)_{NN2}]) \quad (4)$$

As detailed above, the value of *EE* (1) is the average of all *EE<sub>i</sub>* (see (2), (3), (4)) for a given burn identification. That is, all edge cell locations of the evaluated burn are iteratively compared to the nearest edge cell location(s) of the target burn. In the event that a Burn(*eval<sub>i</sub>*) has multiple Burn(*tgt*)<sub>NN2</sub> (when there is a tie for the second nearest neighbor), *EE<sub>Norm</sub>* is evaluated for all possible combinations of the tied elements, selecting the minimum of the evaluated outcomes. An example illustrating the *EE<sub>i</sub>* vectors for a hypothetical pair of burn shapes is provided in Figure 3.3.

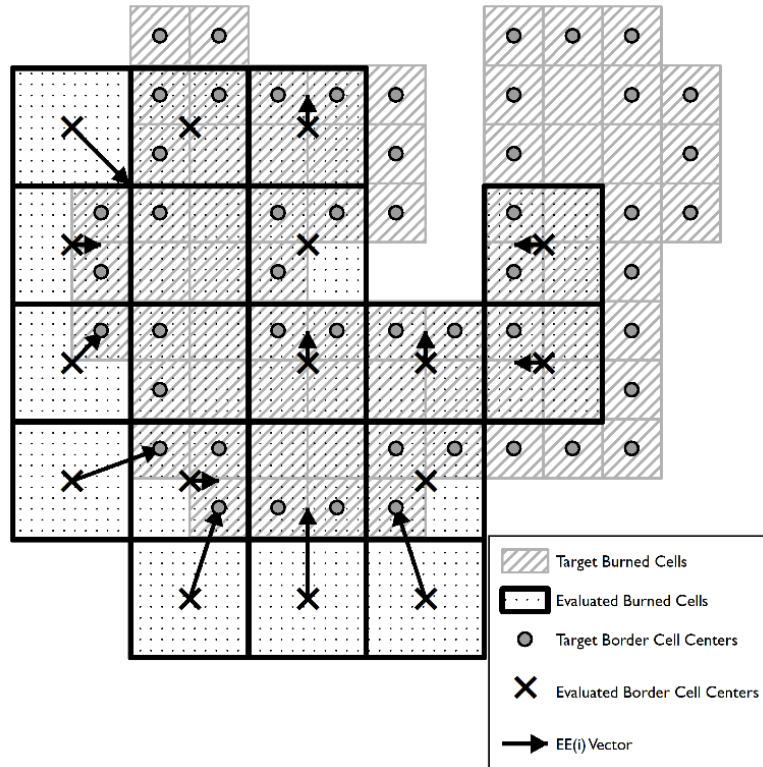


Figure 3.3. Edge error vectors for two hypothetical burns, in the direction of coarse to high-resolution. The “Target Burned Cells” represent the reference dataset at higher resolution, in this instance MTBS. The “Evaluated Burn Cells” represent the coarser resolution dataset, i.e. MCD64A1. The  $EE_i$  vectors (arrows) show the direction and magnitude of the cell-specific edge error.

It is noted that while a subset of the edge locations is often sampled in shape matching implementations, all edge locations are selected in this methodology in order to retain the spatial integrity of the input data. To accommodate the analysis of this volume of data, the search for nearest neighbors is made more efficient (with respect to time) through the use of K-Dimensional trees (“K-D trees”) (Bentley, 1975). K-D trees are a form of binary tree which can be used to rapidly reduce distance-based query time by dividing space using a hyperplane at each tree node. The time complexity for searching a K-D tree is approximated as  $O = n \log(n)$  where  $O$  is the maximum number of operations needed to identify the desired value and  $n$  represents the number of elements to be evaluated. For both the evaluated and

reference objects, a K-D tree is constructed containing all points identified in the edge location extraction step. Each point along the edge of the test object is used to query the reference K-D tree to find the two nearest neighbor points determined by the minimum Euclidean distance between the edge point and the point under evaluation in the K-D tree.

As the *EE* metric consists of the average distance between analogous points along the contours of two burned area identifications, the metric has physical significance and does not rely on any free parameter as input.

#### *Computation of Overlapping Area Metrics*

Many object-based metrics have been proposed in literature which relate the accuracy of a given evaluated object to a reference object based on area. Two of the more widely implemented indices, oversegmentation, and undersegmentation, can be considered analogous to errors of omission and errors of commission, respectively (Bruzzone and Persello, 2010; Clinton *et al.*, 2010; Baraldi, Humber and Boschetti, 2013; Yan and Roy, 2014). Oversegmentation (*OS*) describes the degree to which an algorithm divides an object into too many segments, i.e. omits areas which are within the boundaries of the true object, while undersegmentation (*US*) describes the degree to which an algorithm divides an object into too few segments, i.e. commits areas which are outside of the boundaries of the true object (Clinton *et al.*, 2010). Thus, *OS* (5) defines the relationship between the overlapping area, or intersection, of the target object (“*x*”) and the evaluated object (“*y*”) to the area of the target object such that:

$$OS = 1 - \frac{\text{area}(x \cap y)}{\text{area}(x)} \quad (5)$$

Similarly,  $US$  (6) defines the relationship between the overlapping area of the target object (“ $x$ ”) and the evaluated object (“ $y$ ”) to the area of the evaluated object such that:

$$US = 1 - \frac{\text{area}(x \cap y)}{\text{area}(y)} \quad (6)$$

Both metrics were calculated assuming the MTBS burned area as the target object and the MCD64A1 burned area as the evaluated object. It is noted that while MTBS is designated as the target object (by convention) in this case, the MTBS burned cell identifications themselves are un-validated and are expected to overestimate the total area burned due to the ambiguity of the “Unburned to Low Burn Severity” class. Hereafter,  $OS$  and  $US$  are also referred to as “overlapping area metrics” as they relate the area of one object to another.

#### *Identification of the Minimum Achievable Edge Error*

While the edge error is a measurement of the physical distance between comparable edge locations between two burned areas, the metric can only be interpreted directly when the burned areas are spatially co-registered and at the same spatial resolution. When the observations are presented at different spatial resolutions, it is necessary to account for the effects of the difference in spatial resolution in order to minimize the effects of random placement of burned cells in the higher resolution map compared to the lower resolution map.

In practice, many arrangements of burned pixels at high-resolution can be accurately represented by a coarse-resolution map such that the measured error is a consequence of the discrepancy in cell sizes. Figure 3.4 illustrates two cases where a coarser resolution pixel accurately and reasonably preserves the shape of an object

also represented at a higher resolution. In these cases, errors in the calculation of the edge error ( $EE$ ) are therefore the result of sub-pixel variations in the shape which are not expected to be captured by the coarse-resolution product, rather than errors in the classification itself. Noteworthy, however, is that Figure 3.4(a) will demonstrate an  $EE$  close 0 according to the method described earlier (because all edge cells at the higher resolution intersect the nearest neighbor or are located on the line segment connecting the two nearest neighbors, even though the areas are different!), while Figure 3.4(b) will exhibit a larger  $EE$ , though the value is less than the one-sided dimension of the coarse cell.

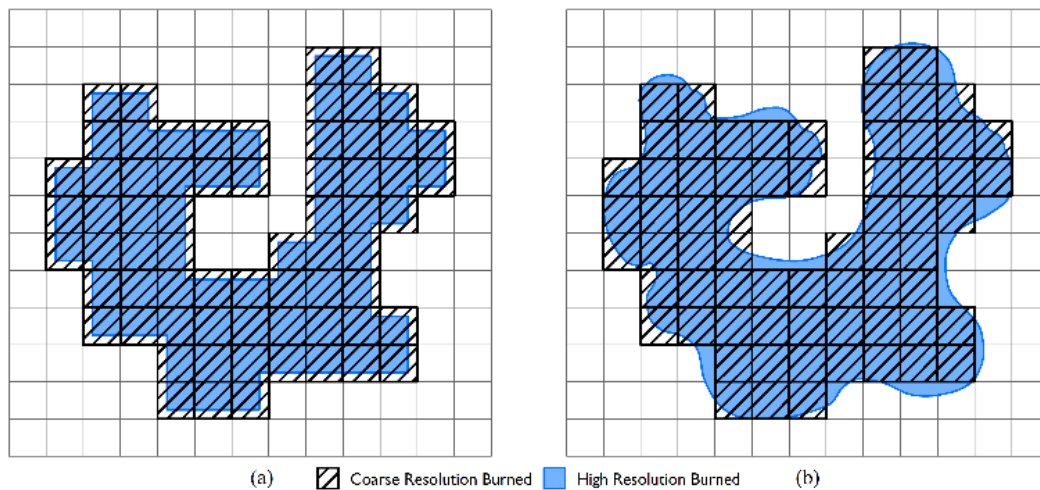


Figure 3.4. Examples of cross-resolution edge location scenarios. (a) illustrates burn boundaries at both resolutions are ideally co-located, while (b) illustrated a scenario in which contains commission and omission errors. The distance between edge locations in both cases is the result of only resolution differences.

Calculation of the Minimum Achievable Edge Error ( $MAEE$ ) gives context to the measurement by providing an estimate of the unavoidable error which results from differences in spatial resolution rather than algorithm misclassification. The  $MAEE$  calculation is a simplified version of the method implemented by (Boschetti, Flasse and Brivio, 2004) for calculating the Pareto Boundary. As with the cited work,

it is necessary to have only the higher resolution image – the MTBS burned area map – and to know the cell size of the coarser resolution product (463.3127 m in the case of MCD64A1).

For each of the eight fires in this study, the MTBS maps were projected and resampled to the MODIS Sinusoidal 500-m grid such that the values of the output raster are a soft classification representing the proportion of the coarse cell that was identified as burned in the original map (values range from 0% to 100%; Figure 3.5). Cells with values of 100% represent the core burned area while locations near the perimeter of the fire exhibit decreasing burn proportions. The soft classifications were then hardened for all whole percent thresholds in the range [1%, 100%], resulting in 100 possible classifications for each fire. The extraction procedure was repeated on the hardened burn proportion maps (Figure 3.6), upon which *EE* was calculated using the native resolution MTBS maps and the thresholded (MODIS resolution) MTBS proportion maps. Note that in cases where the cell sizes are the same and the datasets are spatially co-registered properly, the soft classification will contain only two unique values, 0% and 100%, where a threshold of 0% results in an (implausible) map where all cells are burned and a threshold of 100% results in the original burned area map itself.

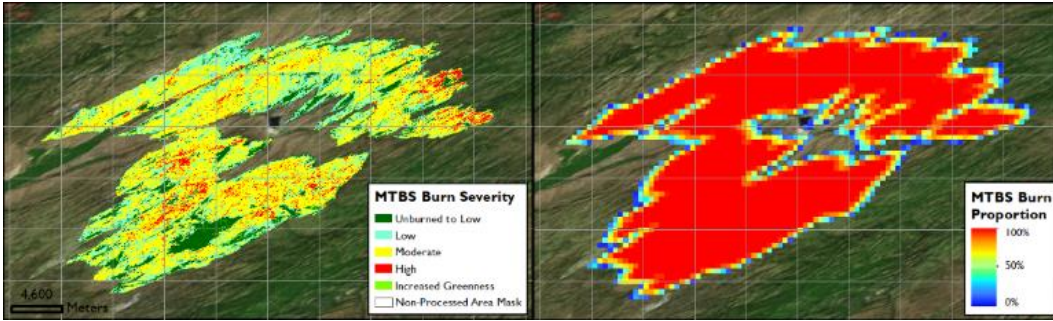


Figure 3.5. Esmerelda Fire: Original MTBS classification and projection/resampling to MODIS Sinusoidal 500-m grid indicating the percent of each cell identified as burned by MTBS.

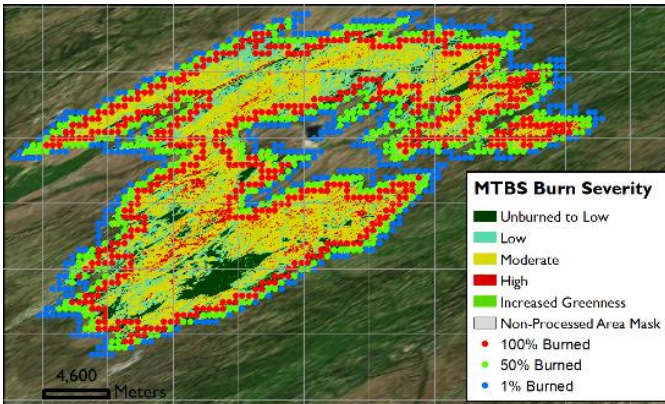


Figure 3.6. Esmerelda Fire: Edge cell locations for MTBS data at MODIS 500-m resolution using 1%, 50%, and 100% thresholds.

The minimum of each *EE* series per fire represents the optimal, or most efficient, solution and is retained as the *MAEE*. Recalling that this number represents the amount of expected or unavoidable error due to the random placement of burned cells at the higher resolution relative to the coarse-resolution, *MAEE* is reported along with *EE* in order to help distinguish between the errors resulting from incorrect classification from the errors resulting from differences in spatial resolution.

*MAEE* was calculated for only the eight case study fires. The reason for this is twofold: *MAEE* is unlikely to be relevant to users of the product when presented in aggregate, and as a practical matter the calculation of *MAEE* is computationally intensive.

## Results

The results of the methodology are presented in the following subsections. The *MAEE* calculation procedures are presented first, as these results are a component of the final edge error statistic. Then, the edge error metric results are presented, followed by the overlapping area metrics. Edge error and overlapping area metrics are presented in aggregate for the 2016 fire season.

### Minimum Achievable Edge Error

The *MAEE* calculation was performed for each of the eight case study fires, taking into consideration the error from the MTBS at the MODIS 500-m resolution to the MTBS native resolution edge. For each fire and threshold for subpixel fraction of area burned (1% to 100%) the mean edge error is plotted in Figure 3.7. Generally, the mean edge error distribution is concave, which is to say *EE* decreases monotonically as the threshold increases until the minimum is reached, at which point the mean edge error increases monotonically.

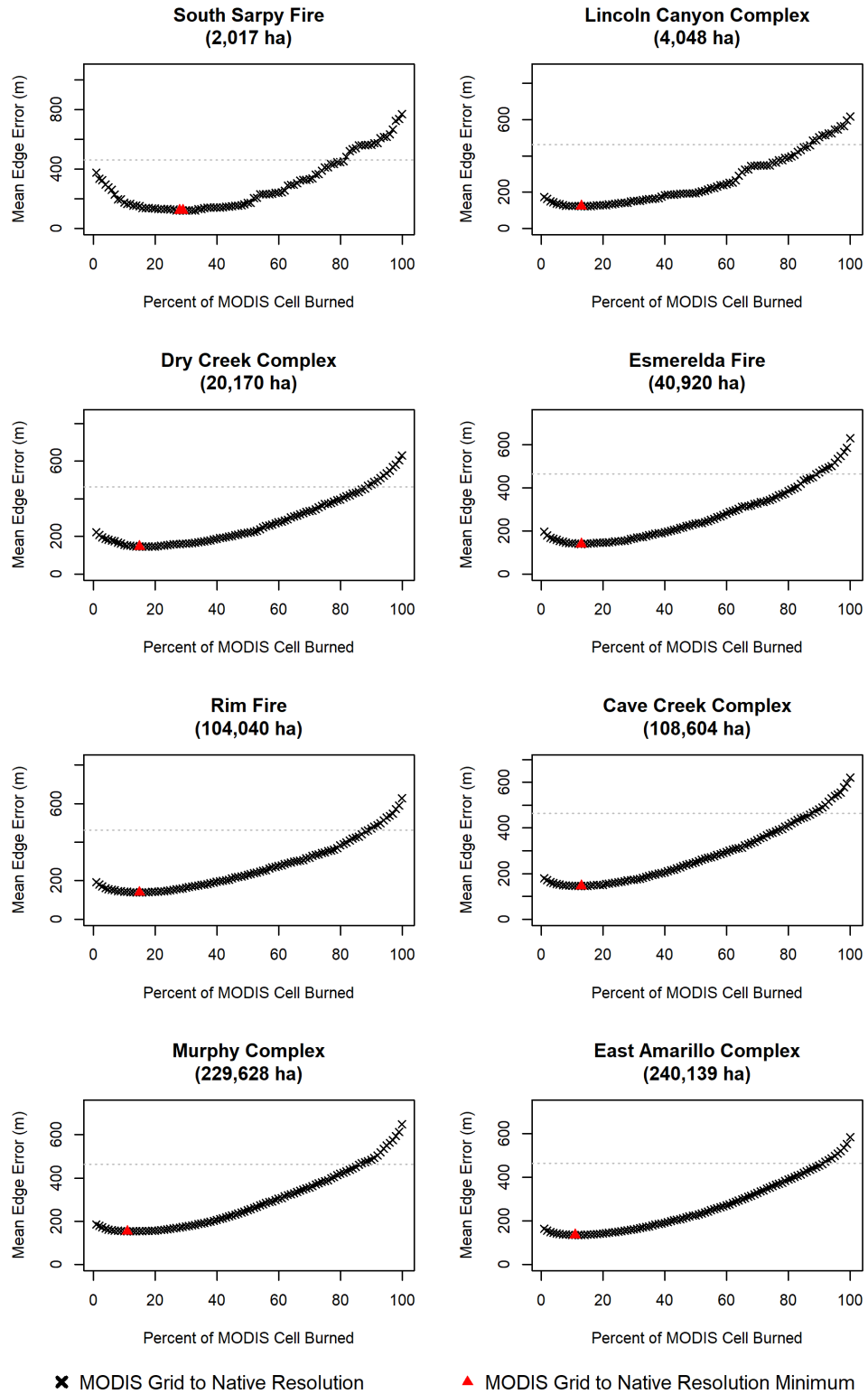


Figure 3.7. Minimum achievable edge error thresholds for MODIS resolution edge locations (463.3127 m cells) and MTBS native resolution edge locations. Red triangles indicate series minima; gray dashed lines indicate MODIS cell size.

The minimum mean achievable edge errors were observed using a minimum threshold in the range 11% (Murphy Complex and East Amarillo Complex) to 29% (South Sarpy Fire). The *MAEE* ranged between ~120.68 m (South Sarpy Fire) and ~153.35 m (Murphy Complex), thus in all cases, the minimum mean achievable edge error is less than 155 m, or roughly 33% of a MODIS 500-m cell. The range of *MAEE* values and thresholds for each fire underscores the need to calculate the metric on a per-fire basis, rather than assuming a single global value.

#### Edge Error and Overlapping Area Metrics

The edge error metric, *EE*, is presented for each of the eight case study fires, where MTBS at the native resolution was used in all cases (not to be confused with the aggregated classifications used for calculation of the *MAEE*). The results are presented in Figure 3.8 and Table 3.2, which show that the *EE* is less than or equal to the MODIS cell size (461.3127 m) in 5 out of 8 possible cases and is slightly greater than the MODIS cell size in one other case – the South Sarpy Fire (466.34 m). The Rim Fire produces arguably the worst result, with *EE* exceeding 776 m or roughly 1.7 cell-widths. For the 2016 fire season, the 25<sup>th</sup>, 50<sup>th</sup>, and 75<sup>th</sup> *EE* quantiles were 259.0 m, 332.9 m, and 442.7 m, respectively.

*Table 3.2. Object-based accuracy metrics for eight fires in the study region. The MAEE is presented parenthesis with the EE metric.*

Fire Name	Edge Error ( <i>EE</i> )		Overlapping Area Metrics	
	MCD64A1 to MTBS (m)	MTBS $\cap$ MCD64A1 (ha)	OS	US
South Sarpy Fire	466.34 (120.68)	<b>1175.73</b>	<b>0.43</b>	<b>0.07</b>
Lincoln Canyon Complex	339.62 (122.73)	3305.98	0.19	0.06
Dry Creek Complex	<b>317.95 (144.5)</b>	17578.31	0.14	0.05
Esmerelda Fire	355.06 (138.1)	35768.59	0.13	0.03
Rim Fire	<b>776.01 (138.72)</b>	88126.07	0.16	<b>0.01</b>
Cave Creek Complex	398.47 (145.22)	92582.20	<b>0.07</b>	0.05

Murphy Complex	769.23 (153.35)	201562.97	0.13	0.02
East Amarillo Complex	433.7 (134.49)	<b>211922.20</b>	0.12	0.05

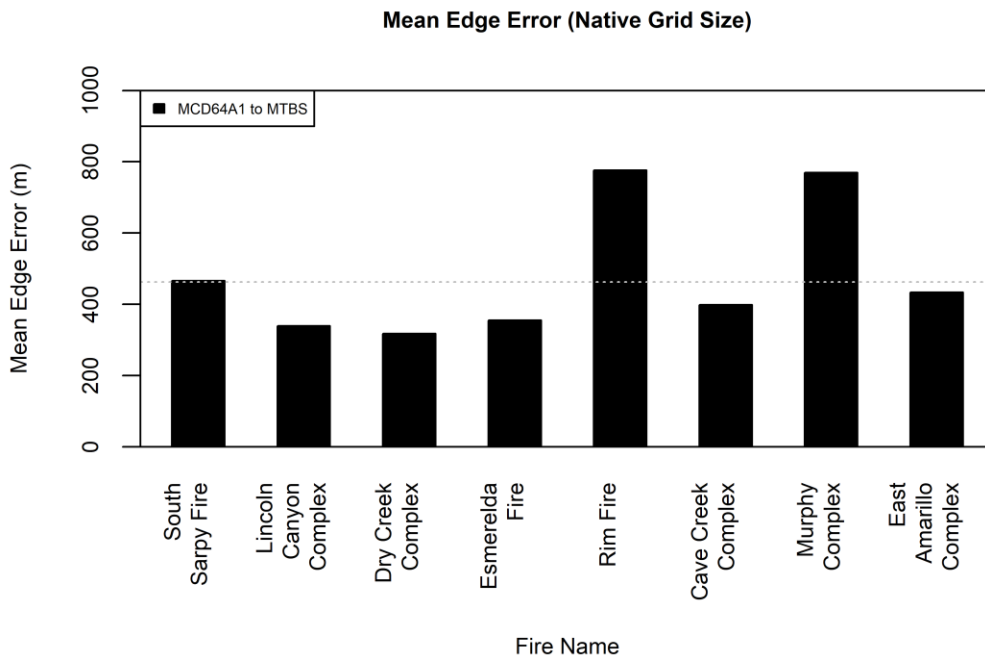


Figure 3.8. Mean edge error for MCD64A1 to MTBS. The dashed gray line indicates MODIS cell size.

The *EE* does not appear to be driven by fire size for the fires in this study, indicating that the MCD64A1 detections along the edge of a fire are relatively stable. The highest edge accuracy was achieved by the Dry Creek Complex, the third smallest fire in the study which burned 20,170 ha according to MTBS. The lowest edge accuracy was achieved by the Rim Fire, the fifth-largest fire in the study at 104,040 ha burned.

With regard to the Rim Fire, it appears that the burned area is poorly characterized by both the MCD64A1 and MTBS products. The former appears to omit some areas that were burned, while the latter commits a significant amount of

burned area due to the ambiguous “Unburned to Low” burn severity class. This is most evident in the northern portion of the fire, depicted in Figure 3.9.

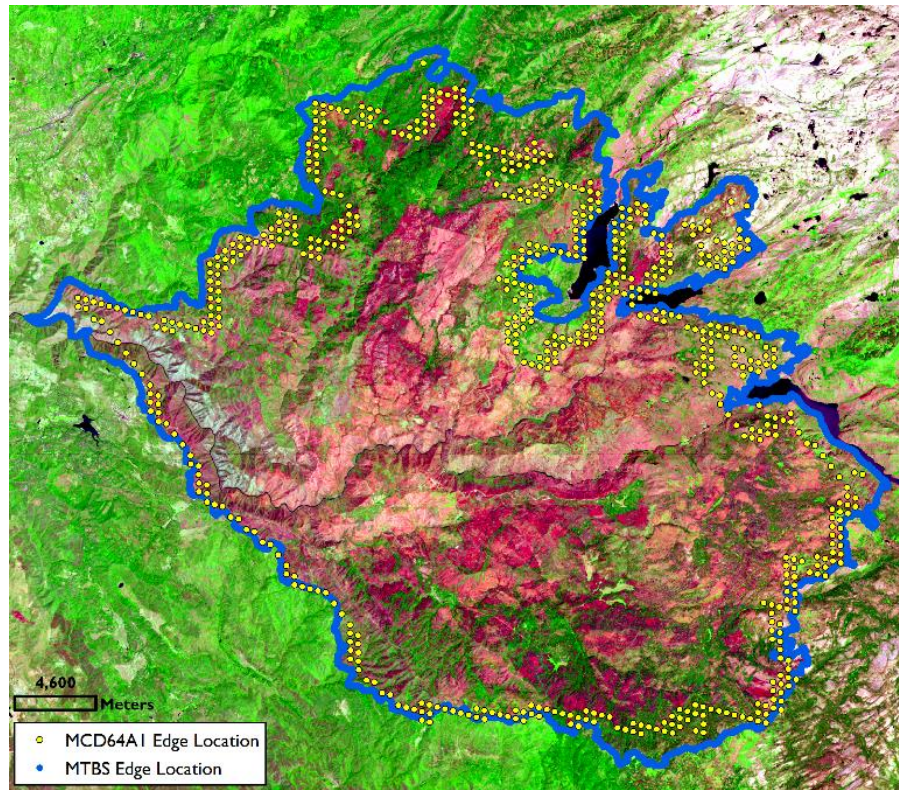


Figure 3.9. Rim Fire edge locations identified by MCD64A1 and MTBS. Significant discrepancies in the northernmost part of the image contribute to high EE values.

A comprehensive listing of the edge error indices for the case study fires is provided in Table II, along with the overlapping area metrics. For both the oversegmentation, *OS*, and undersegmentation, *US*, metrics, the smallest fire in the data set, South Sarpy Fire, demonstrated the worst performance. Intuitively, the area-based metrics are highly susceptible to large swings in the value of the metric for smaller sample sizes. On the other hand, two of the larger fires, the Cave Creek Complex and Rim Fire, demonstrated the smallest *OS* and *US* respectively. In the case of the Rim Fire, the *US* metric performed well at the expense of the *OS* metric for the reasons described above and illustrated in Figure 3.9. We note that these

results are in line with previous findings by (Rodrigues *et al.*, 2019), who determined that the levels of oversegmentation and undersegmentation (referred to as  $OE_{EDGE}$  and  $CE_{EDGE}$ , respectively) decrease as the average fire size increases for the Brazilian Cerrado. Regarding the 2016 fire season, the 25<sup>th</sup>, 50<sup>th</sup>, and 75<sup>th</sup> quantile *OS* errors were 0.15, 0.25, and 0.39, respectively, and the *US* errors were 0.04, 0.07, and 0.13, respectively.

### Discussion and Conclusion

Burned area accuracy assessment has historically been limited to the traditional pixel-based confusion matrix approaches, which succinctly summarize the probability of a pixel having a correct burned or unburned label. These approaches are effective for studies related to the total area burned at coarse spatial scales where the actual shape of fires may be either obscured due to pixel size or of little consequence to the intended use of the data.

This paper introduces a method for characterizing the accuracy of the shape of coarse-resolution burned area detections, by comparing them to higher resolution reference burned area maps. A novel edge error metric (*EE*) indicates the average distance between the boundary of individual burned areas as mapped in the coarse-resolution product and the reference boundary. This metric is accompanied by an indication of the minimum achievable edge error which accounts for burning in the high-resolution reference map which is smaller than the resolution of the coarse product.

To benchmark the performance of the proposed metric, two conventional indices from the object-based image analysis literature were calculated –

oversegmentation and undersegmentation. The oversegmentation (*OS*) and undersegmentation (*US*) metrics show a general tendency to demonstrate large errors for small fires (consistent with Rodrigues *et al.*, 2019) while the edge error does not appear to be related to fire size. This is intuitive given the formulation of the metrics - *OS* and *US* are indices based on the errors in *two-dimensional area*, while *EE* is a measure of the errors in *zero-dimensional (point) edge locations*. At the individual fire level, the proposed *EE* metric complements, but should not replace, the area-based indices because the quantities which they evaluate are different.

The approach was demonstrated by assessing the shape accuracy of the MODIS Collection 6 MCD64A1 Burned Area, using as reference data a sample of high-resolution fire perimeters provided by the Monitoring Trends in Burn Severity (MTBS) project. Our results indicate that for the sample of eight individual fires considered in the analysis, the MODIS Collection 6 MCD64A1 Burned Area product is able to capture the boundaries of fires identified at the Landsat-scale by MTBS. In most cases, the edge error was less than the width of one MODIS 500-m cell and in all cases, the error was less than the width of two cells. Considering the sample of 165 fires that occurred in 2016, the average *EE* for the selected fires was approximately 332 m and the *EE* was less than two pixels in 160 out of 165 cases (97%). No anomalous/unanticipated algorithm behavior was observed when calculating the *EE* of the larger dataset, indicating that our proposed method is operationally stable (a primary rationale for assessing the larger test sample).

It is important to note that the primary purpose of the MTBS dataset is to provide information for land managers on burn severity, and it is not designed to be a

reference dataset for satellite-based burned area mapping [41], as the dataset is often employed. As a result, and due to the labor-intensive procedure used to generate the MTBS dataset, the extent of unburned islands within a fire is not mapped. However, it is expected that the identification of unburned islands within fires changes significantly with scale, e.g. many small unburned islands may exist at the 30 m scale which does not manifest as a meaningful signal at coarse-resolutions. This highlights implicit assumptions of the *EE* metric that: (i) any boundary – burned or unburned – is large enough to be captured by both the test and reference datasets and (ii) for any boundary in a given dataset, a corresponding boundary exists in the other. In the absence of these conditions, the edge errors increase as a function of the number, size, and placement of the unmatched boundaries within the fire extent. The unburned islands are discussed in the Appendix, with the *EE* metric applied to photointerpreted data to demonstrate the metric conceptually, assuming the aforementioned issues have been resolved.

Due to the cross-resolution calculation of the minimum achievable edge error metric, this approach can theoretically be applied to any other combination of burned area maps and reference data, including maps and reference data of the same spatial resolution. Additionally, given a method for automated extraction of individual fires from burned area maps (e.g. Andela *et al.*, 2018), the method can conceivably be routinely applied to the global validation of coarse-resolution products, e.g. (Boschetti *et al.*, 2019; Padilla, Stehman and Chuvieco, 2014). The edge error metric is able to capture information lost in pixel-based accuracy assessment and, for studies

focused on shape and topology of burned area perimeters, it is a more representative and relevant source of information regarding mapping accuracy.

In future work, we will apply the edge error metric as well as the other object-based indices in two research areas. First, we plan to analyze the difference in edge errors for fires identified by different classification algorithms to compare, for example, the MODIS MCD64A1 Collection 6 500-m burned area product (Giglio *et al.*, 2018) and the Fire CCI version 5.1 250-m burned area product which is also derived from MODIS (Chuvieco *et al.*, 2018), or the Fire CCI version 4.1 300-m burned area product derived from MERIS (Alonso-Canas and Chuvieco, 2015).

Additionally, given a higher spatial resolution dataset delineating true fire boundaries, the edge error metric can be used to refine burn scar extraction algorithms. Typically, individual burn scars are identified using flood fill algorithms which use a threshold for the maximum number of days between detections in neighboring pixels to determine adjacency (e.g. Archibald and Roy, 2009; Archibald *et al.*, 2013; Hantson *et al.*, 2015; Hantson, Pueyo and Chuvieco, 2015; Andela *et al.*, 2018; Laurent *et al.*, 2018), which can lead to under- or over-segmentation if the threshold is too large or small, respectively. Edge error, in these cases, could be evaluated iteratively with different thresholds to empirically derive a more representative regional threshold.

### Appendix

An implicit assumption in calculating the *EE* metric is that each object identified at the coarser resolution has a corresponding object at the finer resolution (this assumption is already made when selecting the fires for analysis in the first

place). The *EE* can, therefore, be calculated including unburned islands within the outer boundary of the burn with no modification, provided this condition is met.

However, special consideration must be given to unburned islands as several studies have demonstrated that the presence of unburned islands observed by satellites do not correspond well to *in situ* measurements taken at a higher spatial resolution (Price, Russell-Smith and Edwards, 2003; Russell-Smith *et al.*, 2009). Similarly, unburned islands identified at a higher resolution will not necessarily correspond to those identified at a coarser resolution, e.g. Landsat vs. MODIS, meaning that it is not guaranteed that all unburned islands will be present in both datasets. This issue can, in theory, be solved by applying a robust set of rules for selecting unburned islands that are present across different resolutions, i.e. accounting for the low-resolution bias (Boschetti, Flasse and Brivio, 2004). These rules could be based on the size of the unburned island, whether or not the unburned islands overlap in both datasets, etc. Determining these specific rules is outside of the scope of this work, but it is of interest to the broader fire remote sensing community and deserves additional study.

Two of the case studies were chosen to conceptually demonstrate the *EE* metric when applied to burn scars containing unburned islands. These fires, the Esmerelda Fire and the East Amarillo Complex, were manually photointerpreted to append the larger internal unburned islands to the MTBS boundaries (Figure 3.10s). The edge of the internal unburned islands and external fire boundaries were then compared between the modified MTBS and MCD64A1 fire shapes. The *EE* for the Esmerelda Fire was 252.59 m and the East Amarillo Complex was 398.52 m,

representing improvements of more than 100 m and 40 m, respectively, when compared to the *EE* of the fire boundary alone. This improvement can be attributed to the fact that the geometry of the unburned islands for the two burns is less complex (often elliptical in shape) than the fire boundary geometry. A caveat to this demonstration is that the photointerpretation of the unburned islands purposefully left out very small unburned islands – as previously mentioned, conducting this analysis at scale requires a robust method for determining the minimum detectable unburned island size.

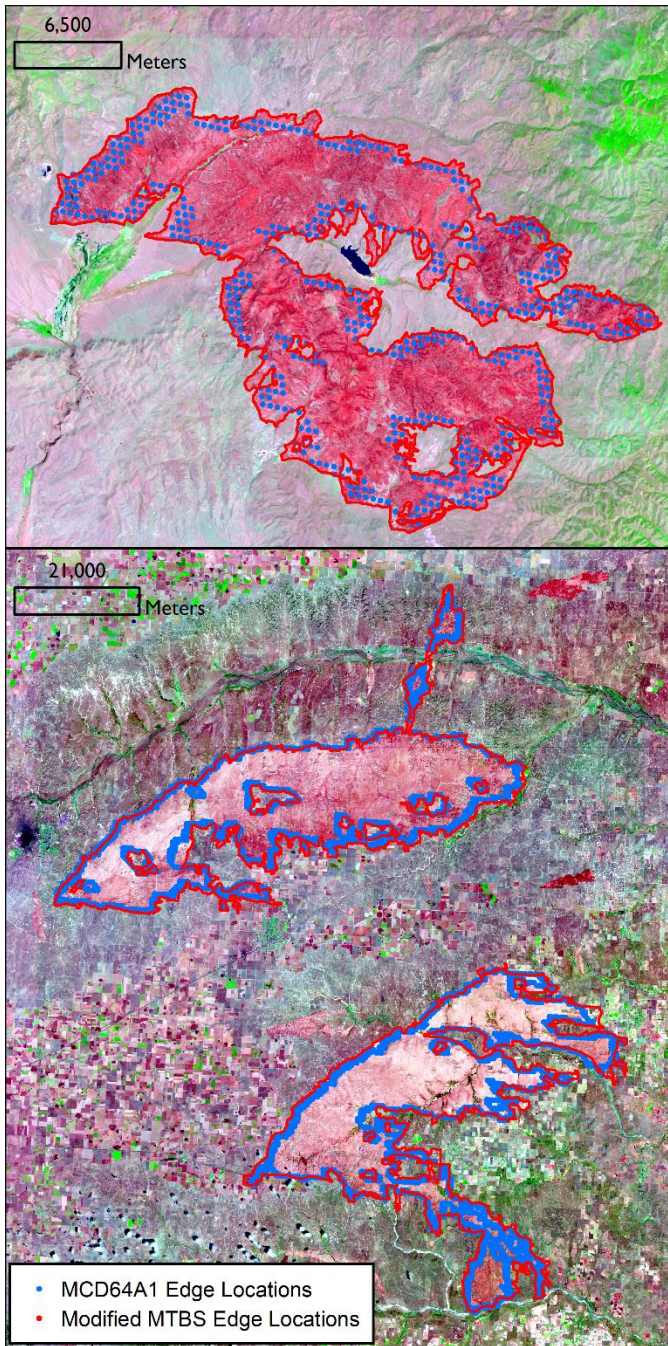


Figure 3.10. MCD64A1 and Modified MTBS edge locations including interior unburned islands. Top: Esmerelda Fire (Nevada, 2005) has an EE of 252.59. Bottom: East Amarillo Complex (Texas, 2006) has an EE of 398.52.

### Acknowledgments

This work was supported by NASA grants 80NSSC18K0739, 80NSSC18K0890, and 80NSSC18K0400.

## Chapter 4 – A MODIS MCD64A1-based Algorithm for Identifying Individual Fires in Boreal and Arctic North America

### Introduction

Remote sensing of wildfires provides unique opportunities to analyze large-scale fire patterns taking advantage of consistent, systematic, and frequent observations. Past studies have used global coarse resolution burned area datasets to describe the fire size distribution over large areas based on satellite observations (Archibald and Roy, 2009; Archibald *et al.*, 2013; Hantson *et al.*, 2015; Hantson, Pueyo and Chuvieco, 2015; Oom *et al.*, 2016), with recent work providing publicly available datasets containing individual fire characteristics (Laurent *et al.*, 2018; Andela *et al.*, 2019). Because the burned area products from which individual fires are derived have been generated automatically, their biases can generally be considered systematic and consistent, in comparison to photointerpretation-based methods which, while capable of providing higher accuracy, can vary widely depending on the photointerpreter.

Fire regimes have typically been summarized in terms of area burned, timing of burning, and length of fire season, often neglecting the size distribution of individual fires, as size measurements have been hard to obtain over large areas. Small fires, which contribute very little to total burned area even though much more plentiful than large fires (Malamud, Millington and Perry, 2005; Hantson *et al.*, 2015; Hantson, Pueyo and Chuvieco, 2015), are often excluded from databases of manually

derived fire boundaries due to the inherent mapping difficulties (AICC, no date; Natural Resources Canada, no date; Eidenshink *et al.*, 2007).

At broad scales, large fires are correlated with high fire intensity (Archibald *et al.*, 2013). At the same time, it has been shown that higher fire radiative power (FRP) drives convection in the atmosphere leading to higher injection heights (Amiridis *et al.*, 2010) and that boreal forests have the highest injection heights globally (van Martin, Logan and Kahn, 2010). Black carbon and other light-absorbing particles can be transported to the Arctic regions from Boreal fires, depending on the FRP and the time of year (Stohl *et al.*, 2006; Hall and Loboda, 2017), leading to decreased surface albedo and subsequent loss of snow cover and land/sea ice, triggering a positive feedback loop. This cycle has been speculated since the mid-2000's (Hansen and Nazarenko, 2004) and attributed to boreal wildfires shortly thereafter (Kim *et al.*, 2005). Other work also suggests that increased albedo following wildfires leads to a net cooling effect regardless of black carbon deposition (Randerson *et al.*, 2006; Chen *et al.*, 2018).

The Global Fire Emissions Database (Giglio *et al.*, 2006; van der Werf *et al.*, 2006) attributed approximately 2.5 Mha of burned area per year between 2002 and 2016, or ~0.5% of global burned area (Giglio *et al.*, 2018) to Boreal North America, a region defined to include Canada and Alaska. Fires in the region disproportionately contributed an estimated average of 5 Tg C per year, or ~2.7 percent of global fire emissions, due to high fuel consumption rates and consumption of organic soils (van der Werf *et al.*, 2017).

Within the North American boreal forest biome, wildfires are characterized by long burning duration, high intensity, and large size (Kasischke *et al.*, 2010; French *et al.*, 2015), while fires in the tundra tend to be less frequent and smaller than in the boreal system (French *et al.*, 2015). Burned area totals are dominated by a small number of large fires, particularly in boreal forests where fires < 200ha contribute < 3.5% of burned area in Canada (Stocks *et al.*, 2002) and < 1% in Alaska (Kasischke and Turetsky, 2006). In Canadian and Alaskan boreal forests, large fires not only drive the total amount of burned area but also correspond to higher fire intensity, increased burn severity and increased soil burning depth leading to higher rates of carbon loss (Turetsky *et al.*, 2011). Fire size and shape influence fire succession (Fuller, 1991; Whelan, 1995; Turner *et al.*, 1998), soil erosion (Gill and Allan, 2009), and landscape composition and fragmentation (Barrett *et al.*, 2011; Lehsten, de Groot and Sallaba, 2016).

Recent studies generally agree that climate change will significantly impact wildfire patterns in the northern regions, with higher temperatures expected to result in increased fuel drying during the burning season, in turn leading to more intense fires with greater fuel consumption (in terms of area burned and combustion completeness) occurring at a higher frequency (Balshi *et al.*, 2009; Flannigan *et al.*, 2009; de Groot, Flannigan and Cantin, 2013; French *et al.*, 2015). Through observation of past climate patterns, relevant work has shown that large scale patterns in temperature and moisture availability can be predictive of the total burned area (Duffy *et al.*, 2005; Balshi *et al.*, 2009). Under these scenarios, fire size is likely to increase corresponding to the probability of encountering fire weather conditions

during the fire season (Abatzoglou and Kolden, 2011; Barrett *et al.*, 2016). A rigorous and consistent method to map individual fires over large areas is therefore needed to monitor changes in fire size distribution.

In this work, we present a method for extracting individual fires from the Collection 6 MODIS MCD64A1 Burned Area product (Giglio *et al.*, 2018) in Alaska and Canada from March 2002 through February 2019, subdivided into three main regions (Figure 4.1) derived from the Terrestrial Ecoregions of the World map (Olson *et al.*, 2001): boreal (~508 Mha), tundra (~374 Mha), and other (temperate biomes; ~218 Mha). We then use object-based approaches to assess the accuracy of the shape of individual fires compared to the existing Fire Atlas database (Andela *et al.*, 2019), implementing existing high-resolution databases of individual fire boundaries as reference data (AICC, no date; Natural Resources Canada, no date; Loboda and Hall, 2017). The results are then used to analyze patterns of fires larger than 200 ha in Canada and Alaska, as identified by the Collection 6 MCD64A1 Burned Area product.



Figure 4.1. Biomes within the Alaska and Canada study area.

## Data and Methods

### Individual Fire Extraction

Systematic analysis of large area, multi-annual patterns of fire sizes is typically based on satellite observations of burned areas. To exploit the consistent, systematic data which can be obtained only through satellite observations, all available data from the MODIS Collection 6 (C6) MCD64A1 Burned Area product archive (Giglio *et al.*, 2018) for March 2002 through February 2019 were used in this study (Figure 4.2). This product identifies the most total burned area of any current global operational coarse resolution product (Humber *et al.*, 2019; Chuvieco *et al.*, 2019), although, in Canada and Alaska, the C6 MCD64A1 product identifies approximately 6 percent less burned area than its Collection 5.1 predecessor (Giglio *et al.*, 2018). A recent validation exercise, in line with the Committee on Earth

Observation Satellites (CEOS) Calibration/Validation Stage 3 guidelines (*CEOS Land Product Validation Subgroup*, no date), showed that out of seven biome types, the C6 product arguably performs best in the boreal forest biome, with omission errors and relative bias far lower than any other biome and the third lowest commission error of any biome (Boschetti *et al.*, 2019).

Several approaches have been implemented for extracting individual burns from coarse spatial resolution burned area maps. Several of these approaches are based on a flood-fill algorithm (Archibald and Roy, 2009) developed for the Collection 5 MODIS MCD45A1 burned area algorithm (Roy *et al.*, 2005). The approach evaluates adjacent pixels labeled as burned and considers those pixels to be from the same event if the day of burning identified for each pixel is less than 8 days apart, where 8 days was chosen as the adjacency threshold because it represented the temporal accuracy of the MCD45A1 product. Several other works have implemented a similar flood-fill algorithm, but have tuned the adjacency threshold empirically or heuristically. For example, the Fire Atlas algorithm (Andela *et al.*, 2019) implements an adaptive threshold based on fire frequency in a given area. Other works rely on empirically derived thresholds, ranging from 2 days (Archibald *et al.*, 2013) to 14 days (Hantson *et al.*, 2015) with other intermediate thresholds implemented as well (Hantson, Pueyo and Chuvieco, 2015; Oom *et al.*, 2016).

While the location and day of burning (*DoB*) are reported by most global burned area products (Roy *et al.*, 2005; Tansey *et al.*, 2008; Alonso-Canas and Chuvieco, 2015; Chuvieco *et al.*, 2018; Giglio *et al.*, 2018), MCD64A1 is unique in that the product provides a per-pixel estimate of the *temporal* uncertainty of the burn

detection. The burn date uncertainty represents the period of ambiguity in the spectral separability index used to identify burns during which there is insufficient data to label a cell as burned or unburned due to aerosol loading, cloud cover, etc. (Giglio *et al.*, 2009, 2018). By default, the burn date uncertainty of the MCD64A1 product is set to 1 day to compensate for errors resulting from the overpass time of the sensor, i.e. the cell burned the day before the burn was detected but after the previous satellite overpass. In cases where the cell is obscured for one or more days by aerosols or clouds, the uncertainty represents the number of days between clear observations because, in reality, the actual day of burning could have occurred on any day within the uncertainty window.

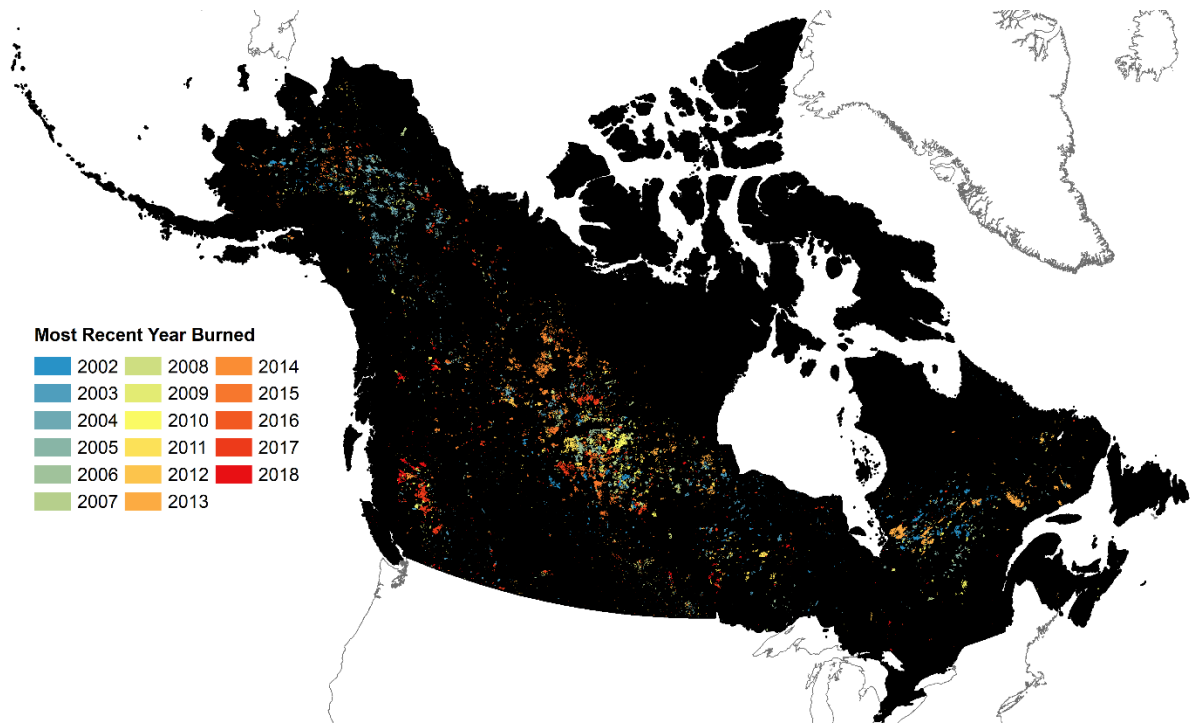


Figure 4.2. MODIS MCD64A1 burned area detections in Canada and Alaska. Year refers to fire year, from March to the following February.

Using this additional source of information, the MODIS Uncertainty-based Single-fire Extraction (MUSE) algorithm was developed and designed to identify

individual burns by analyzing the *DoB* of each mapped cell while considering its temporal uncertainty. Like other flood-fill algorithms, the MUSE algorithm searches for adjacent cells which are both labeled as burned with the differenced day of burning falling below a defined threshold. However, rather than applying a static or empirically defined threshold, burned cells are only considered to be connected (8-connectivity / Queen's case adjacent) if their *possible* burn dates overlap, as determined by the *DoB* and the *burn date uncertainty*. The range of possible dates during which the burn could have occurred is established by assuming the identified *DoB* as the median day of the range,  $\pm$  half of the burn date uncertainty. Additionally, to account for the sub-cell fire spread, an additional day is allotted for the fire to spread across the ground surface.

This approach was applied to spatiotemporal mosaics of the C6 MCD64A1 Burned Area product. The mosaics were created for each fire year for all of Alaska and Canada, with the fire year defined as the period between March 1 of a given year and the following February 28/29. Past work has shown that fire activity is at a minimum both globally and for Canada and Alaska in March (Boschetti and Roy, 2008; Giglio, Randerson and van der Werf, 2013), therefore “resetting” the fire year during March greatly reduces, or ideally eliminates, errors resulting from cells which burn twice in the same calendar year. In practice, fire activity in Canada and Alaska is very low between October and April – the selection of March is purely academic in this regard.

Isolated pixels and very small groups of cells (five or fewer) were removed from the dataset – these clusters of cells fall below the minimum fire size which is

confidently mapped by the MCD64A1 algorithm of approximately 120 hectares (Giglio *et al.*, 2009). Other works such as (Hantson *et al.*, 2015; Hantson, Pueyo and Chuvieco, 2015) also remove these small clusters of cells, while the Fire Atlas (Andela *et al.*, 2019) allows for exceptions to the fire growth tracking algorithm in cases where the small groups of cells are adjacent to much larger burns. The effects of the small cluster removal are minimal in the context of this work, as the downstream analysis is limited to only fires larger than 200 ha (> 9 MODIS 500-m cells) by the availability of validation data.

A relevant error existed in the processing of the C6 MCD64A1 product which prevented the first or last column of twenty-six tiles from receiving a “burned” label due to an overly restrictive contextual relabeling test. This error was corrected for August 2018 onward, however, months prior to August 2018 will be corrected in the forthcoming MODIS Collection 7. It is expected that fires crossing the boundaries of the affected tiles will be artificially segmented in this work, with two tiles affected in the study region (h11v02 and h09v04). This issue can lead to artificial splitting of burns into multiple segments if the burn lies along the edge of one of these tiles.

#### Accuracy Metrics

While the C6 MCD64A1 product has been extensively validated at the pixel level (Boschetti *et al.*, 2019; Chuvieco *et al.*, 2018; Giglio *et al.*, 2018), these exercises focused on characterizing the amount of burning over large areas and do not address the accuracy of individual burn scars. To characterize the per-fire performance of the algorithm, object-based approaches are necessary. Object-based accuracy assessments have been previously applied to remotely sensed thematic maps

(Clinton *et al.*, 2010; Persello and Bruzzone, 2010; Baraldi, Humber and Boschetti, 2013; Yan and Roy, 2014), but only a few have addressed burned area maps specifically (Humber, Boschetti and Giglio, Accepted; Rimmel and Perera, 2002; Nogueira *et al.*, 2017).

The accuracy metrics chosen for this work relate a coarse resolution mapped object to a higher resolution reference object. To summarize the degree of areal overlap between the two objects, the commonly used oversegmentation (*OS*) and undersegmentation (*US*) indices were selected (Clinton *et al.*, 2010; Persello and Bruzzone, 2010; Baraldi, Humber and Boschetti, 2013; Yan and Roy, 2014; Humber, Boschetti and Giglio, Accepted). *OS* and *US* indicate the degree to which a reference object is divided into too many or too few parts, respectively. In this regard, the *OS* is related to errors of omission while *US* is related to errors of commission when considering the evaluated objects as a binary burned/not-burned classification.

Thus, *OS* defines the relationship between the overlapping area of the reference burn scar (“*x*”) and the classified burn scar (“*y*”) to the area of the reference burn scar such that:

$$OS = 1 - \frac{\text{area}(x \cap y)}{\text{area}(x)}$$

Similarly, *US* defines the relationship between the overlapping area of the reference burn scar (“*x*”) and the classified burn scar (“*y*”) to the area of the mapped burn scar such that:

$$US = 1 - \frac{\text{area}(x \cap y)}{\text{area}(y)}$$

The overlapping area metrics *OS* and *US* are calculated only for the mapped fire which most overlaps a given reference fire.

Complementary to the overlapping area indices, the edge error ( $EE$ ) metric (Humber, Boschetti and Giglio, Accepted) was calculated to characterize the correctness of the burn scar boundaries. The  $EE$  is the mean error between an evaluated edge location  $\text{Burn}(eval)$  to the minimum of geometric normal of the line segment ( $\perp$ ) connecting the two nearest neighbors ( $NN$ ) in a target burn,  $\text{Burn}(tgt)_{NN1}$  and  $\text{Burn}(tgt)_{NN2}$ , or the closest of the two  $NN$  such that for a  $\text{Burn}(eval)$  with  $n$  edge locations:

$$EE = \sum_i^n \frac{EE_i}{n}$$

Where

$$EE_i = \min(EE_{NN}, EE_{Norm})$$

and

$$EE_{NN} = d(\text{Burn}(eval_i), \text{Burn}(tgt)_{NN1})$$

and

$$EE_{Norm} = d(\text{Burn}(eval_i) \perp [\text{Burn}(tgt)_{NN1}, \text{Burn}(tgt)_{NN2}])$$

For each combination of mapped and reference burn scars,  $EE$  quantifies the difference between the boundary of a mapped burn scar to the edge of a reference burn scar which can be directly interpreted as the average distance from any location on the mapped burn scar boundary to the true boundary. It should be noted that  $EE$  is independent of the overlapping area metrics, as it evaluates the burn perimeter rather than the overlapping area.

Reference burn boundaries were selected from the Arctic-Boreal Vulnerability Experiment (ABOVE) Wildfire dataset (Loboda and Hall, 2017), which provides a large collection of fire scar perimeters mapped at medium spatial resolution (30 m)

for fires which occurred between 2001 and 2015. The ABoVE Wildfire dataset was compiled as part of the ABoVE Program and includes fire boundaries from the Natural Resources Canada's Canadian National Fire Database (Natural Resources Canada, no date) and the Alaska Interagency Coordination Center (AICC, no date). In the case of the Canadian National Fire Database, it is noted that "[...] the data contained in the CNFDB [Canadian National Fire Database] are not complete nor are they without error. Not all fires have been mapped, and data accuracy varies due to different mapping techniques. This collection includes only data that has been contributed by the agencies. Data completeness and quality vary among agencies and between years" (<http://cwfis.cfs.nrcan.gc.ca/ha/nfdb>). The dataset, therefore, has an unknown error rate, presumably favoring errors of omission, which precludes its use as a true reference dataset from which robust estimates can be derived. Although the ABoVE dataset cannot be considered a complete census of the fire activity, the fire perimeters which were identified were assumed to be of high quality and used to evaluate the accuracy of the burn scar shapes extracted from MCD64A1.

The performance of the MUSE algorithm was compared to the Fire Atlas (Andela *et al.*, 2019), which to the best of the authors' knowledge is the only publicly available, systematically generated satellite-derived dataset providing individual fire characteristics including the fire boundary as of the time of writing. The Fire Atlas was also derived from the MCD64A1 product, but identifies individual fires by tracking the expansion of the fire from an ignition point using a three-step process which identifies ignition points, determines the threshold for fire propagation from

pixel-to-pixel, and finally adjusts outliers along the edges of the burn scar (Andela *et al.*, 2019).

Validation and intercomparison of the fire identification algorithm was conducted for the period from 2003 to 2015. This range represents the overlap period between the MODIS Burned Area archive used by MUSE (2001 – current), the Arctic-Boreal Vulnerability Experiment (ABoVE) Wildfire dataset (2001 – 2015) used for validation (Loboda and Hall, 2017), and the Global Fire Atlas dataset (2003 – 2016) which is used as a benchmark for comparison (Andela *et al.*, 2019).

### Results

In line with previous studies which have emphasized the relatively small contribution of smaller fires to the regional burning totals in North American boreal forests (Stocks *et al.*, 2002; Gillett *et al.*, 2004; Kasischke and Turetsky, 2006; Girardin and Mudelsee, 2008), the analysis was limited to burns larger than 200 ha. Between 2003 and 2015, MUSE identified 11,056 individual fires while the Fire Atlas identified 55,187. Due primarily to omissions of small fires in the ABoVE dataset and commission errors in MCD64A1, the Fire Atlas intersected 4,218 of the ABoVE fires while MUSE intersected 3,464. On average, one ABoVE reference fire corresponded to 3.11 MUSE fires and 8.00 Fire Atlas fires. Recalling that both products are derived from MCD64A1, this difference in the number of fires identified can be attributed to differences in the extraction algorithms.

The edge error (*EE*) metric and overlapping area indices (*OS* and *US*) were calculated using the ABoVE burn scar boundaries as reference data, with the MUSE and Fire Atlas boundaries analyzed as the classified data. Due to the extreme spatial

distortions in the sinusoidal projection in the circumpolar latitudes, *EE* was computed in the North America Equidistant Conic Projection due to its inherently distance-based calculation. On the other hand, *OS* and *US* were computed in the Sinusoidal Projection as they are area-based calculations.

As shown in Table 4.3 and Figure 4.3, the MUSE fire boundaries in all years have an *EE* of less than 2 times the one-sided dimension of the MODIS 500-m cell (463.3127 m). The Fire Atlas *EE* is below this threshold in all years except 2004. This finding is in line with a similar analysis of MCD64A1 undertaken for the Western United States (Humber, Boschetti and Giglio, Accepted). In all years except 2015, MUSE is an improvement over the Fire Atlas for edge error, which can likely be attributed to the Fire Atlas' tendency to oversegment burns. It should be noted that the maximum difference is approximately 180 m, or less than 40% of the MODIS cell dimension.

*Table 4.3. Edge Error metrics (in meters) for individual fires extracted from MCD64A1 vs. ABoVE reference fires. Fire Atlas - MUSE indicates the difference in median distance from mapped-to-reference boundaries between algorithms.*

<b><i>Year</i></b>	<b><i>MUSE</i></b>	<b><i>Fire Atlas</i></b>	<b><i>Fire Atlas - MUSE</i></b>
2003	590.50	614.21	23.70
2004	835.86	936.70	100.84
2005	672.24	788.72	116.48
2006	397.13	452.21	55.07
2007	570.48	675.00	104.52
2008	694.69	735.22	40.53
2009	782.05	820.46	38.41
2010	579.34	675.94	96.59
2011	730.37	829.59	99.22
2012	526.15	531.63	5.47
2013	571.48	626.80	55.32
2014	740.17	920.36	180.19
2015	679.17	661.99	-17.18

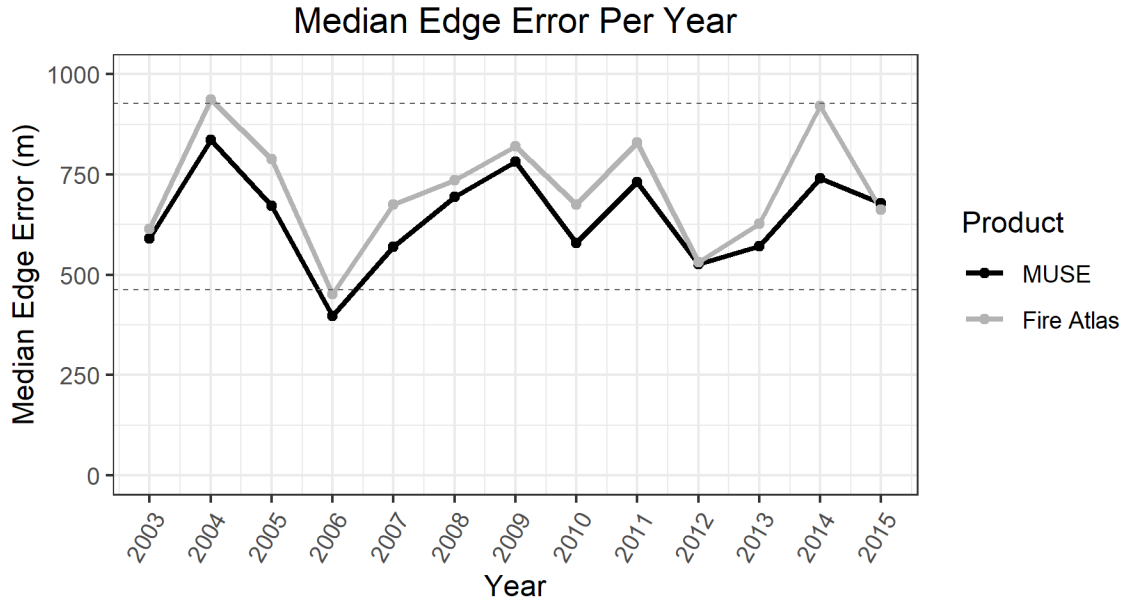


Figure 4.3. Graph of Edge Error through time for individual fires extracted from MCD64A1 vs. ABoVE reference fires. The gray dashed line indicates 1x MODIS cell dimension, the black dashed line indicates 2x MODIS cell dimension.

Regarding *OS* and *US*, there is a stronger tendency to oversegment (versus undersegment) for both MUSE and the Fire Atlas. Recalling that *OS* and *US* are related to omission and commission errors, respectively, these results agree with prior pixel-based validation results indicating MCD64A1’s prevalence of omission errors (Boschetti *et al.*, 2019). For all years, the median *OS* and *US* errors for the MUSE boundaries were lower than for the Fire Atlas. For both products and in all years, *US* errors are smaller than *OS* errors (Table 4.2, Figure 4.4).

Table 4.4. Oversegmentation (*OS*) and Undersegmentation (*US*) errors for individual fires extracted from MCD64A1 vs. ABoVE reference fires. Fire Atlas - MUSE indicates the difference in the error metric between algorithms.

Year	Oversegmentation			Undersegmentation		
	Fire Atlas	MUSE	Fire Atlas - MUSE	Fire Atlas	MUSE	Fire Atlas - MUSE
2003	0.54	0.52	0.01	0.18	0.16	0.02
2004	0.65	0.63	0.02	0.14	0.10	0.04
2005	0.55	0.47	0.08	0.18	0.14	0.04
2006	0.48	0.40	0.08	0.19	0.17	0.01
2007	0.58	0.52	0.07	0.18	0.15	0.03
2008	0.60	0.53	0.07	0.11	0.09	0.02

2009	0.64	0.62	0.02	0.16	0.10	0.06
2010	0.61	0.55	0.07	0.10	0.09	0.01
2011	0.66	0.61	0.05	0.22	0.12	0.10
2012	0.53	0.48	0.05	0.14	0.12	0.02
2013	0.57	0.54	0.03	0.14	0.12	0.03
2014	0.55	0.50	0.05	0.09	0.07	0.02
2015	0.59	0.54	0.06	0.25	0.13	0.11

### Median Oversegmentation and Undersegmentation Per Year

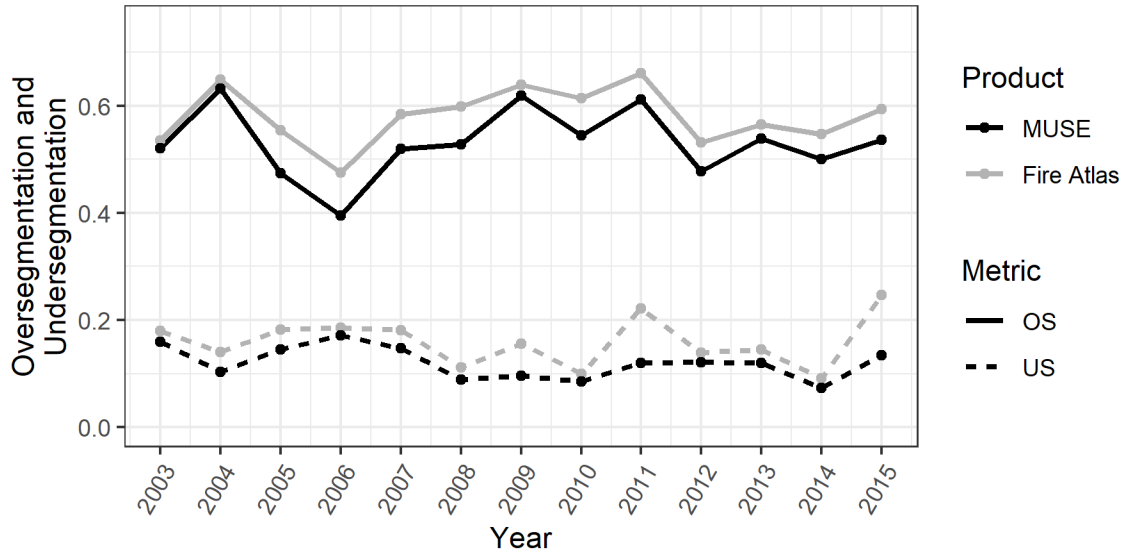


Figure 4.4. Graph of Oversegmentation (OS) and Undersegmentation (US) errors through time for individual fires extracted from MCD64A1 vs. ABoVE reference fires.

Qualitatively, MUSE has a tendency to create small, artificial unburned islands within the boundary of the burn scar due to the removal of small clusters of burned cells which, though spatially adjacent to the surrounding cells, do not overlap with the temporal burn date range (Figure 4.5). The Fire Atlas does not remove small clusters burned cells and therefore does not demonstrate this behavior. However, MUSE appears to better represent the shape of the fire due to its tendency to identify larger connected segments.

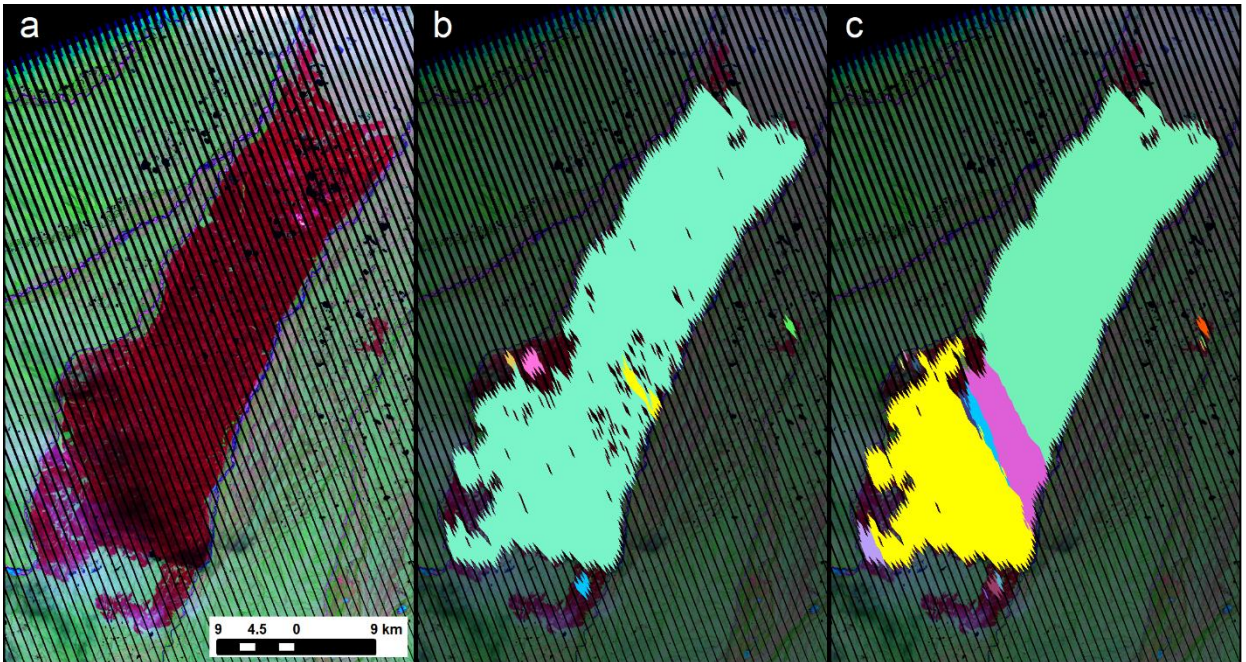


Figure 4.5. The 2007 Anuktavuk Fire. (a) Landsat-7 Path 073 Rows 011-012 composite (June 2008; R=Mid IR, G=NIR, B=Red). (b) MUSE overlapping fire segments. (c) Fire Atlas overlapping fire segments. In (b) and (c), each color corresponds to an individual extracted fire segment. Note that MCD64A1 underestimates the area of the burn, which propagates into the extraction algorithms.

As an example, the Anuktavuk River Fire (Figure 4.5), which burned over the course of three months in 2007 in the north Alaskan tundra and is known from previous studies to have burned over 100,000 ha and was the largest and longest burning tundra fire on record (Jones *et al.*, 2009; Mack *et al.*, 2011). The main body of the burn scar was underestimated by MCD64A1, likely due to issues with the MODIS water mask (Giglio *et al.*, 2018), resulting in MUSE identifying the main body of the fire as 81,484 ha with an additional smaller attached segment of 515 ha. By contrast, the Fire Atlas subdivided the main body of the fire into nine distinct segments, the largest of which was approximately 51,792 ha followed by a segment of 26,496 ha. This is consistent with results throughout the study area indicating the tendency of both fire extraction algorithms to oversegment individual fires into multiple fragments, though MUSE creates fewer total fragments.

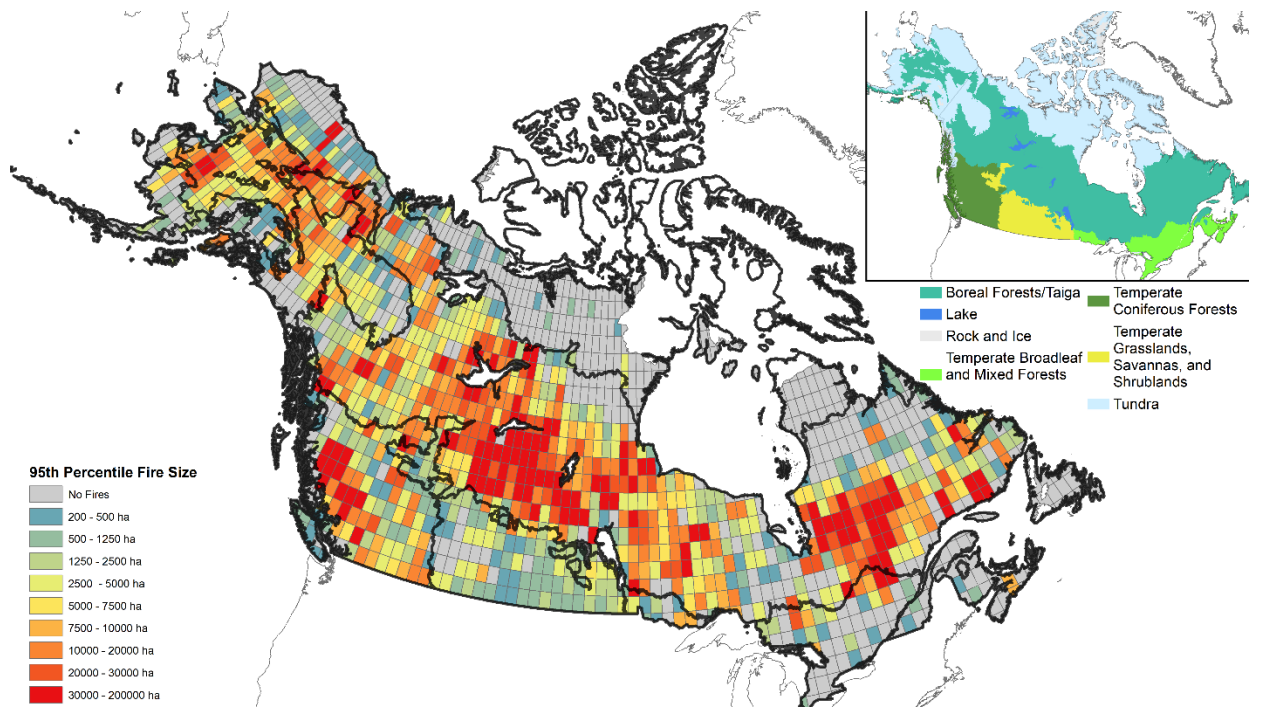


Figure 4.6. The 95th percentile fire size for 1-degree cells, based on the 2002 through 2018 fire years according to the MUSE algorithm.

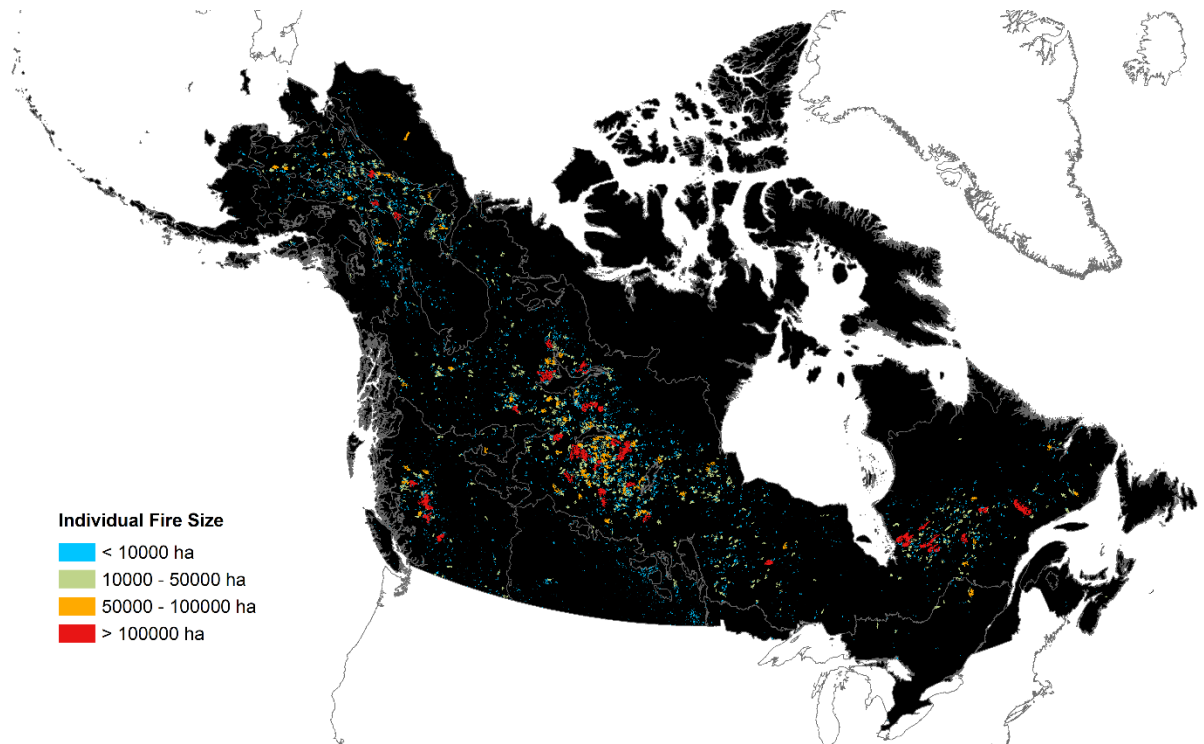


Figure 4.7. Size of individual fires throughout any of the 2002 to 2018 fire seasons according to the MUSE algorithm.

Throughout the study area, the largest fires were generally found in the boreal region as expected (Figure 4.6 and Figure 4.7). These fires span the breadth of the continent, with concentrations of very large fires (> 100,000 ha) found in central Canada (Saskatchewan, Alberta, and Northern Territories), central Quebec, and eastern Alaska. Due to the large number of fires in the biome, trends in boreal fires drive patterns for all of Alaska and Canada.

Large (50,000 to 100,000 ha) and very large fires are generally rare in the tundra biome, with occasional medium-sized fires (10,000 to 50,000 ha) present among an overwhelming majority of small fires (< 10,000 ha). Total burned area in the tundra was driven entirely by small and medium sizes fires, with exceptions in 2007 (the Anaktuvuk River Fire, which burned in northern Alaska) and 2004/5 which experienced an abnormal amount of burning along the Canada-Alaska border.

### Discussion and Conclusions

Fire size and shape are important parameters for characterizing individual fire spread which can be correlated with fire intensity, severity, emission rates, and smoke plume injection heights (Amiridis *et al.*, 2010; Turetsky *et al.*, 2011; Archibald *et al.*, 2013). Furthermore, fire size and shape directly influence fire succession (Fuller, 1991; Whelan, 1995; Turner *et al.*, 1998) and soil erosion (Gill and Allan, 2009). The proximity of boreal forests and tundra fires to Arctic permafrost underlies the importance of understanding specific fire characteristics in these areas, as black carbon from smoke plumes has the potential to be transported to snow and ice-covered surfaces and consequently impact surface albedo (Hansen and Nazarenko, 2004; Kim *et al.*, 2005).

Coarse spatial resolution satellite-derived products such as MODIS MCD64A1 (Giglio *et al.*, 2018) have provided valuable and systematic daily observations of fire activity over nearly two decades. In this work, a modified flood-fill algorithm (MUSE) is implemented for extracting individual fires from the MCD64A1 archive based on the temporal uncertainty of the day of burning. The results are driven by the availability of clear surface observations rather than empirically defined thresholds and therefore make fewer assumptions about the spread rate of fires on the surface. An object-based accuracy assessment showed the MUSE algorithm provides better representation of individual fire segments than the publicly available Fire Atlas (Andela *et al.*, 2019) for almost all metrics and fire years when compared to the ABoVE reference dataset (AICC, no date; Natural Resources Canada, no date; Loboda and Hall, 2017).

The results show distinct spatial patterns across Canada and Alaska, with concentrations of very large fires in the boreal regions of Alaska as well as central and eastern Canada (, ). Recent large and very large fires were also identified in British Columbia, which have been documented by the Canadian Government in mountain pine beetle affected forests (British Columbia Wildfire Service, 2018). While these results should be considered specific to MCD64A1 and require confirmation from additional data sources, they indicate that the MUSE algorithm provides a plausible description of individual fire sizes over large areas.

In future work, a pressing need is to evaluate the patterns of individual fire shapes and sizes extracted MCD64A1 through comparison with other products such as the regionally-tuned Arctic Boreal Burned Area (ABBA) product (Loboda *et al.*,

2011) in order to independently confirm the presence of spatial fire size patterns observed in this study. Qualitative inspection of the C6 MCD64A1 product indicates that the product may suffer from omission errors due to inconsistencies in the water mask flags, causing “perforations” in contiguous burned cells. These errors propagate into the MUSE algorithm’s workflow and can artificially reduce the size of individual fires.

Additionally, given that the MUSE algorithm is not calibrated to any specific region, the algorithm can theoretically be applied globally. This analysis can, therefore, be expanded to include the boreal and tundra biomes in Eurasia to better understand how wildfire activity affected by changes in climate, and whether any such changes are in line with the expectations outlined in previous work that predicted increases in fire size, severity, and frequency (Balshi *et al.*, 2009; Flannigan *et al.*, 2009; Abatzoglou and Kolden, 2011; Barrett *et al.*, 2011; de Groot, Flannigan and Cantin, 2013; French *et al.*, 2015).

## Chapter 5 – Discussion and Conclusions

### Summary of Findings

This research undertook the analysis of large-area fire patterns from an object-based perspective, using individual fires derived from existing earth observations datasets as the basic unit of analysis. Improved characterization of individual fire attributes is relevant to landscape management, climatological studies, and fire ecology. The purpose of the object-based approach is assess satellite-derived fire products to provide additional types of fire-related attributes to users (such as individual fire size, aggregated size distributions, and fire shapes) and to evaluate the efficacy of these derived data points.

First, an intercomparison of the four publicly available global burned area products was conducted to identify the relative strengths and weaknesses of the products and to examine their similarities and inconsistencies. Next, a novel edge error metric was proposed as part of a framework for analyzing errors in individual fire boundaries derived from satellite data. Finally, a fire extraction algorithm was developed and used to map fire size patterns in Canada and Alaska at the biome level. The performance of the algorithm was evaluated within the previously proposed edge error framework against a similar dataset, the Fire Atlas, using publicly available fire boundary data.

The intercomparison of four global burned area products (Chapter 2) consisted of wall-to-wall global analysis of the amount of burned area identified by Fire CCI (v 4.1), Copernicus Burnt Area (SPOT-Vegetation), MODIS Collection 5.1 MCD45A1,

and MODIS Collection 6 MCD64A1 for the overlapping observation period of 2005 to 2011. The Collection 6 MCD64A1 product identified the highest total burned area of any product globally, though this varied significantly from region to region. On the other hand, the Copernicus Burnt Area product identified the least amount of burned area globally, and the algorithm appeared to have a flaw which caused the amount of burned area detected to decrease year by year (this was later acknowledged by Copernicus, and identified as the reason the product was rescinded<sup>7</sup>). Furthermore, Copernicus identified the least burned area in regions which contribute the most to global burned area totals (Africa and Australia), and the most burned area in regions which burn relatively little (temperate and boreal regions). MCD45A1 and Fire CCI identified the second- and third- most burned area and were the most similar in terms of total burned area identified, though MCD45A1 showed better correlation to MCD64A1 at the Thiessen Scene Area (Gallego, 2005; Kennedy, Yang and Cohen, 2010) level than Fire CCI.

The temporal patterns of burning identified by MCD64A1, MCD45A1, and Fire CCI products all corresponded well to the timing of MCD14ML active fire detections, which were used as a proxy for fire seasonality. Notably, Fire CCI appeared to extend the burning periods by one month for regions with less burning relative to MCD64A1. The Copernicus Burnt Area product was notably different from the other products and, in many regions of the world, was out of phase with the active fire detections, meaning the product identified periods of high amounts of

---

<sup>7</sup> <https://land.copernicus.eu/global/content/burnt-area-1km-spotvgt-unavailable>

burning when there were few active fires and low amounts of burning when there were many active fires.

The results of this investigation varied greatly from region to region, as expected, and the intercomparison underscored the need for users of burned area products to understand the classification tendencies of each product. This also raised the bigger question of distributing satellite-derived products without providing clear and useful quality assessment indicators to end-users. Based on this study, the MCD64A1 product was selected for use in later objectives due to its temporal fidelity and the tendency to identify the most overall burned area.

It is important to bear in mind that product intercomparison cannot replace validation for determining the accuracy of a product in a given location because the correctness of the products is not assessed – the majority (or all) products could plausibly omit or commit errors in any specific location. To properly assess product accuracy, validation is still a necessary exercise. Recent emphasis has been placed on improving the process and adoption of burned area validation in order to achieve CEOS Cal/Val Stage 3, representing a spatiotemporal accuracy assessment using statistically robust sampled reference data, and CEOS Cal/Val Stage 4 which is the same as Stage 3 but applied on a continuous basis. Protocols were proposed by Padilla *et al.* (2015, 2017) and Boschetti *et al.* (2016) and implemented by Boschetti *et al.* (2019) and Chuvieco *et al.* (2018).

While these assessments are helpful for obtaining consistent estimates of burned area across many fires and at large scales, such pixel-based approaches do not necessarily characterize how well individual fires are mapped. In order to better

evaluate the accuracy of individual fires, a method was proposed for evaluating wildfire classification maps while retaining the spatially explicit properties of the burn scar using individual fires as the unit for analysis. The method quantified the edge error of burned area classifications and reference maps by calculating the average geometric normal of the evaluated burned area boundary along the burn edge and the two nearest neighbor samples from the reference burn boundary.

Additionally, in order to account for the low resolution bias associated with comparing coarse and medium resolution classifications, the minimum achievable edge error was calculated as the optimized solution which accounts for the amount of edge error attributable only to the random placement of high-resolution burned cells nested within coarse-resolution cells (i.e. error which cannot be attributed to misclassification).

The edge error metric was demonstrated by comparing 500 m MODIS MCD64A1 maps to 30 m Monitoring Trends in Burn Severity (MTBS; Eidenshink *et al.*, 2007) maps for 173 wildfires in the United States. Importantly, the edge error did not appear to show any pattern related to fire size while other commonly used object-based metrics (undersegmentation and oversegmentation) tended to report larger errors as the size of the fires decreased. This is intuitive because oversegmentation and undersegmentation are based on measurements of (2-dimensional) area, while the edge error metric measurement is based on (1-dimensional) distances between points. The results of the edge error calculations showed that, when accounting for the minimum achievable edge error due to differing spatial resolutions, the mean edge error of the MCD64A1 product was less than twice the MODIS edge dimension and

did not change with fire size. This indicates that while visually and qualitatively the MCD64A1 map appears to lack fine detail, quantitatively the product represents fire boundaries accurately compared to 10 m reference data.

Having determined that MCD64A1 appears capable of retaining the shapes of individual fires, the product was then used as input to a new shape extraction algorithm named the MODIS Uncertainty-based Single-fire Extraction (MUSE) algorithm. The algorithm's approach is novel in its use of the per-pixel temporal uncertainty from the MCD64A1 product to determine the threshold for fire propagation across the landscape, whereas other works use empirically defined thresholds to accomplish the same goal (Mouillot and Field, 2005; Hantson *et al.*, 2015; Hantson, Pueyo and Chuvieco, 2015; Oom *et al.*, 2016; Andela *et al.*, 2018).

The algorithm was applied in Canada and Alaska and used to observe patterns in fire sizes throughout the MODIS era (2002 to present). Individual fires identified by the MUSE algorithm were validated using single-fire polygons compiled in the Arctic-Boreal Vulnerability Experiment (ABOVE) wildfire dataset (Loboda and Hall, 2017), derived from the Natural Resources Canada's Canadian National Fire Database (Canada, no date) and the Alaska Interagency Coordination Center (Alaska Interagency Coordination Center, no date). When compared to the Fire Atlas database (Andela *et al.*, 2018), the performance of the MUSE algorithm was better in nearly all years for the edge error, oversegmentation, and undersegmentation metrics. Additionally, the MUSE algorithm demonstrated a lower propensity for fragmenting individual fires and better captured the main body of fires, while the Fire Atlas tended to divide individual fires into several equal-sized objects.

Fires were analyzed at the biome level and split into four categories in line with other studies (Kasischke and Turetsky, 2006): small fires (<10,000 ha), medium fires (10,000 to 50,000 ha), large fires (50,000 to 100,000 ha), and very large fires (>100,000 ha). As expected, the largest fires were typically found in the boreal biome. However, the contribution of very large fires to the total amount of burned area, as well as the number of very large fires, was shown to have increased since 2010 according to the MCD64A1 dataset. This observation could support theories relating climate change and fire size, i.e. that weather patterns in a given fire season are more likely to favor the uninhibited spread of fires across the landscape, leading to an increase in size and severity (Abatzoglou and Kolden, 2011), but needs to be confirmed through verification with other datasets. Additional large fires were observed in British Columbia in recent years, which is consistent with known severe fires in mountain pine beetle affected forests (British Columbia Wildfire Service, 2018).

### *Impact and Importance to the Broader Community*

In Chapter 2, the inventory of publicly available burned area products was evaluated to determine how well each broadly represented fire patterns around the world. This work has been cited by other authors for a variety of purposes, including as justification of a burned area product choice (e.g. Andela *et al.*, 2018; McWethy *et al.*, 2018), as an overview of burned area products (e.g. Giglio *et al.*, 2018; Elliott *et al.*, 2019; Lasko, 2019), as evidence of significant regional differences in burned area products (e.g. Brennan *et al.*, 2019; Chuvieco *et al.*, 2019; Forkel *et al.*, 2019), and as a framework for similar comparison exercises (e.g. Rodrigues *et al.*, 2019).

The intercomparison exercise should be repeated as new burned area products become available. This is particularly important in the current era of free and inexpensive high-powered computing resources, which has made the production of Earth observations datasets attainable for an increasing number of organizations. Systems such as Google Earth Engine (Gorelick *et al.*, 2017) have made Earth observations data and map classification widely available to expert and non-expert users through simple yet powerful programming interfaces. While these advances can generally be considered as positive for promoting remote sensing data uptake and transparency, arguable the availability of these resources has promoted iterative and incremental improvements to datasets rather than stable product releases.

Under this new iterative product development paradigm, in less than two years since the manuscript associated with Chapter 2 was originally published the list of publicly available burned area products has changed drastically: The Copernicus Programme has released two new PROBA-V-based Burnt Area products (at 1 km and 300m), deprecated two products (PROBA-V 1 km, SPOT-Vegetation 1 km), and will soon release a new version of the 300 m PROBA-V product. The Fire CCI program, in addition to the MERIS-based Fire CCI v3.1 and v4.1 products, released the MODIS-based Fire CCI v5.0 and 5.1, the AVHRR-based Fire CCI Long Term Beta product known as FIRE CCI LT10, and the Fire CCI SFD v1.1 Small Fire Dataset based on Sentinel-2. A VIIRS-base analog to MCD64A1 is planned for release in the near future, though the product (to be named VNP64A1) is a transition of the MCD64A1 burned area product to the VIIRS platform. This list is by no means exhaustive, and does not include products developed by other researchers over

smaller areas. In the absence of direct product intercomparison, users of burned area products are left to make partially informed decisions about products based on product specifications or accuracy assessments calculated from sampled data which are unlikely to capture anomalous behavior over small regions.

Chapters 3 and 4 of this dissertation focused on using and evaluating burned area maps from an object-based perspective, ultimately for the purpose of observing spatial and temporal patterns in fire size. A recent trend, including work in this dissertation, involves extracting individual burns from burned area maps for the purpose of determining the properties of individual fires which can include geometry as well as intensity, spread rate, and other attributes (Andela *et al.*, 2018; Laurent *et al.*, 2018). The edge error metric proposed in Chapter 3 provides a method for evaluating the derived fire products in a manner that is more in-line with their intended use (as descriptors of individual fires) than pixel-based accuracy metrics. The accuracy of specific objects is of immediate interest to the community, as these properties can be used in global vegetation models (Yue *et al.*, 2014, 2015). Additionally, because attributes like fire size and perimeter-to-area ratio are correlated with other attributes such as smoke injection height, emission rates, and intensity (Amiridis *et al.*, 2010; Turetsky *et al.*, 2011; Archibald *et al.*, 2013), it is important to understand how accurately the shape characteristics are represented.

As proof of the efficacy of the edge error metric, individual fires were extracted from the MCD64A1 burned area product and compared to the MTBS (Eidenshink *et al.*, 2007) fire boundaries. This demonstration showed that over a sample of 173 fires, the edge errors were less than two times the one-sided dimension

of the MODIS 500-m pixel, which is a significant finding indicating that, for well-mapped fires, the errors introduced by differences in spatial resolution are relatively small.

As new sensors such as the European Space Agency's Sentinel-2 MSI and PlanetScope provide increasingly finer spatial resolution observations (10 m and 3 m, respectively) with shorter revisit times (5 days and daily, respectively), the capacity to observe small fires and fine details of burn scars has improved accordingly. In fact, two recent products implement Sentinel-2 MSI and Landsat-8 OLI observations for mapping burned area in Africa (Roteta *et al.*, 2019; Roy *et al.*, 2019). Evidence presented by those authors suggests that these higher spatial resolution products are able to deliver on the promise of better small fire mapping than coarse spatial resolution counterparts such as the MODIS-derived products.

The additional capacity to detect fine-scale features in burn scars makes these datasets inherently useful for individual fire mapping. Object-based accuracy assessment using metrics such as the edge error proposed in this work are natural candidates to evaluate medium and high-resolution fire classifications. Though higher resolution sensors like PlanetScope (3 m), Pleiades (0.5 m), WorldView-3 (0.3 m) and others lack the shortwave infrared bands conventionally used for mapping burning automatically, they certainly provide the spatial resolution necessary to create photointerpreted validation datasets which can be used to assess medium spatial resolution products (Roy *et al.*, 2019).

Arguably, a pitfall of the drastic increase in sensor spatial resolutions is the loss of the "homogenizing" effect which coarse-resolution sensors have on pixel

observations. For burned area mapping, this means incomplete combustion and patchiness within fire perimeters is more likely to be observed by the sensor, a prevalence of which has been shown to increase with spatial resolution (Price, Russell-Smith and Edwards, 2003). Accurately representing these properties can require sub-pixel measure such as the fraction burned and combustion completeness (“*f.cc*”, Roy *et al.*, 2019) rather than discrete burned/unburned labels.

Chapter 4 provided two contributions to the current body of research. First, a novel algorithm for extracting individual fires from the MCD64A1 product was introduced. The MUSE algorithm exploits the temporal uncertainty of MCD64A1 to reconstruct a range of plausible burn dates. This represents a methodological improvement over previous algorithms because it is driven by data available from the burned area product itself, rather than by empirically defined thresholds.

The algorithm results were used to identify fires in Canada and Alaska, and distinct spatial patterns of fire size were observed on a yearly basis. Consistent with the results of previous studies, the largest fires were observed in the boreal biome (Kasischke *et al.*, 2010; French *et al.*, 2015). Recent large fires in mountain pine beetle affected forests in British Columbia were captured by the dataset as well. While the analysis provides qualitatively plausible results, the Collection 6 MCD64A1 product suffers from omission errors in high latitudes due to issues with the MODIS water mask. Such omission errors appear to lead to the fragmentation of large burns, reducing the overall fire sizes in the near-polar regions. Therefore, it is important to confirm the observed fire size patterns using other datasets such as the regionally adapted Arctic Boreal Burned Area (ABBA) product (Loboda *et al.*, 2011).

A shift in fire sizes in Canada since 2010 was observed in the boreal biome and in British Columbia since 2010. This merits additional study and ongoing monitoring due to the proximity to vulnerable arctic snow and ice, which can be covered in soot from wildfires leading to decreased surface albedo ultimately resulting in melting. These results are relevant to current events, as media outlets have expressed concern over the severity of the ongoing 2019 fire season in the Arctic (Fresco, 2019; Harball, 2019; NASA Earth Observatory, 2019; *BBC News*, 2019). Additionally, fire patterns in Canada and Alaska have long been assumed to be highly susceptible to changes brought on by climate change (Gillett *et al.*, 2004; M. D. Flannigan *et al.*, 2009; M. Flannigan *et al.*, 2009; Abatzoglou and Kolden, 2011; de Groot, Flannigan and Cantin, 2013; French *et al.*, 2015). The dataset generated in this work can provide a valuable contribution to evaluating whether these assumptions are being realized.

#### *Directions for Future Work*

Wall-to-wall product intercomparison is a simple but effective activity that should be undertaken periodically, ideally as new burned area products become available. As previously mentioned, the three programs which produced the maps used for intercomparison – NASA, Fire CCI, and Copernicus – have combined to release or have impending releases of eight new burned area products in addition to the four products which were evaluated. Therefore, there is a pressing need to evaluate these new products in order to provide users with up-to-date information about product performance and suitability for specific study areas and periods.

A disadvantage of direct product intercomparison is that the methods are unable to capture product accuracy, meaning validation studies are still necessary. For spatially and temporally robust burned area accuracy assessment which requires higher resolution reference data, statistical sampling is a practical solution because of the effort required to generate high-quality reference data sets and sampling strategies have been proposed (Padilla *et al.*, 2015, 2017; Boschetti, Stehman and Roy, 2016). These strategies are stratified based on independently derived spatial and temporal patterns in fire activity in order to define strata to improve sampling efficiency. However, these sampling methods cannot be directly used to validate burn shapes because they are not optimized for fire size, which affects the inclusion probabilities of individual fires, i.e. a specific big fire is more likely to appear in a random sample than a specific small fire. Future work which focuses on statistically rigorous sampling of individual fires must take into account fire boundaries which are covered by clouds which obscure parts of the fire boundary and fires that are in actively spreading at the time of observation.

Datasets providing the boundaries of individual burns are relatively new, with no known products being created in an operational mode. While the MUSE algorithm was implemented for Canada and Alaska in Chapter 4, in ongoing work the algorithm has already been applied globally for the period spanning March 2002 to February 2019. The preliminary global results seem qualitatively reasonable and indicate that the algorithm may perform effectively outside of the boreal and surrounding regions. Future work will focus on improving the MUSE algorithm, most notably by improving the handling of small clusters of burned cells which are removed in the

current version. Although the product was validated in Canada and Alaska, this is a data-rich environment with existing high-quality datasets that are typically not available in most of the world. Validating the outputs of the MUSE algorithm for much of the world presents a major challenge due to the lack of available reference data, though it is debatable whether the shape and area of individual fires has any significance in areas with low biomass and high annual burned area such as African and Australian savannahs.

Barriers to further improvements in any thresholded flood-fill based algorithm include the lack of calibration and validation data for assessing the product performance and a lack of methods for evaluating the accuracy of these products. The edge error metric is one of several potential metrics for quantifying the error in the burn shapes, but access to reference data remains an issue. Many existing validation datasets are not suitable for object-based accuracy assessment because, in accordance with the CEOS Cal/Val protocol (Boschetti, Roy and Justice, 2009), they can include partial burns since only the burning between two dates is evaluated by a photointerpreter. Object-based accuracy assessment requirements are stricter in this regard because the entire burn shape must be evaluated, which additionally implies a lack of cloud cover (which can be flagged separately in the CEOS protocol). Publicly available datasets suitable for use as reference data in fire size analysis are limited to the Monitoring Trends in Burn Severity project in the United States (Eidenshink *et al.*, 2007) and the ABoVE wildfire dataset for Canada and Alaska (AICC, no date; Natural Resources Canada, no date; Loboda and Hall, 2017).

Finally, investigation into possible changes in fire regimes focusing on individual fire properties is essential as global climate patterns continue to change. The fire size analysis can easily be expanded to include other vulnerable ecosystems, including the Eurasian Arctic and Boreal regions and the Amazon. The increasing length of the archive of fire observations from satellite earth observation should reduce the uncertainties in identifying change through time, enabling a better understanding of the relationships between fire and other biological, physical, and climatological variables.

## References

- Abatzoglou, J. and Kolden, C. (2011) ‘Climate Change in Western US Deserts: Potential for Increased Wildfire and Invasive Annual Grasses Fire and Invasive Plants Special Feature Climate Change in Western US Deserts: Potential for Increased Wildfire and Invasive Annual Grasses’, *Rangeland Ecology & Management*, 64, pp. 471–478.
- Abatzoglou, J. T. and Williams, A. P. (2016) ‘Human-caused climate change is now a key driver of forest fire activity in the western United States’, *Proceedings of the National Academy of Sciences*, 113(42), pp. 11649–11650. doi: 10.1073/pnas.1612926113.
- Adamek, T. and O’Connor, N. (2004) ‘Efficient contour-based shape representation and matching’, in *dl.acm.org*, p. 138. doi: 10.1145/973264.973287.
- Ager, A. A., Vaillant, N. M. and Finney, M. A. (2010) ‘A comparison of landscape fuel treatment strategies to mitigate wildland fire risk in the urban interface and preserve old forest structure’, *Forest Ecology and Management*, 259(8), pp. 1556–1570. doi: 10.1016/j.foreco.2010.01.032.
- AICC (no date) *Alaska Interagency Coordination Center*. Available at: <https://fire.ak.blm.gov/> (Accessed: 18 July 2019).
- Alonso-Canas, I. and Chuvieco, E. (2015) ‘Global burned area mapping from ENVISAT-MERIS and MODIS active fire data’, *Remote Sensing of Environment*, 163, pp. 140–152. doi: 10.1016/j.rse.2015.03.011.
- Amiridis, V. *et al.* (2010) ‘Smoke injection heights from agricultural burning in Eastern Europe as seen by CALIPSO’, *Atmospheric Chemistry and Physics*, 10(23), pp. 11567–11576. doi: 10.5194/acp-10-11567-2010.
- Andela, N. *et al.* (2017) ‘A human-driven decline in global burned area’, *Science*, 356(6345), pp. 1356–1362. doi: 10.1126/science.aal4108.
- Andela, N. *et al.* (2018) ‘The Global Fire Atlas of individual fire size, duration, speed, and direction’, *Earth System Science Data Discussions*, pp. 1–28. doi: 10.5194/essd-2018-89.
- Andreou, I. and Sgouros, N. M. (2005) ‘Computing, explaining and visualizing shape similarity in content-based image retrieval’, *Information Processing and Management*, 41(5), pp. 1121–1139. doi: 10.1016/j.ipm.2004.08.008.
- Archibald, S. and Roy, D. P. (2009) ‘Identifying individual fires from satellite-derived burned area data’, in *International Geoscience and Remote Sensing Symposium (IGARSS)*. doi: 10.1109/IGARSS.2009.5417974.

- Archibald, S. *et al.* (2010) ‘Southern African fire regimes as revealed by remote sensing’, *International Journal of Wildland Fire*, 19(7), p. 861. doi: 10.1071/WF10008.
- Archibald, S. *et al.* (2013) ‘Defining pyromes and global syndromes of fire regimes.’, *Proceedings of the National Academy of Sciences of the United States of America*, 110(16), pp. 6442–7. doi: 10.1073/pnas.1211466110.
- Balshi, M. S. *et al.* (2009) ‘Assessing the response of area burned to changing climate in western boreal North America using a Multivariate Adaptive Regression Splines (MARS) approach’, *Global Change Biology*, 15(3), pp. 578–600. doi: 10.1111/j.1365-2486.2008.01679.x.
- Baraldi, A., Humber, M. and Boschetti, L. (2013) ‘Quality assessment of pre-classification maps generated from spaceborne/airborne multi-spectral images by the satellite image automatic mapper<sup>TM</sup> and atmospheric/topographic correction<sup>TM</sup>-spectral classification software products: Part 2 - experimental result’, *Remote Sensing*, 5(10). doi: 10.3390/rs5105209.
- Barbosa, P. M., Stroppiana, D. and Cardoso, J. M. (1999) ‘An assessment of vegetation fire in Africa (1981-1991): Burned areas, burned biomass, and atmospheric emissions’, *Africa*, 13(4), pp. 933–950.
- Barrett, K. *et al.* (2011) ‘Potential shifts in dominant forest cover in interior Alaska driven by variations in fire severity’, *Ecological Applications*, 21(7), pp. 2380–2396. doi: 10.1890/10-0896.1.
- Barrett, K. *et al.* (2016) ‘Static and dynamic controls on fire activity at moderate spatial and temporal scales in the Alaskan boreal forest’, *Ecosphere*, 7(11), p. e01572. doi: 10.1002/ecs2.1572.
- BBC News* (2019) ‘The Arctic is on fire - how bad is it?’, 2 August. Available at: <https://www.bbc.com/news/world-europe-49125391> (Accessed: 11 September 2019).
- Bentley, J. L. (1975) ‘Multi-dimensional binary search trees used for associated searching’, *Commun. ACM*, 18(9), pp. 509–517. doi: 10.1145/361002.361007.
- Bond, W. J. and Keeley, J. E. (2005) ‘Fire as a global “herbivore”: the ecology and evolution of flammable ecosystems’, *Trends in Ecology & Evolution*, 20(7), pp. 387–394. doi: 10.1016/j.tree.2005.04.025.
- Bond, W. J., Woodward, F. I. and Midgley, G. F. (2005) ‘The global distribution of ecosystems in a world without fire’, *New Phytologist*, 165(2), pp. 525–538. doi: 10.1111/j.1469-8137.2004.01252.x.

Boschetti, L. *et al.* (2004) 'Lessons to be learned from the comparison of three satellite-derived biomass burning products', *Geophysical Research Letters*, 31(21), p. n/a–n/a. doi: 10.1029/2004GL021229.

Boschetti, L. *et al.* (2006) 'A sampling method for the retrospective validation of global burned area products', *IEEE Transactions on Geoscience and Remote Sensing*, 44(7). doi: 10.1109/TGRS.2006.874039.

Boschetti, L. *et al.* (2008) 'A MODIS assessment of the summer 2007 extent burned in Greece', *International Journal of Remote Sensing*, 29(8), pp. 2433–2436. doi: 10.1080/01431160701874561.

Boschetti, L. *et al.* (2010) 'Global assessment of the temporal reporting accuracy and precision of the MODIS burned area product', *International Journal of Wildland Fire*, 19(6), p. 705. doi: 10.1071/wf09138.

Boschetti, L. *et al.* (2015) 'MODIS-Landsat fusion for large area 30m burned area mapping', *Remote Sensing of Environment*, 161. doi: 10.1016/j.rse.2015.01.022.

Boschetti, L. *et al.* (2019) 'Global validation of the Collection 6 MODIS burned area product', *Remote Sensing of Environment*, *Accepted*.

Boschetti, L., Flasse, S. P. and Brivio, P. A. (2004) 'Analysis of the conflict between omission and commission in low spatial resolution dichotomic thematic products: The Pareto Boundary', *Remote Sensing of Environment*, 91(3), pp. 280–292. doi: 10.1016/j.rse.2004.02.015.

Boschetti, L. and Roy, D. P. (2008) 'Defining a fire year for reporting and analysis of global interannual fire variability', *Journal of Geophysical Research: Biogeosciences*, 113(G3), p. G03020. doi: 10.1029/2008JG000686.

Boschetti, L., Roy, D. and Justice, C. (2009) 'International Global Burned Area Satellite Product Validation Protocol Part I—production and standardization of validation reference data', *Unpublished data*.

Boschetti, L., Stehman, S. V. and Roy, D. P. (2016) 'A stratified random sampling design in space and time for regional to global scale burned area product validation', *Remote Sensing of Environment*, 186, pp. 465–478. doi: 10.1016/j.rse.2016.09.016.

Bowman, D. M. J. S. *et al.* (2009) 'Fire in the earth system', *Science*. doi: 10.1126/science.1163886.

Bowman, D. M. J. S. *et al.* (2011) 'The human dimension of fire regimes on Earth', *Journal of Biogeography*, 38(12), pp. 2223–2236. doi: 10.1111/j.1365-2699.2011.02595.x.

Brennan, J. *et al.* (2019) ‘Theoretical uncertainties for global satellite-derived burned area estimates’, *Biogeosciences*, 16(16), pp. 3147–3164. doi: <https://doi.org/10.5194/bg-16-3147-2019>.

British Columbia Wildfire Service (2018) *Wildfire Season Summary - Province of British Columbia, Wildfire Season Summary*. Available at: <https://www2.gov.bc.ca/gov/content/safety/wildfire-status/about-bcws/wildfire-history/wildfire-season-summary> (Accessed: 9 August 2019).

Bruzzone, L. and Persello, C. (2010) ‘A Novel Protocol for Accuracy Assessment in Classification of Very High-resolution Images’, *IEEE Transactions on Geoscience and Remote Sensing*, 48(3), pp. 1232–1244. doi: 10/dp638h.

Canada, N. R. (no date) *Canadian Wildland Fire Information System | Canadian National Fire Database*. Available at: <http://cwfis.cfs.nrcan.gc.ca/ha/nfdb?type=poly&year=9999> (Accessed: 18 July 2019).

Cao, C. *et al.* (2013) ‘Suomi NPP VIIRS sensor data record verification, validation, and long-term performance monitoring’, *Journal of Geophysical Research: Atmospheres*, 118(20), pp. 11,664–11,678. doi: 10.1002/2013JD020418.

Cao, C. *et al.* (2014) ‘Early On-Orbit Performance of the Visible Infrared Imaging Radiometer Suite Onboard the Suomi National Polar-Orbiting Partnership (S-NPP) Satellite’, *IEEE Transactions on Geoscience and Remote Sensing*, 52(2), pp. 1142–1156. doi: 10.1109/TGRS.2013.2247768.

*CEOS Land Product Validation Subgroup* (no date). Available at: <https://lpvs.gsfc.nasa.gov/> (Accessed: 19 July 2019).

Chang, D. and Song, Y. (2009) ‘Comparison of L3JRC and MODIS global burned area products from 2000 to 2007’, *Journal of Geophysical Research: Atmospheres*, 114(D16), p. D16106. doi: 10.1029/2008JD011361.

Chen, D. *et al.* (2018) ‘Strong cooling induced by stand-replacing fires through albedo in Siberian larch forests’, *Scientific Reports*, 8(1), p. 4821. doi: 10.1038/s41598-018-23253-1.

Chuvieco, E. *et al.* (2016) ‘A new global burned area product for climate assessment of fire impacts’, *Global Ecology and Biogeography*, 25(5), pp. 619–629. doi: 10.1111/geb.12440.

Chuvieco, E. *et al.* (2018) ‘Generation and analysis of a new global burned area product based on MODIS 250-m reflectance bands and thermal anomalies’, *Earth System Science Data*, 10(4), pp. 2015–2031. doi: 10.5194/essd-10-2015-2018.

- Chuvieco, E. *et al.* (2019) ‘Historical background and current developments for mapping burned area from satellite Earth observation’, *Remote Sensing of Environment*, 225, pp. 45–64. doi: 10.1016/j.rse.2019.02.013.
- Clinton, N. *et al.* (2010) ‘Accuracy assessment measures for object-based image segmentation goodness’, *Photogrammetric Engineering and remote sensing*, 76(3), pp. 289–299. doi: 10.14358/PERS.76.3.289.
- Csiszar, I. A., Morisette, J. T. and Giglio, L. (2006) ‘Validation of active fire detection from moderate-resolution satellite sensors: the MODIS example in northern Eurasia’, *IEEE Transactions on Geoscience and Remote Sensing*, 44(7), pp. 1757–1764. doi: 10.1109/TGRS.2006.875941.
- Davies, D. K. *et al.* (2009) ‘Fire Information for Resource Management System: Archiving and Distributing MODIS Active Fire Data’, *IEEE Transactions on Geoscience and Remote Sensing*, 47(1), pp. 72–79. doi: 10.1109/TGRS.2008.2002076.
- Descloitres, J. *et al.* (2002) ‘The MODIS fire products’, *Remote Sensing of Environment*, 83(1–2), pp. 244–262.
- D’Odorico, P. *et al.* (2014) ‘Intercomparison of fraction of absorbed photosynthetically active radiation products derived from satellite data over Europe’, *Remote Sensing of Environment*, 142, pp. 141–154. doi: 10.1016/j.rse.2013.12.005.
- Duffy, P. A. *et al.* (2005) ‘Impacts of Large-Scale Atmospheric–Ocean Variability on Alaskan Fire Season Severity’, *Ecological Applications*, 15(4), pp. 1317–1330. doi: 10.1890/04-0739.
- Eidenshink, J. *et al.* (2007) ‘Project for monitoring trends in burn severity’, *Fire ecology*. Available at: <http://agris.fao.org/agris-search/search.do?recordID=US201300881952> (Accessed: 14 September 2015).
- Elliott, M. *et al.* (2019) ‘Planned and unplanned fire regimes on public land in south-east Queensland’, *International Journal of Wildland Fire*. doi: 10.1071/WF18213.
- Flannigan, M. *et al.* (2009) ‘Impacts of climate change on fire activity and fire management in the circumboreal forest’, *Global Change Biology*, 15(3), pp. 549–560. doi: 10.1111/j.1365-2486.2008.01660.x.
- Flannigan, M. D. *et al.* (2009) ‘Implications of changing climate for global wildland fire’, *International Journal of Wildland Fire*, 18(5), pp. 483–507. doi: 10.1071/WF08187.
- Forkel, M. *et al.* (2019) ‘Emergent relationships with respect to burned area in global satellite observations and fire-enabled vegetation models’, *Biogeosciences*, 16(1), pp. 57–76. doi: 10.5194/bg-16-57-2019.

- Frantz, D. *et al.* (2016) 'Fire spread from MODIS burned area data: obtaining fire dynamics information for every single fire', *International Journal of Wildland Fire*, 25(12), p. 1228. doi: 10.1071/wf16003.
- French, N. H. F. *et al.* (2015) 'Fire in arctic tundra of Alaska: past fire activity, future fire potential, and significance for land management and ecology', *International Journal of Wildland Fire*, 24(8), pp. 1045–1061. doi: 10.1071/WF14167.
- Fuller, M. (1991) *Forest fires : an introduction to wildland fire behavior, management, firefighting, and prevention*. Available at: <https://www.cabdirect.org/cabdirect/abstract/19920657858>.
- Fresco, N. (2019) *Huge wildfires in the Arctic and far North send a planetary warning*, *The Conversation*. Available at: <http://theconversation.com/huge-wildfires-in-the-arctic-and-far-north-send-a-planetary-warning-121167> (Accessed: 11 September 2019).
- Gallego, F. J. (2005) 'Stratified sampling of satellite images with a systematic grid of points', *ISPRS Journal of Photogrammetry and Remote Sensing*, 59(6), pp. 369–376. doi: 10.1016/j.isprsjprs.2005.10.001.
- Garrigues, S. *et al.* (2008) 'Validation and intercomparison of global Leaf Area Index products derived from remote sensing data', *Journal of Geophysical Research: Biogeosciences*, 113(G2), p. n/a–n/a. doi: 10.1029/2007JG000635.
- Gavin, D. G. *et al.* (2007) 'Forest fire and climate change in western North America: insights from sediment charcoal records', *Frontiers in Ecology and the Environment*, 5(9), pp. 499–506. doi: 10.1890/060161.
- GCOS (2019) *Fire: Essential Climate Variable (ECV) Factsheet*. Available at: <https://gcos.wmo.int/en/essential-climate-variables/ecv-factsheets>
- GEO (2019) 'GEO Initiative: Global Wildfire Information System (GWIS) Implementation Plan'. Available at: [https://www.earthobservations.org/documents/gwp20\\_22/GWIS.pdf](https://www.earthobservations.org/documents/gwp20_22/GWIS.pdf) (Accessed: 11 October 2019).
- Giglio, L. *et al.* (2003) 'An Enhanced Contextual Fire Detection Algorithm for MODIS', *Remote Sensing of Environment*, 87(2), pp. 273–282. doi: 10.1016/S0034-4257(03)00184-6.
- Giglio, L. *et al.* (2006) 'Global estimation of burned area using MODIS active fire observations', *Atmospheric Chemistry and Physics*, 6(4), pp. 957–974. doi: <https://doi.org/10.5194/acp-6-957-2006>.

Giglio, L. *et al.* (2008) 'Active fire detection and characterization with the advanced spaceborne thermal emission and reflection radiometer (ASTER)', *Remote Sensing of Environment*, 112(6), pp. 3055–3063. doi: 10.1016/j.rse.2008.03.003.

Giglio, L. *et al.* (2009) 'An active-fire based burned area mapping algorithm for the MODIS sensor', *Remote Sensing of Environment*, 113(2), pp. 408–420.

Giglio, L. *et al.* (2010) 'Assessing variability and long-term trends in burned area by merging multiple satellite fire products', *Biogeosciences*, 7(3), pp. 1171–1186. doi: <https://doi.org/10.5194/bg-7-1171-2010>.

Giglio, L. *et al.* (2016) *Collection 6 MODIS Burned Area product User Guide*, NASA.

Giglio, L. *et al.* (2018) 'The Collection 6 MODIS burned area mapping algorithm and product', *Remote Sensing of Environment*, 217, pp. 72–85. doi: 10.1016/j.rse.2018.08.005.

Giglio, L., Randerson, J. T. and van der Werf, G. R. (2013) 'Analysis of daily, monthly, and annual burned area using the fourth-generation global fire emissions database (GFED4)', *Journal of Geophysical Research: Biogeosciences*, 118(1), pp. 317–328. doi: 10.1002/jgrg.20042.

Giglio, L., Schroeder, W. and Justice, C. O. (2016) 'The collection 6 MODIS active fire detection algorithm and fire products', *Remote Sensing of Environment*, 178, pp. 31–41. doi: 10.1016/j.rse.2016.02.054.

Gill, A. M. and Allan, G. (2009) 'Large fires, fire effects and the fire-regime concept', *International Journal of Wildland Fire*, 17(6), pp. 688–695. doi: 10.1071/WF07145.

Gillett, N. P. *et al.* (2004) 'Detecting the effect of climate change on Canadian forest fires', *Geophysical Research Letters*, 31(18). doi: 10.1029/2004GL020876.

Girardin, M. P. and Mudelsee, M. (2008) 'Past and Future Changes in Canadian Boreal Wildfire Activity', *Ecological Applications*, 18(2), pp. 391–406. doi: 10.1890/07-0747.1.

*GOCF Gold* (no date). Available at: <http://gofc-fire.umd.edu/> (Accessed: 28 August 2019).

Gorelick, N. *et al.* (2017) 'Google Earth Engine: Planetary-scale geospatial analysis for everyone', *Remote Sensing of Environment*. (Big Remotely Sensed Data: tools, applications and experiences), 202, pp. 18–27. doi: 10.1016/j.rse.2017.06.031.

Gregoire, J.-M. *et al.* (2006) 'A sampling method for the retrospective validation of global burned area products', *IEEE Transactions on Geoscience and Remote Sensing*, 44(7), pp. 1765–1773. doi: 10.1109/tgrs.2006.874039.

de Groot, W. J., Flannigan, M. D. and Cantin, A. S. (2013) ‘Climate change impacts on future boreal fire regimes’, *Forest Ecology and Management*. (The Mega-fire reality), 294, pp. 35–44. doi: 10.1016/j.foreco.2012.09.027.

Günsel, B. and Tekalp, A.M. (1998) ‘Shape similarity matching for query-by-example’, *Elsevier*, 31(7), pp. 931–944.

Hall, J. V. *et al.* (2016) ‘A MODIS-based burned area assessment for Russian croplands: Mapping requirements and challenges’, *Remote Sensing of Environment*, 184, pp. 506–521. doi: 10.1016/j.rse.2016.07.022.

Hall, J. V. and Loboda, T. V. (2017) ‘Quantifying the Potential for Low-Level Transport of Black Carbon Emissions from Cropland Burning in Russia to the Snow-Covered Arctic’, *Frontiers in Earth Science*, 5. doi: 10.3389/feart.2017.00109.

Hansen, J. and Nazarenko, L. (2004) ‘Soot climate forcing via snow and ice albedos’, *Proceedings of the National Academy of Sciences*, 101(2), pp. 423–428. doi: 10.1073/pnas.2237157100.

Hantson, S. *et al.* (2015) ‘Anthropogenic effects on global mean fire size’, *International Journal of Wildland Fire*, 24(5), p. 589. doi: 10.1071/wf14208.

Hantson, S., Pueyo, S. and Chuvieco, E. (2015) ‘Global fire size distribution is driven by human impact and climate’, *Global Ecology and Biogeography*, 24(1), pp. 77–86. doi: 10.1111/geb.12246.

Harball, E. (2019) “‘There is no silver lining’: why Alaska fires are a glimpse of our climate future”, *The Guardian*, 23 August. Available at: <https://www.theguardian.com/cities/2019/aug/23/there-is-no-silver-lining-why-alaska-fires-are-a-glimpse-of-our-climate-future> (Accessed: 11 September 2019).

Hawbaker, T. J. *et al.* (2008) ‘Detection rates of the MODIS active fire product in the United States’, *Remote Sensing of Environment*. (Earth Observations for Terrestrial Biodiversity and Ecosystems Special Issue), 112(5), pp. 2656–2664. doi: 10.1016/j.rse.2007.12.008.

Herold, M. *et al.* (2008) ‘Some challenges in global land cover mapping: An assessment of agreement and accuracy in existing 1 km datasets’, *Remote Sensing of Environment*. (Earth Observations for Terrestrial Biodiversity and Ecosystems Special Issue), 112(5), pp. 2538–2556. doi: 10.1016/j.rse.2007.11.013.

Higuera, P. E. *et al.* (2011) ‘Peak detection in sediment–charcoal records: impacts of alternative data analysis methods on fire-history interpretations’, *International Journal of Wildland Fire*, 19(8), pp. 996–1014. doi: 10.1071/WF09134.

Homer, C. *et al.* (2015) ‘Completion of the 2011 National Land Cover Database for the Conterminous United States – Representing a Decade of Land Cover Change

Information’, *Photogrammetric Engineering & Remote Sensing*. doi: 10.14358/PERS.81.5.345.

Houborg, R. and McCabe, M. F. (2018) ‘A Cubesat enabled Spatio-Temporal Enhancement Method (CESTEM) utilizing Planet, Landsat and MODIS data’, *Remote Sensing of Environment*, 209, pp. 211–226. doi: 10.1016/j.rse.2018.02.067.

Humber, M. L. *et al.* (2019) ‘Spatial and temporal intercomparison of four global burned area products’, *International Journal of Digital Earth*, 12(4). doi: 10.1080/17538947.2018.1433727.

Humber, M. L., Boschetti, L. and Giglio, L. (Accepted) ‘Assessing the shape accuracy of coarse resolution burned area identifications’, *IEEE Transactions on Geoscience and Remote Sensing*.

IPCC (2012) ‘Managing the Risks of Extreme Events and Disasters to Advance Climate Change Adaptation’, Available from Cambridge University Press, The Edinburgh Building, Shaftesbury Road, Cambridge CB2 8RU ENGLAND, 582 pp. Available from June 2012

Jones, B. M. *et al.* (2009) ‘Fire Behavior, Weather, and Burn Severity of the 2007 Anaktuvuk River Tundra Fire, North Slope, Alaska’, *Arctic, Antarctic, and Alpine Research*, 41(3), pp. 309–316. doi: 10.1657/1938-4246-41.3.309.

Justice, C. O. and Dowty, P. (1994) ‘IGBP-DIS satellite fire detection algorithm workshop technical report’, *IGBP-DIS working paper*, 9, p. 88.

Justice, C. O., Townshend, J. R. G., *et al.* (2002(a)) ‘An overview of MODIS Land data processing and product status’, *Remote Sensing of Environment*. (The Moderate Resolution Imaging Spectroradiometer (MODIS): a new generation of Land Surface Monitoring), 83(1–2), pp. 3–15. doi: 10.1016/S0034-4257(02)00084-6.

Justice, C. O., Giglio, L., *et al.* (2002b) ‘The MODIS fire products’, *Remote Sensing of Environment*. (The Moderate Resolution Imaging Spectroradiometer (MODIS): a new generation of Land Surface Monitoring), 83(1–2), pp. 244–262. doi: 10.1016/S0034-4257(02)00076-7.

Justice, C. O., Giglio, L., *et al.* (2002) ‘The MODIS fire products’, *Remote Sensing of Environment*. (The Moderate Resolution Imaging Spectroradiometer (MODIS): a new generation of Land Surface Monitoring), 83(1–2), pp. 244–262. doi: 10.1016/S0034-4257(02)00076-7.

Justice, C. O. *et al.* (2003) ‘A review of current space-based fire monitoring in Australia and the GOFCC/GOLD program for international coordination’, *International Journal of Wildland Fire*, 12(4), pp. 247–258. doi: 10.1071/wf03013.

- Kasischke, E. S. *et al.* (2010) ‘Alaska’s changing fire regime — implications for the vulnerability of its boreal forests’, *Canadian Journal of Forest Research*, 40(7), pp. 1313–1324. doi: 10.1139/X10-098.
- Kasischke, E. S. and Turetsky, M. R. (2006) ‘Recent changes in the fire regime across the North American boreal region—Spatial and temporal patterns of burning across Canada and Alaska’, *Geophysical Research Letters*, 33(9). doi: 10.1029/2006GL025677.
- Kennedy, R. E., Yang, Z. and Cohen, W. B. (2010) ‘Detecting trends in forest disturbance and recovery using yearly Landsat time series: 1. LandTrendr — Temporal segmentation algorithms’, *Remote Sensing of Environment*, 114(12), pp. 2897–2910. doi: 10.1016/j.rse.2010.07.008.
- Kim, Y. *et al.* (2005) ‘Possible effect of boreal wildfire soot on Arctic sea ice and Alaska glaciers’, *Atmospheric Environment*, 39(19), pp. 3513–3520. doi: 10.1016/j.atmosenv.2005.02.050.
- de Klerk, H. (2008) ‘A pragmatic assessment of the usefulness of the MODIS (Terra and Aqua) 1-km active fire (MOD14A2 and MYD14A2) products for mapping fires in the fynbos biome’, *International Journal of Wildland Fire*, 17(2), pp. 166–178. doi: 10.1071/WF06040.
- Korontzi, S., Justice, C. O. and Scholes, R. J. (2003) ‘Influence of timing and spatial extent of savanna fires in southern Africa on atmospheric emissions’, *Journal of Arid Environments*, 54(2), pp. 395–404. doi: 10.1006/jare.2002.1098.
- Krinner, G. *et al.* (2005) ‘A dynamic global vegetation model for studies of the coupled atmosphere-biosphere system’, *Global Biogeochemical Cycles*, 19(1). doi: 10.1029/2003GB002199.
- Land SIPS / Earthdata* (no date). Available at: <https://earthdata.nasa.gov/eosdis/sips/land-sips> (Accessed: 20 August 2019).
- Lasko, K. (2019) ‘Incorporating Sentinel-1 SAR imagery with the MODIS MCD64A1 burned area product to improve burn date estimates and reduce burn date uncertainty in wildland fire mapping’, *Geocarto International*, 0(0), pp. 1–21. doi: 10.1080/10106049.2019.1608592.
- Laurent, P. *et al.* (2018) ‘FRY, a global database of fire patch functional traits derived from space-borne burned area products’, *Scientific Data*, 5, p. 180132. doi: 10.1038/sdata.2018.132.
- Leblon, B., Bourgeau-Chavez, L. and San-Miguel-Ayanz, J. (2012) ‘Sustainable development-authoritative and leading edge content for environmental management’, *Use of Remote Sensing in Wildfire Management*, pp. 55–81.

- Lehsten, V., de Groot, W. and Sallaba, F. (2016) 'Fuel fragmentation and fire size distributions in managed and unmanaged boreal forests in the province of Saskatchewan, Canada', *Forest Ecology and Management*, 376, pp. 148–157. doi: 10.1016/j.foreco.2016.06.014.
- Loboda, T. V. *et al.* (2011) 'Mapping burned area in Alaska using MODIS data: a data limitations-driven modification to the regional burned area algorithm', *International Journal of Wildland Fire*, 20(4), p. 487. doi: 10.1071/wf10017.
- Loboda, T. V. *et al.* (2012) 'Regional fire monitoring and characterization using global NASA MODIS fire products in dry lands of Central Asia', *Frontiers of Earth Science*, 6(2), pp. 196–205. doi: 10.1007/s11707-012-0313-3.
- Loboda, T. V. and Hall, J. V. (2017) 'ABOVE: Wildfire Date of Burning within Fire Scars across Alaska and Canada, 2001-2015', *ORNL DAAC*. doi: <https://doi.org/10.3334/ORNLDAAC/1559>.
- Mack, M. C. *et al.* (2011) 'Carbon loss from an unprecedented Arctic tundra wildfire', *Nature*, 475(7357), pp. 489–492. doi: 10.1038/nature10283.
- Malamud, B. D., Millington, J. D. A. and Perry, G. L. W. (2005) 'Characterizing wildfire regimes in the United States', *Proceedings of the National Academy of Sciences*, 102(13), pp. 4694–4699. doi: 10.1073/pnas.0500880102.
- Marlon, J. R. *et al.* (2008) 'Climate and human influences on global biomass burning over the past two millennia', *Nature Geoscience*, 1(10), pp. 697–702. doi: 10.1038/ngeo313.
- McWethy, D. B. *et al.* (2018) 'Landscape drivers of recent fire activity (2001-2017) in south-central Chile', *PLOS ONE*, 13(8), p. e0201195. doi: 10.1371/journal.pone.0201195.
- MODIS Adaptive Processing System (MODAPS) SIPS / Earthdata* (no date). Available at: <https://earthdata.nasa.gov/eosdis/sips/modaps-sips> (Accessed: 20 August 2019).
- Moreira, F. *et al.* (2011) 'Landscape – wildfire interactions in southern Europe: Implications for landscape management', *Journal of Environmental Management*. Academic Press, 92(10), pp. 2389–2402. doi: 10.1016/J.JENVMAN.2011.06.028.
- Morisette, J. T. *et al.* (2005) 'Validation of the MODIS active fire product over Southern Africa with ASTER data', *International Journal of Remote Sensing*, 26(19), pp. 4239–4264. doi: 10.1080/01431160500113526.
- Mouillot, F. and Field, C. B. (2005) 'Fire history and the global carbon budget: a 1°× 1° fire history reconstruction for the 20th century', *Global Change Biology*, 11(3), pp. 398–420. doi: 10.1111/j.1365-2486.2005.00920.x.

NASA Earth Observatory (2019) *Arctic Fires Fill the Skies with Soot*. Available at: <https://earthobservatory.nasa.gov/images/145380/arctic-fires-fill-the-skies-with-soot> (Accessed: 9 August 2019).

Nasreddine, K., Benzinou, A. and Fablet, R. (2010) 'Variational shape matching for shape classification and retrieval', *Pattern Recognition Letters*, 31(12), pp. 1650–1657. doi: 10.1016/j.patrec.2010.05.014.

Natural Resources Canada (no date) *Canadian Wildland Fire Information System / Canadian National Fire Database*. Available at: <http://cwfis.cfs.nrcan.gc.ca/ha/nfdb?type=poly&year=9999> (Accessed: 18 July 2019).

Nogueira, J. M. P. *et al.* (2017) 'Can we go beyond burned area in the assessment of global remote sensing products with fire patch metrics?', *Remote Sensing*, 9(1). doi: 10.3390/rs9010007.

Olson, D. M. *et al.* (2001) 'Terrestrial Ecoregions of the World: A New Map of Life on Earth: A new global map of terrestrial ecoregions provides an innovative tool for conserving biodiversity', *BioScience*, 51(11), pp. 933–938. doi: 10.1641/0006-3568(2001)051[0933:TEOTWA]2.0.CO;2.

Oom, D. *et al.* (2016) 'Highlighting biome-specific sensitivity of fire size distributions to time-gap parameter using a new algorithm for fire event individuation', *Remote Sensing*, 8(8). doi: 10.3390/rs8080663.

Padilla, M. *et al.* (2015) 'Comparing the accuracies of remote sensing global burned area products using stratified random sampling and estimation', *Remote Sensing of Environment*, 160, pp. 114–121. doi: 10.1016/j.rse.2015.01.005.

Padilla, M. *et al.* (2017) 'Stratification and sample allocation for reference burned area data', *Remote Sensing of Environment*, 203, pp. 240–255. doi: 10.1016/j.rse.2017.06.041.

Padilla, M., Stehman, S. V and Chuvieco, E. (2014) 'Validation of the 2008 MODIS-MCD45 global burned area product using stratified random sampling', *Remote Sensing of Environment*, 144, pp. 187–196. doi: 10.1016/j.rse.2014.01.008.

Patterson, W. A., Edwards, K. J. and Maguire, D. J. (1987) 'Microscopic charcoal as a fossil indicator of fire', *Quaternary Science Reviews*, 6(1), pp. 3–23. doi: 10.1016/0277-3791(87)90012-6.

Pausas, J. G. and Keeley, J. E. (2009) 'A Burning Story: The Role of Fire in the History of Life', *BioScience*, 59(7), pp. 593–601. doi: 10.1525/bio.2009.59.7.10.

Pechony, O. and Shindell, D. T. (2010) 'Driving forces of global wildfires over the past millennium and the forthcoming century', *Proceedings of the National Academy of Sciences*, 107(45), pp. 19167–19170. doi: 10.1073/pnas.1003669107.

- Persello, C. and Bruzzone, L. (2010) 'A Novel Protocol for Accuracy Assessment in Classification of Very High Resolution Images', *IEEE Transactions on Geoscience and Remote Sensing*, 48(3), pp. 1232–1244. doi: 10.1109/TGRS.2009.2029570.
- Pflugmacher, D. *et al.* (2011) 'Comparison and assessment of coarse-resolution land cover maps for Northern Eurasia', *Remote Sensing of Environment*, 115(12), pp. 3539–3553. doi: 10.1016/j.rse.2011.08.016.
- Plummer, S. *et al.* (2006) 'Establishing A Earth Observation Product Service For The Terrestrial Carbon Community: The Globcarbon Initiative', *Mitigation and Adaptation Strategies for Global Change*, 11(1), pp. 97–111. doi: 10.1007/s11027-006-1012-8.
- Price, O., Russell-Smith, J. and Edwards, A. (2003) 'Fine-scale patchiness of different fire intensities in sandstone heath vegetation in northern Australia', *International Journal of Wildland Fire*. CSIRO PUBLISHING, 12(2), p. 227. doi: 10.1071/WF03040.
- Pyne, S. J. (2007) 'Problems, paradoxes, paradigms: triangulating fire research', *International Journal of Wildland Fire*, 16(3), pp. 271–276.
- Randerson, J. T. *et al.* (2006) 'The Impact of Boreal Forest Fire on Climate Warming', *Science*, 314(5802), pp. 1130–1132. doi: 10.1126/science.1132075.
- Randerson, J. T. *et al.* (2012) 'Global burned area and biomass burning emissions from small fires', *Journal of Geophysical Research: Biogeosciences*, 117(G4), p. G04012. doi: 10.1029/2012JG002128.
- Reid, C. E. *et al.* (2016) 'Critical Review of Health Impacts of Wildfire Smoke Exposure', *Environmental Health Perspectives*, 124(9), pp. 1334–1343. doi: 10.1289/ehp.1409277.
- Rommel, T. K. and Perera, A. H. (2002) 'Accuracy of discontinuous binary surfaces: a case study using boreal forest fires', *International Journal of Geographical Information Science*, 16(3), pp. 287–298. doi: 10.1080/13658810110096209.
- Rodrigues, J. A. *et al.* (2019) 'How well do global burned area products represent fire patterns in the Brazilian Savannas biome? An accuracy assessment of the MCD64 collections', *International Journal of Applied Earth Observation and Geoinformation*. Elsevier, 78, pp. 318–331. doi: 10.1016/J.JAG.2019.02.010.
- Rossi, S. *et al.* (2016) 'FAOSTAT estimates of greenhouse gas emissions from biomass and peat fires', *Climatic Change*, 135(3–4), pp. 699–711. doi: 10.1007/s10584-015-1584-y.

- Roteta, E. *et al.* (2019) ‘Development of a Sentinel-2 burned area algorithm: Generation of a small fire database for sub-Saharan Africa’, *Remote Sensing of Environment*, 222, pp. 1–17. doi: 10.1016/j.rse.2018.12.011.
- Roy, D. P. (1999) ‘Multi-temporal active-fire based burn scar detection algorithm’, *International Journal of Remote Sensing*, 20(5), pp. 1031–1038. doi: 10.1080/014311699213073.
- Roy, D. P. *et al.* (2008) ‘The collection 5 MODIS burned area product — Global evaluation by comparison with the MODIS active fire product’, *Remote Sensing of Environment*, 112(9), pp. 3690–3707. doi: 10.1016/j.rse.2008.05.013.
- Roy, D. P. *et al.* (2019) ‘Landsat-8 and Sentinel-2 burned area mapping - A combined sensor multi-temporal change detection approach’, *Remote Sensing of Environment*, 231, p. 111254. doi: 10.1016/j.rse.2019.111254.
- Roy, D. P., Jin, Y., *et al.* (2005) ‘Prototyping a global algorithm for systematic fire-affected area mapping using MODIS time series data’, *Remote Sensing of Environment*, 97(2), pp. 137–162. doi: 10.1016/j.rse.2005.04.007.
- Roy, D. P., Frost, P. G. H., *et al.* (2005) ‘The Southern Africa Fire Network (SAFNet) regional burned-area product-validation protocol’, *International Journal of Remote Sensing*, 26(19), pp. 4265–4292. doi: 10.1080/01431160500113096.
- Roy, D. P. and Boschetti, L. (2009) ‘Southern Africa Validation of the MODIS, L3JRC, and GlobCarbon Burned-Area Products’, *IEEE Transactions on Geoscience and Remote Sensing*, 47(4), pp. 1032–1044. doi: 10.1109/TGRS.2008.2009000.
- Roy, D.P., Boschetti, L. and Smith, A.M. (2013) Satellite remote sensing of fires. *Fire Phenomena and the Earth System*, pp.77-93.
- Rucker, G. and Tiemann, J. (2012) ‘Eleven Years of MODIS Burned Areas: A GIS Analysis for the Territory of the United Republic of Tanzania’. Ministry of Natural Resources and Tourism, Dar es Salaam.
- Russell-Smith, J. *et al.* (2009) ‘Improving estimates of savanna burning emissions for greenhouse accounting in northern Australia: limitations, challenges, applications’, *International Journal of Wildland Fire*. CSIRO PUBLISHING, 18(1), p. 1. doi: 10.1071/WF08009.
- Sánchez, R. R., Heil, A. and Chuvieco, E. (2014) ‘Product Intercomparison Report (PIR). Version 1.4.’ Available at: [http://esa-fire-cci.org/webfm\\_send/762](http://esa-fire-cci.org/webfm_send/762).
- Schindler, K. and Suter, D. (2008) ‘Object detection by global contour shape’, *Pattern Recognition*. Pergamon, 41(12), pp. 3736–3748. doi: 10.1016/J.PATCOG.2008.05.025.

- Schroeder, W. *et al.* (2008) ‘Validation of GOES and MODIS active fire detection products using ASTER and ETM+ data’, *Remote Sensing of Environment*. (Earth Observations for Terrestrial Biodiversity and Ecosystems Special Issue), 112(5), pp. 2711–2726. doi: 10.1016/j.rse.2008.01.005.
- Scott, A. C. and Glasspool, I. J. (2006) ‘The diversification of Paleozoic fire systems and fluctuations in atmospheric oxygen concentration’, *Proceedings of the National Academy of Sciences*, 103(29), pp. 10861–10865. doi: 10.1073/pnas.0604090103.
- Seiler, W. and Crutzen, P. J. (1980) ‘Estimates of gross and net fluxes of carbon between the biosphere and the atmosphere from biomass burning’, *Climatic Change*, 2(3), pp. 207–247. doi: 10.1007/BF00137988.
- Shapiro, L. G. and Stockmann, G. C. (2001) ‘Binary image analysis’, *Computer Vision*, pp. 69–75.
- Sparks, A. M. *et al.* (2015) ‘An accuracy assessment of the MTBS burned area product for shrub-steppe fires in the northern Great Basin, United States’, *International Journal of Wildland Fire*, 24(1), pp. 70–78. doi: 10.1071/WF14131.
- Stehman, S. V. and Czaplewski, R. L. (1998) ‘Design and Analysis for Thematic Map Accuracy Assessment: Fundamental Principles’, *Remote Sensing of Environment*, 64(3), pp. 331–344. doi: 10.1016/S0034-4257(98)00010-8.
- Stocks, B. J. *et al.* (2002) ‘Large forest fires in Canada, 1959–1997’, *Journal of Geophysical Research: Atmospheres*, 107(D1), p. FFR 5-1-FFR 5-12. doi: 10.1029/2001JD000484.
- Stohl, A. *et al.* (2006) ‘Pan-Arctic enhancements of light absorbing aerosol concentrations due to North American boreal forest fires during summer 2004’, *Journal of Geophysical Research: Atmospheres*, 111(D22). doi: 10.1029/2006JD007216.
- Sugihara, N. G. *et al.* (2006) *Fire in California’s ecosystems*. University of California Press. Available at: <https://nau.pure.elsevier.com/en/publications/fire-in-californias-ecosystems> (Accessed: 18 August 2019).
- Syphard, A. D. *et al.* (2017) ‘Human presence diminishes the importance of climate in driving fire activity across the United States’, *Proceedings of the National Academy of Sciences*, 114(52), pp. 13750–13755. doi: 10.1073/pnas.1713885114.
- Tansey, K. *et al.* (2008) ‘A new, global, multi-annual (2000–2007) burnt area product at 1 km resolution’, *Geophysical Research Letters*, 35(1), p. L01401. doi: 10.1029/2007GL031567.

- Turetsky, M. R. *et al.* (2011) 'Recent acceleration of biomass burning and carbon losses in Alaskan forests and peatlands', *Nature Geoscience*, 4(1), pp. 27–31. doi: 10.1038/ngeo1027.
- Turner, M. G. *et al.* (1998) 'Factors Influencing Succession: Lessons from Large, Infrequent Natural Disturbances', *Ecosystems*, 1(6), pp. 511–523. doi: 10.1007/s100219900047.
- Townshend, J. R. (1992) 'Improved global data for land applications: A proposal for a new high resolution data set.' IGBP Global Change Report Number 20, International Geosphere-Biosphere Programme, Stockholm, Sweden.
- val Martin, M., Logan, J. A. and Kahn, R. A. (2010) 'Smoke injection heights from fires in North America: analysis of 5 years of satellite observations', *Atmos. Chem. Phys.*, p. 21.
- van der Werf, G. R. *et al.* (2006) 'Interannual variability in global biomass burning emissions from 1997 to 2004', *Atmospheric Chemistry and Physics*, 6(11), pp. 3423–3441. doi: 10.5194/acp-6-3423-2006.
- van der Werf, G. R. *et al.* (2010) 'Global fire emissions and the contribution of deforestation, savanna, forest, agricultural, and peat fires (1997–2009)', *Atmospheric Chemistry and Physics*, 10(23), pp. 11707–11735. doi: 10.5194/acp-10-11707-2010.
- van der Werf, G. *et al.* (2009) 'Estimates of fire emissions from an active deforestation region in the southern Amazon based on satellite data and biogeochemical modelling'. Available at: <https://escholarship.org/uc/item/3rq0j7pf>.
- van der Werf, G. R. *et al.* (2017) 'Global fire emissions estimates during 1997–2016', *Earth System Science Data*, 9(2), pp. 697–720. doi: <https://doi.org/10.5194/essd-9-697-2017>.
- van Langevelde, F. *et al.* (2003) 'Effects of Fire and Herbivory on the Stability of Savanna Ecosystems', *Ecology*, 84(2), pp. 337–350. doi: 10.1890/0012-9658(2003)084[0337:EOFAHO]2.0.CO;2.
- van Leeuwen, T. T. and van der Werf, G. R. (2011) 'Spatial and temporal variability in the ratio of trace gases emitted from biomass burning', *Atmospheric Chemistry and Physics*, 11(8), pp. 3611–3629. doi: <https://doi.org/10.5194/acp-11-3611-2011>.
- Veltkamp, R. C. (2001) 'Shape matching: Similarity measures and algorithms', in *Proceedings - International Conference on Shape Modeling and Applications, SMI 2001*. IEEE Computer Society, pp. 188–197. doi: 10.1109/SMA.2001.923389.
- Westerling, A. L. *et al.* (2006) 'Warming and Earlier Spring Increase Western U.S. Forest Wildfire Activity', *Science*, 313(5789), pp. 940–943. doi: 10.1126/science.1128834.

- Whelan, R. (1995) *The ecology of fire*. Available at:  
[https://books.google.com/books?hl=en&lr=&id=4bFxAwAAQBAJ&oi=fnd&pg=PR9&dq=+Whelan,+R.+J.+\(1995\).+The+ecology+of+fire.+Cambridge+university+press.&ots=\\_6IMwArWPs&sig=vruTwAIQFTeXIPfQOR\\_fVwsp4g](https://books.google.com/books?hl=en&lr=&id=4bFxAwAAQBAJ&oi=fnd&pg=PR9&dq=+Whelan,+R.+J.+(1995).+The+ecology+of+fire.+Cambridge+university+press.&ots=_6IMwArWPs&sig=vruTwAIQFTeXIPfQOR_fVwsp4g).
- Wolfe, R. E., Roy, D. P. and Vermote, E. (1998) 'Modis Land Data Storage, Gridding, And Compositing Methodology: Level 2 Grid - Geoscience and Remote Sensing, IEEE Transactions on', *ieeexplore.ieee.org*, 36(4), pp. 1324–1338.
- Yan, L. and Roy, D. P. (2014) 'Automated crop field extraction from multi-temporal Web Enabled Landsat Data', *Remote Sensing of Environment*. Elsevier, 144, pp. 42–64. doi: 10.1016/J.RSE.2014.01.006.
- Yue, C. *et al.* (2014) 'Modelling the role of fires in the terrestrial carbon balance by incorporating SPITFIRE into the global vegetation model ORCHIDEE-Part 1: Simulating historical global'. Available at:  
<https://ore.exeter.ac.uk/repository/handle/10871/19599>.
- Yue, C. *et al.* (2015) 'Modelling the role of fires in the terrestrial carbon balance by incorporating SPITFIRE into the global vegetation model ORCHIDEE – Part 2: Carbon emissions and the role of fires in the global carbon balance'. Available at:  
<https://hal-insu.archives-ouvertes.fr/insu-01204878> (Accessed: 23 June 2019).
- Zhang, Y. H. *et al.* (2003) 'Monthly burned area and forest fire carbon emission estimates for the Russian Federation from SPOT VGT', *Remote Sensing of Environment*, 87(1), pp. 1–15. doi: 10.1016/S0034-4257(03)00141-X.